DISSERTATION

Development of Parallel Radiofrequency Transmission Approaches for Magnetic Resonance Imaging of Conductive Biodegradable Implants

Entwicklung paralleler Hochfrequenztechnologie für die Magnetresonanztomographie elektrisch leitfähiger, biologisch abbaubarer Implantate

zur Erlangung des akademischen Grades
Doctor of Philosophy (PhD)

vorgelegt der Medizinischen Fakultät
Charité – Universitätsmedizin Berlin

von

Mostafa Berangi (MSc)

Erstbetreuung: Prof. Dr. rer.nat. Thoralf Niendorf

Datum der Promotion: February 28, 2025

Table of contents

List of tables

List of figures

List of abbreviations

ASTM	American Society of Testing and Materials
B_0	Main Magnetic Field
B1+	Rotating component of RF magnetic field
CP	Circular Polarization
CT	Computed Tomography
D	Diameter
DICOM	Digital Imaging and Communications in Medicine
EMF	Electro Magnetic Field
FOV	Field of View
GAP	Genetic Algorithm
GRE	Gradient Echo
L	Length
Mg	Magnesium
MRI	Magnetic Resonance Imaging
OP	Orthogonal Projection
PTX	Parallel Transmission
R	Radius
RF	Radio Frequency
ROI	Region of Interest
SAR	Specific Absorption Rate
SNR	Signal-to-Noise Ratio
T	Tesla
TE	Echo Time
Ti	Titanium
TR	Repetition Time
TSE	Turbo Spin Echo

Abstract

Orthopedic implants are of high clinical relevance for the repair of musculoskeletal injuries. Conventional implants commonly require removal upon success of the bone healing process. Biodegradable implants present an alternative to conventional implants by making implant removal surgery obsolete. This merit arises from the degrading nature inherent to the new implant materials such as Magnesium based alloys.

Post implantation, non-invasive tracking of the implantation site and of the healing process is part of the clinical workflow aided by imaging. Magnetic resonance imaging (MRI) is a viable alternative for monitoring of implantation sites. MRI is free of ionizing radiation, ensuring a safer diagnostic imaging approach.

A large body of literature reports that conventional metal-based implants potentially constrain the diagnostic quality of MRI and elevate the level of deposited radiofrequency (RF) energy in implantation sites. Yet, the impact of biodegradable implants with a degrading structure on the quality of MRI is underexplored.

Recognizing this opportunity, this thesis focuses on three main goals. First, the impact of biodegradable implants on MRI distortion artefacts at the implantation site is carefully examined. The main finding from this study is that Mg-based implants generate lower metallic distortion in MRI when compared to conventional Ti-based implants. Second, radiofrequency induced heating of biodegradable orthopedic screw implants due to the interference between the passive electrically conductive implants and the RF power deposited in the body during an MRI examine is investigated. The main conclusion from this study is that the highest risk of RF induced implant heating is most pronounced for Mg-based screws prior to degradation. Following the careful assessment of the MRI characteristics of biodegradable implants a radiofrequency transmission field shimming method is developed and applied with the goal to compensate or even eliminate image distortion or RF heating in the presence of biodegradable implants. The approach developed in this thesis project makes use of RF antenna arrays customized for parallel RF transmission to generate dedicated electromagnetic field (EMF) patterns which are derived from RF excitation vector optimization tailored for MRI of implantation sites. The proposed method is validated in numerical simulations and benchmarked against conventional approaches in phantom experiments using a 7.0 T whole body MRI scanner. For this purpose, MRI-aided transmission field mapping, MR thermometry, and MR imaging of implantation sites were performed. In conclusion, parallel RF transmission using optimized RF excitation vectors in conjunction with dedicated RF antenna arrays provides a technical foundation *en route* to safe and MRI of implantation sites with diagnostic image quality free of transmission field distortions, which is the main achievement of this thesis project.

Zusammenfassung

Orthopädische Implantate sind von hoher klinischer Relevanz. Herkömmliche Implantate müssen in der Regel nach erfolgreichem Heilungsverlauf operativ entfernt werden. Für biologisch abbaubare Implantate entfällt diese Notwendigkeit. Dieser Vorteil ergibt sich aus den Materialeigenschaften und dem natürlichen Abbau neuer biologisch resorbierbarer Implantate wie etwa Magnesiumlegierungen.

Post-operativ ist die nicht-invasive Überwachung der Implantationsstelle und des Heilungsprozesses Teil der klinischen Kontrolle. Diese wird mittels, bildgebender Verfahren, einschließlich der Magnetresonanztomographie (MRT), unterstützt.

Die Fachliteratur zeigt auf, dass herkömmliche metallische Implantate die diagnostische Qualität der MRT potenziell beeinträchtigen können. Ebenso ist die Erhöhung des Eintrages von in der MRT verwendeter Radiofrequenzenergie an Implantationsstellen und damit einhergehende mögliche Erwärmung umliegenden Gewebes als potentielles Risiko dokumentiert. Das äquivalente Verhalten biologisch abbaubarer Implantate mit dynamischer Geometrie und Struktur auf die Qualität und Sicherheit der MRT ist nicht hinlänglich erforscht.

Deshalb konzentriert sich diese Dissertation auf drei Hauptziele. Zunächst wird der Einfluss biologisch abbaubarer Implantate auf MRT-Artefakte wie störende Bildverzerrungen an der Implantationsstelle untersucht. Das Kernergebnis dieses Teils ist, daß Mg-basierte Implantate im Vergleich zu herkömmlichen Ti-basierten Implantaten weitaus geringere Bildverzerrungen in der MRT erzeugen. Im nächsten Schritt wird durch Radiofrequenzenergie induzierte Erwärmung elektrisch leitender, biologisch abbaubarer Schraubenimplantate untersucht. Die wichtigste Schlussfolgerung dieses Teils der Dissertation besteht darin, dass für Mg-basierte orthopädische Schrauben das höchste Risiko für Hochfrequenzenergie induzierte Implantat Erwärmung vor Resorption am stärksten ausgeprägt ist.

Nach der Bewertung dieser Ergebnisse wurde eine Methode zur gezielten Anregung des MRT-Radiofrequenzfeldes entwickelt. Dieser methodische Ansatz der parallelen Anregung ist maßgeschneidert, um Bildverzerrungen oder HF-Erwärmung in Gegenwart biologisch abbaubar Implantate zu kompensieren und bestenfalls zu eliminieren, um somit die MRT-unterstützte Überwachung von Implantationsstellen zu verbessern. Der Ansatz verwendet eigens entwickelte Hochfrequenzantennen für maßgeschneiderte parallele MRT-Signalanregung, Diese wird aus der in der Arbeit entwickelten Vektoroptimierung der Hochfrequenzfelder hergeleitet. Die vorgeschlagene Methodik wird in numerischen Simulationen validiert und in Phantomexperimenten mit einem 7.0 T-Ganzkörper-MRT-Scanner mit konventionellen Ansätzen verglichen.

Zusammenfassend bietet die parallele Verwendung optimierter RF-Anregungsvektoren eine technische Grundlage für sichere MRT von Implantationsstellen mit diagnostischer Bildqualität. Dieses Ergebnis ist der Haupterfolg dieses Dissertationsprojekts.

1 Introduction

This chapter contains and uses results of my research that have been published in:

- **Paper 1**
  Jonathan Espiritu, Mostafa Berangi, Christina Yiannakou, Eduarda Silva, Roberto Fran-cischello, Andre Kühne, Thoralf Niendorf, Sören Könneker, Regine Willumeit-Römer, Jan-Marten Seitz, Evaluating metallic artefact of biodegradable magnesium-based im-plants in magnetic resonance imaging Bioactive Materials 15, 2022
- **Paper 2**
  Jonathan Espiritu, Mostafa Berangi, Hanna Cwieka, Kamila Iskhakova, Andre Kuehne, D.C. Florian Wieland, Berit Zeller-Plumhoff, Thoralf Niendorf, Regine Willumeit-Römer, Jan-Marten Seitz, Radiofrequency induced heating of biodegradable orthopedic screw implants during magnetic resonance imaging, Bioactive Materials 25, 2023
- **Paper 3**
  Mostafa Berangi, Andre Kuehne, Helmar Waiczies and Thoralf Niendorf, MRI of Implantation Sites Using Parallel Transmission of an Optimized Radiofrequency Excitation Vector, Tomography 9(2), 2023

and therefore, contains text, statements, passages and figures from these publications.

1.1 Background

Orthopedic implants play a pivotal role in addressing musculoskeletal injuries and disorders. Conventional implants, including titanium and stainless steel, have been extensively utilized in orthopedic surgeries due to their favorable mechanical properties and biocompatibility. Nonetheless, these materials can potentially elicit noteworthy complications, such as inciting inflammatory reactions [1] and elevating the risk of refractures [2]. Consequently, there has been an expanding exploration of alternative implant materials. Among these, magnesium (Mg)-based alloys have garnered attention in the fields of material sciences and medicine [3-5], as they can safely degrade in vivo while serving as load-bearing implant materials, rendering them appealing for temporary bone support [6-8].

An imperative aspect in utilizing metallic implants, such as biodegradable Mg-based implants, pertains to their compatibility with medical imaging. Magnetic resonance imaging (MRI) presents a viable diagnostic modality for assessing the degradation state of biodegradable implants and studying the implant-tissue interface [9-12]. MRI is a mainstay of contemporary diagnostic imaging due to its capability to deliver exceptional soft tissue contrast with high spatial resolution, rendering it ideal for monitoring the post-orthopedic implantation healing process [13-15]. However, the presence of metallic implants during MRI can give rise to various challenges, as metals influence the static main magnetic field (B_0) and the dynamic electromagnetic fields (EMF, magnetic component: H-field, electric component: E-fields) of the MRI system (B_1^+ and gradient fields). These interactions not only introduce potential image artifacts such as image distortions and signal voids due to susceptibility gradients and H-field inhomogeneities but also potentially pose safety hazards due to tissue heating caused by the interference between E-fields and passive conducting implants.

While the introduction of magnetic metals (termed ferromagnetic materials) in proximity to an MRI system is strictly prohibited due to their strong attraction to the static B_0 field, presenting substantial safety risks [16], nonmagnetic metals (e.g., Mg and Ti) are not attracted by the static magnetic field and can be positioned in an MRI environment. Nevertheless, these metals possess distinct magnetic susceptibilities from that of bone and muscle, inducing significant local disruptions in the B_0 field. This, in turn, leads to geometric distortions in MRI images (susceptibility artifacts), potential signal loss due to shortened effective transverse relaxation time T2*, or even signal voids in regions with high B_0 gradients. Furthermore, these metals can trigger off-resonance effects resulting from ΔB_0-induced frequency variations [17]. These challenges can be addressed through on- and off-resonance methodologies, enabling MRI of implants devoid of B_0 distortions and signal voids [18-22].

Furthermore, these metals can interact with dynamic EMFs, introducing additional problems in terms of image artifacts (corresponding to implant induced magnetic fields) and potential safety concerns due to escalated specific absorption rates (SAR) of radiofrequency energy at the implant site (corresponding to implant induced electric fields), leading to tissue heating during MRI. One type of tissue heating occurs in case of heat conduction from a heated implant to adjacent tissues. This form of heating mainly arises from the interaction between metallic implants and gradient EMFs, and it is particularly pronounced in larger metallic implants such as hip joint implants [23]. Another type of implant heating is through induction heating, which is more pronounced in MRI and arises from the interaction between conductive implants and transmitted RF fields. This type of heating can stem from large or small metallic implants, resulting in scattered RF EMFs. The superposition of incident E-fields (E_{inc}) from the RF transmitter and the implant-induced scattered E-fields (E_{sca}) might result in locally elevated total E-fields ($E_{total} = E_{inc} + E_{sca}$) of implantation site. This can cause an increase in the SAR by $(E_{total})^{\wedge 2}$, potentially leading to increased RF-induced heating. The extent of heating depends on the operating frequency of the MR scanner and the physical length of the metallic implant. For instance, when using a 7.0 Tesla MRI scanner, the RF wavelength (λ) in brain tissue is relatively short (λ ~12 cm) compared to the size range of clinically available orthopedic implants. Consequently, resonance and therefore significant heating effects can occur within a range approximately from λ/4 to λ/2. [24].

Additionally, the superposition of magnetic components of scattered and incident fields can induce non-uniformities in the RF transmission field B_1^+. These interferences might manifest as non-uniform image intensities, signal shading, signal voids, or signal intensity elevations near the implant. These advert effects have the potential to compromise the primary advantage of MRI, which is diagnostic image quality [17].

It's essential to note that the degree of RF-induced heating and RF transmission field distortions can vary based on the shape, location, and orientation of a conductive implant, along with the RF excitation vector in parallel RF transmission (pTx) [25]. Overall, these constraints highlight the importance of carefully considering the type of implant and the potential risks associated with MRI monitoring when planning the use of this imaging modality for patients with implanted devices.

Numerous studies have been published concerning MRI hardware and methodologies designed to investigate and mitigate RF-induced implant heating and/or RF shading near conductive implants [26-28]. Researchers have successfully demonstrated the reduction of RF heating at the tip of metallic implant leads and the enhancement of B_1^+ homogeneity by altering the magnitude of the excitation currents on two separate channels of a dual-drive birdcage RF coil [29]. Furthermore, researchers have employed a pTx pulse design at 3.0 T to minimize SAR near a deep brain stimulation device (DBS) in a uniform flip-angle excitation scheme, which has been confirmed in numerical EMF simulations [30]. Numerical simulations have been employed to explore the application of RF coil configurations utilizing parallel transmission at 3.0 T MRI on phantom studies and cadaver studies, to reduce absorbed power or improve transmission field uniformity around DBS implants [31, 32]. An optimization process based on a subject-dependent optimization factor has been recommended to limit SAR while maintaining uniform B_1^+ [33]. A more comprehensive mathematical approach for MRI compatible with implants has been proposed, previously demonstrated in a theoretical cylindrical model [34]. However, direct implementation of this approach in a practical RF transmitter array is challenging, as the desired B_1^+ profile and zero E-field in the implant were stringent constraints in the optimization formulation, and the available degrees of freedom in a realistic pTx array are constrained by the number of transmit channels. These constraints may lead to an unsolvable optimization problem, as not all restrictions can be simultaneously met with the limited number of transmit channels. Other innovative strategies involve manipulating RF transmission fields with RF arrays and parallel transmission using maximum- and null-current modes [35]. Machine-learning-based prediction of RF power absorption or rapid computation of RF field enhancements near medical implants provide computational approaches for implant-specific RF heating assessment and management [36, 37].

Given the growing population of patients with orthopedic implants [38], comprehending and addressing the interaction of passive conductive implants with RF fields is vital to advance MRI at implantation sites while ensuring patient safety and distortion-free B_1^+ fields. This clinical need applies to traditional implants made of titanium or stainless steel as well as clinically available biodegradable implants based on magnesium [39, 40]. The latter not only enhances patient comfort but also reduces healthcare expenses by obviating implant removal surgeries. Utilization of small biodegradable screw implants (short implants) are real world examples in the clinic.

1.2 Research questions

The potential of Mg-based alloys as an alternative implant material is underscored by their capacity to degrade safely in vivo while exhibiting mechanical properties akin to natural bone. The utilization of MRI for guided monitoring of the implant site serves a dual purpose: it facilitates the tracking of tissue healing and offers insights into the implant's performance and degradation status. However, the judicious selection and application of Mg-based implants necessitate a thorough consideration of potential image artifacts and heating that can occur during MRI procedures. The meticulous assessment of artifact generation in MRI is imperative to ensure optimal medical diagnosis and precise anatomical depiction. Furthermore, a comprehensive evaluation of the safety of Mg implants under the influence of dynamic electromagnetic fields (EMFs) is essential. Concomitantly, it is crucial to explore strategies to ameliorate the undesired effects of implants on MRI image quality and safety. Hence, the main three research questions addressed in this dissertation are:

a) To systematically assess the occurrence of image artifacts stemming from Mg implants during MRI.
b) To decipher and quantify the degree of tissue heating at the implantation site induced by the presence of Mg implants.
c) To propose and demonstrate feasibility of RF parallel transmission technology tailored for mitigation of unfavorable B_1^+ artifact and tissue heating that might arise during MRI imaging of the implantation site containing Mg-based implants.

The outcome of this research has been published in three papers:

- **Paper** 1:
  *Jonathan Espiritu, **Mostafa Berangi**, Christina Yiannakou, Eduarda Silva, Roberto Francischello, Andre Kühne, Thoralf Niendorf, Sören Könneker, Regine Willumeit-Römer, Jan-Marten Seitz, Evaluating metallic artefact of biodegradable magnesium-based implants in magnetic resonance imaging Bioactive Materials 15, 2022*
- **Paper** 2:
  *Jonathan Espiritu, **Mostafa Berangi**, Hanna Cwieka, Kamila Iskhakova, Andre Kuehne, D.C. Florian Wieland, Berit Zeller-Plumhoff, Thoralf Niendorf, Regine Willumeit-Römer, Jan-Marten Seitz, Radiofrequency induced heating of biodegradable orthopedic screw implants during magnetic resonance imaging, Bioactive Materials 25, 2023*
- **Paper** 3:
  ***Mostafa Berangi**, Andre Kuehne, HelmarWaiczies and Thoralf Niendorf, MRI of Implantation Sites Using Parallel Transmission of an Optimized Radiofrequency Excitation Vector, Tomography 9(2), 2023*

I wish to disclose explicitly that this dissertation uses methods, results and critical discussion that have been published in these three papers and therefore contains text, statements, passages and figures from these three publications.

2 Methods

The methods and materials used in this study are outlined in two sections:

1. Assessment of radio frequency interactions of Mg-based implants with an MRI scanner.
2. Development, evaluation, validation and application of parallel RF transmission technology tailored for the reduction of unwanted artefacts and tissue heating in the presence Mg-based implants.

This chapter contains and uses results of my research that have been published in:

- **Paper 1**
  Jonathan Espiritu, Mostafa Berangi, Christina Yiannakou, Eduarda Silva, Roberto Fran-cischello, Andre Kühne, Thoralf Niendorf, Sören Könneker, Regine Willumeit-Römer, Jan-Marten Seitz, Evaluating metallic artefact of biodegradable magnesium-based im-plants in magnetic resonance imaging Bioactive Materials 15, 2022
- **Paper 2**
  Jonathan Espiritu, Mostafa Berangi, Hanna Cwieka, Kamila Iskhakova, Andre Kuehne, D.C. Florian Wieland, Berit Zeller-Plumhoff, Thoralf Niendorf, Regine Willumeit-Römer, Jan-Marten Seitz, Radiofrequency induced heating of biodegradable orthopedic screw implants during magnetic resonance imaging, Bioactive Materials 25, 2023
- **Paper 3**
  Mostafa Berangi, Andre Kuehne, Helmar Waiczies and Thoralf Niendorf, MRI of Implantation Sites Using Parallel Transmission of an Optimized Radiofrequency Excitation Vector, Tomography 9(2), 2023

and therefore, contains text, statements, passages and figures from these publications.

2.1 Radio frequency interactions of Mg-based implants with MRI scanner

This section represents the methods implemented for in vivo measurement of the interactions between the MRI scanner and Mg-based and other metallic implants. These interactions are categorized into a) image artefact and b) MRI induced heating of tissue in the vicinity of an implant. The following subsections will discuss the sample preparation, measurement setup, and the protocol employed for the measurements.

2.1.1 Samples preparation

Compression screws with a length of 40 mm and a diameter of 3.2 mm, made of Mg-based material developed by Syntellix AG in Hannover, Germany, were subjected to degradation in a laboratory setting. The volume of the Mg-based screw was measured to be 151.51 mm3, with a surface area of 552.54 mm^2. The chemical composition of Mg-based biodegradable material includes Yttrium (3.7–4.3%), Rare Earth Elements (2.4–4.4%), and Zirconium (0.4%), with the remainder being composed of Magnesium. In order to compare results, a non-degraded Mg-based screw and a titanium screw with similar dimensions were included as well (Fig. 1).

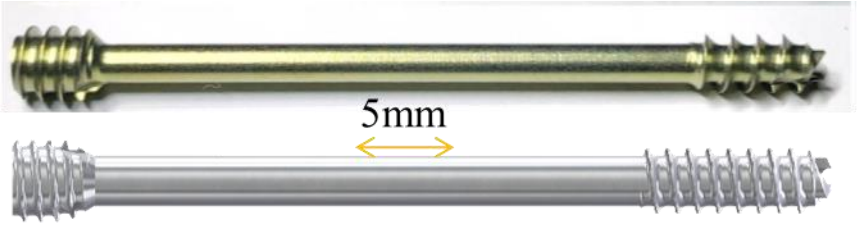

Figure 1: Sample implants used in the experiments of this thesis project. top) A 40 mm titanium screw that serves as the market equivalent screw implant. Bottom) Orthopedic compression screw made of magnesium-based material known as MAGNEZIX® CS ø3.2. (Modified from: Jonathan Espiritu, Mostafa Berangi, Christina Yiannakou, Eduarda Silva, Roberto Francischello, Andre Kuehne, Thoralf Niendorf, Sören Könneker, Regine Willumeit-Römer, Jan-Marten Seitz, ”Evaluating metallic artefact of biodegradable magnesium-based implants in magnetic resonance imaging”, Bioactive Materials 15,2022, [41])

The degradation of the Mg-based samples was carried out using a modified version of the ASTM F3268 Standard [42] with Dulbecco's Phosphate Buffered Saline (DPBS). A total of five screws were immersed in DPBS for different durations, ranging from one to five weeks, with a one-week interval between each time point (1 week, 2 weeks, 3 weeks, 4 weeks, and 5 weeks). After each immersion period, the samples were cleansed with distilled water to remove excess salts, rinsed with ethanol to prevent further oxidation, and then dried and stored.

2.1.2 Experimental setup for the assessment of MRI artefacts induced by Mg-based implants

The test object was suspended in a custom-made phantom acrylic container using a 3D printed holder and submerged in a $CuSO_4$ solution (Merck Millipore, USA) to reduce T_1 relaxation effects. The dimensions of artifacts were determined using a custom MATLAB script following the ASTM F2119 [43] definition.

To measure the diameter artifact, the longest artifact along the screw's diameter was determined. The length artifact was measured as the longest artifact along the screw's length. The largest measurements were considered as the "worst-case" artifacts.

Calculation of test object distortion was conducted to assess the artifact size in relation to the dimensions of the test object. Test object distortion is calculated by:

$$\frac{Total\ artefact\ length\ measured - test\ object\ dimension}{Test\ object\ dimension}$$

2.1.3 Experimental setup for the assessment of RF induced heating of Mg-based implants

A rectangular case made of acrylic glass was constructed according to the dimensions defined by the ASTM Standard. The case was filled with a tissue-mimicking phantom gel. The phantom gel consisted of 25 L of distilled water, 1.32 g/L NaCl (Sigma Aldrich, Taufkirchen, Germany) and 10 g/L of polyacrylic acid (Sigma Aldrich, Taufkirchen, Germany). Prior to each heating test, a calibration following the procedures described in ASTM F2182 [44] was conducted to compensate for the local incident field.

A specifically crafted non conducting holder was manufactured using 3D-printed to safely fasten the samples and direct fiber-optic probes from the thermometry system. (model T1; Neoptix Inc., Québec, Canada) to the tips of the implants, which represent the highest heating points [45]. In total three probes were considered in the setup, two were placed at the tips of the implant and the third was placed on the opposite side of the phantom as the reference probe measuring the RF-induced temperature elevation not affected by the implant. It was ensured that the probe was positioned at the same distance from the implant for different samples. The holder, containing a single screw sample, was positioned at the center, 2 cm away from the phantom wall, and aligned with the main magnetic field, as this orientation was previously identified as having maximum heating [46]. The acrylic case was then placed in a Styrofoam insulation container for scanning, as shown in Figure 2.

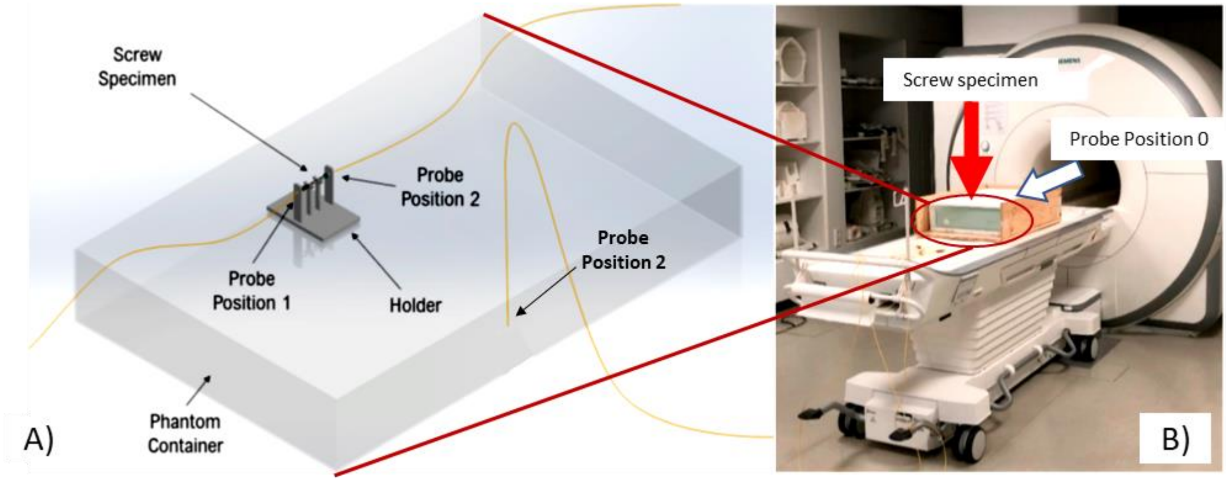

Figure 2: Experimental setup used for the assessment of RF heating induced by Magnesium-based implants during MRI. A) Basic scheme of the experimental setup based on the ASTM F2182 guidelines [44]. B) real world temperature measurements where the phantom setup was positioned at the isocenter of the MR scanner (Modified from Jonathan Espiritu, Mostafa Berangi, Hanna Cwieka, Kamila Iskhakova, Andre Kuehne, D.C. Florian Wieland, Berit Zeller-Plumhoff, Thoralf Niendorf, Regine Willumeit-Römer, Jan-Marten Seitz, ”Radiofrequency induced heating of biodegradable orthopaedic screw implants during magnetic resonance imaging”, Bioactive Materials 25, 2023, [47]).

To guarantee the gel phantom attains the equilibrium temperature, it was relocated to the MRI room 24 hours prior to the heating experiments. The temperature was noted two minutes before and after initiating the scanning sequence (four minutes in total), with one-second intervals. For every sample, a measurement was acquired in the absence of the sample implant to set a baseline, and a subsequent measurement was taken with the implant positioned in the phantom to evaluate the temperature rise attributable to the implant itself.

2.1.4 MRI experiments

For the in vitro (phantom-based) MRI measurements of image artefact, three MRI scanners were employed: a 1.5 T (GE Signa Artist, GE Healthcare, Waukesha, USA), a 3.0 T (Skyra Fit, Siemens, Erlangen, Germany), and a 7.0 T (Magnetom, Siemens, Erlangen, Germany). The phantom imaging was adapted from ASTM F2119 (43) where the the long axis of the implant was positioned (1) perpendicular and (2) parallel to the main magnetic field (B_0). Different combinations of implant orientation relative to the main magnetic field, imaging sequences, slice orientations, phase-encoding directions, and materials were employed before each image acquisition. Table 1 provides additional details regarding the imaging protocol and techniques utilized for the in vitro measurements.

In vitro temperature measurements were conducted only on a 3.0 T MRI scanner (Skyra Fit, Siemens, Erlangen, Germany). The procedure for assessing the degraded samples and titanium equivalent was adapted from ASTM F2182 [44]. The objective of the MR scanning for the heating measurement was to introduce energy using the RF transmitter (body coil) into the setup, which is the primary cause of implant-induced heating. To achieve this goal, a turbo spin echo sequence was utilized for a duration of 939 seconds, with the maximum allowable SAR (Specific Absorption Rate).

Table 1: Protocol parameters for the pulse sequences employed in the in vitro MRI examinations of implant induced image artefacts. (Modified from Modified from Jonathan Espiritu, Mostafa Berangi, Christina Yiannakou, Eduarda Silva, Roberto Francischello, Andre Kuehne, Thoralf Niendorf, Sören Könneker, Regine Willumeit-Römer, Jan-Marten Seitz, ”Evaluating metallic artefact of biodegradable magnesium-based implants in magnetic resonance imaging”, Bioactive Materials 15,2022, [41])

	Field Strength (B0) [T]					
	7.0		3.0		1.5	
RF Coil	Spine		Spine		Volume	
Sequence	GRE	TSE	GRE	TSE	GRE	TSE
TR [ms]	550	1190	500	1190	100	500
TE [ms]	13	30	13	20	15	20
FOV [mm]	185	185	180	200	300	300
Matrix Size [pixel]	256	256	256	256	256	256
Slice Thickness [mm]	2	2	2	2	2	2

2.2 Reduction of implant induced image artefacts and RF induced tissue heating

This section provides an overview of the procedures developed to establish novel methodology for elimination of unwanted effects of the Mg-based implant (in general every small metallic implant) in MRI which are categorized into four sections:

1. RF transceiver array configurations: design criteria and electromagnetic field (EMF) simulations that are considered and conducted to determine the most suitable RF array configuration using commonly utilized RF transceiver components.

2. Transmission field shaping (B_1^+ shimming): optimization of the excitation vector to minimize the occurrence of scattered fields.

3. The phantom experiments section elaborates on measures taken and setups used for the validation of the EMF simulations through experimental studies conducted at 7.0 T.

4. The sections dedicated to MR thermometry and transmission field mapping describe the metrics employed for the purpose of validation.

2.2.1 RF transceiver array configurations

Numerical electromagnetic field (EMF) simulations were conducted at 297.2 MHz (corresponding to a 7.0 T MRI) to examine the interaction between electrically conductive implants, electric fields (E-fields), and magnetic fields (B-fields). Eight configurations of radiofrequency (RF) arrays, specifically designed for MRI of body extremity, were evaluated to determine the configuration that provided the best performance in terms of B_1^+ field uniformity and strength along with the lowest specific absorption rate (SAR) value.

The eight proposed and investigated configurations are shown in Figure 3:

(A–D) Eight loop elements of equal length (L = 100 mm) but varying widths (W), where $W_n = ((210\text{ mm})\ \pi/16) \times \alpha_n$, with n ranging from 1 to 4 and α_n values of 1, 1.25, 1.5, and 1.75.

(E) Eight fractionated dipoles (L = 200 mm, W = 5 mm).

(F) Birdcage RF resonator with degenerate characteristics (L = 100 mm, D = 210 mm) utilizing eight rungs.

(G) A four-rung degenerate birdcage (L = 100 mm, D = 210 mm) and four fractionated dipoles (L = 200 mm, W = 5 mm), with each fractionated dipole positioned between the rungs of the birdcage.

(H) Eight modules consisting of a loop (L = 100 mm, W = (210 mm) π/16) and a fractionated dipole [48, 49] (L = 200 mm, W = 5 mm) placed at the center of the loop.

RF transceivers were uniformly distributed around a cylindrical phantom (length, L = 300 mm; diameter, D = 170 mm). The phantom was designed to replicate the electrical characteristics of muscle at the operation frequency of a 7T MRI scanner (f=297.2 MHz, εr = 58.24 and σ = 0.769 S/m,). The RF transceiver arrays were located 20 mm from the phantom and shielded at a distance of 30 mm.

The RF array configurations were implemented using CST Studio Suite 2020 (CST MWS, Darmstadt, Germany) and the Finite Integration Technique (FIT) [50]. The EMF simulations employed a mesh resolution finer than 1.5 mm^3. Matching and tuning capacitors of the system were adjusted to ensure that the magnitude of reflection coefficient of scattering parameters remained below -15 dB. Transformers were used for decoupling of the neighbouring loop elements [51] to below -15dB, while no decoupling was necessary for the dipole elements due to their geometric separation.

To evaluate the performance of the RF arrays, a cylindrical region of interest (ROI) with dimensions of L = 110 mm and R = 20 mm, covering the implant, was used to assess the strength and uniformity of the B_1^+ field. Additionally, the maximum induced SAR (averaged over 10 g of tissue, SAR10g,max) throughout the entire phantom was measured. A cylindrical object mimicking a conductive screw implant (L = 70 mm, R = 1 mm, σ = 5.8 × 10^8 S/m), was considered within the phantom. The implant was oriented parallel to the phantom's axis and placed 30 mm away from the phantom surface. This simulation setup allowed for the evaluation of the RF array configurations in terms of B_1^+ field characteristics and the maximum SAR induced within the phantom.

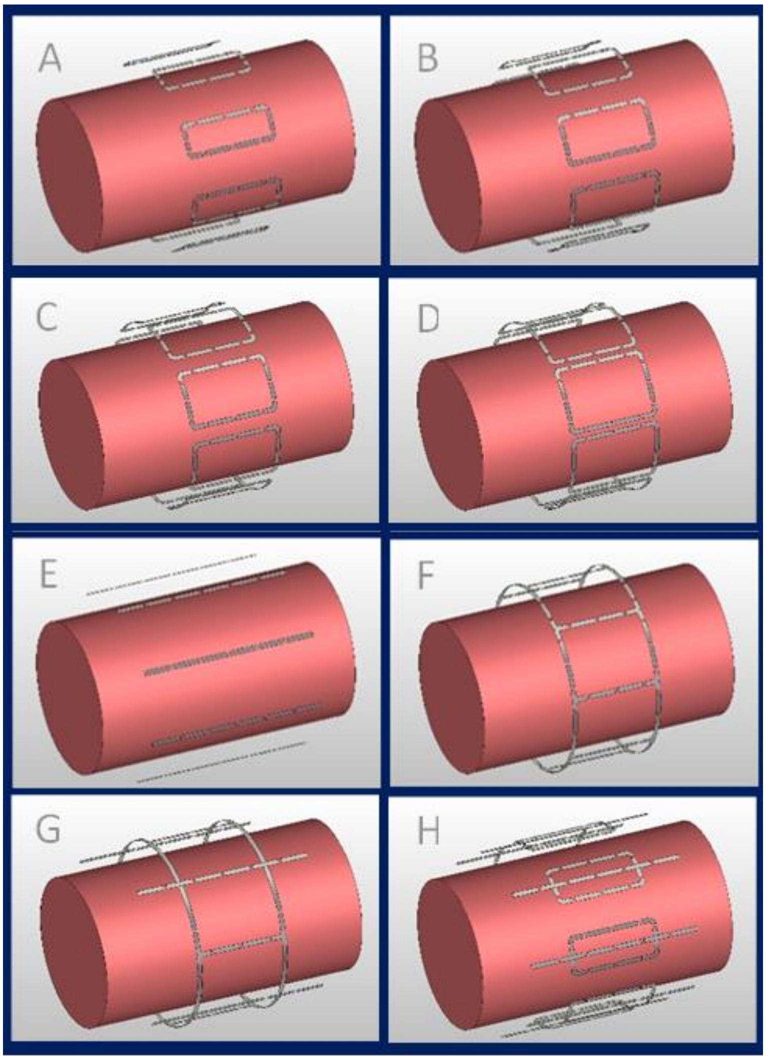

Figure 3: Different configurations of an eight-channel RF transceiver array investigated in the EMF simulations. (A–D) Eight loop elements with a length (L) of 100 mm and varying widths (W) approximately equal to 41 mm, 52 mm, 62 mm, and 72 mm. (E) Eight fractionated dipoles with a length of 200 mm. (F) Degenerate birdcage configuration with eight rungs, where the length (L) is 100 mm and the diameter (D) is 210 mm. (G) Hybrid configuration combining a birdcage with four rungs (L = 100 mm, D = 210 mm) and four dipoles (L = 200 mm). (H) Loop-dipole array consisting of a loop element with a length of 100 mm and a width approximately equal to 41 mm, and a dipole element with a length of 200 mm (Modified from Berangi, Mostafa, Andre Kuehne, Helmar Waiczies, and Thoralf Niendorf. "MRI of Implantation Sites Using Parallel Transmission of an Optimized Radiofrequency Excitation Vector" Tomography 9 (2), 2023, [52]).

2.2.2 Transmission field Shaping (B_1^+ Shimming)

In order to achieve a strong and uniform B_1^+ field in the target ROI containing the implant, while also reducing the local SAR_{max} below the limits set by the IEC guidelines

[16], transmission field shaping was conducted. The MATLAB toolbox [53] was utilized, employing a multi-objective genetic algorithm (GA) approach, to optimize the excitation vectors. The GA-based approach enables the resolution of optimization problems with multiple conflicting objectives.

For the field shaping problem, the GA algorithm outputs a number of excitation vectors based on the predefined objectives. These solutions are located on a trade-off curve (pareto front), illustrating the trade-off between objectives. Enhancing one objective may lead to the deterioration of one or more other objectives.

The following parameters were employed for defining the objectives:

- $\mathrm{local\ SAR_{10g,max}}$: the maximum 10g SAR value of the whole phantom, not just in the ROI containing the implant.
- $\mathrm{B_1\_SAR_{max}} = \mathrm{B_1^+}/\sqrt{\mathrm{local\ SAR_{10g,max}}}$: For the target region of interest (ROI) encompassing the implant, the B1+ values are computed and divided by the maximum 10g local SAR across the entire phantom.
- COV($\mathrm{B_1}$_$\mathrm{SAR_{max}}$)= $\mathrm{std(B_1\_SAR_{max})/mean(B_1\_SAR_{max})}$

The term COV ($\mathrm{B_1\_SAR_{max}}$) governs the uniformity of the B_1^+ where the standard deviation of $\mathrm{B_1^+}/\sqrt{\mathrm{local\ SAR_{10g,max}}}$ inside the ROI is divided by the mean value of the $\mathrm{B_1^+}/\sqrt{\mathrm{local\ SAR_{10g,max}}}$ inside the ROI. The result of this optimization process is a complex excitation vector known as the GA excitation vector (U_{GA}):

$$\vec{U}_{GA} = K_{GA} \times (u_1, u_2, \dots, u_8);\ \text{and}$$

$$|u_n| = 1; 1 \leq n \leq 8, n \in \mathbb{N}$$

The excitation vector in the optimization process is composed of complex excitation values (u_n) corresponding to each RF channel, with the real value constant (K_{GA}) controlling the overall power of the excitation vector.

To ensure the algorithm's sensitivity to small SAR10g,max variations, the optimization tolerance function was set to 10^{-6}. Additionally, for the optimization step, the virtual observation point (VOP) approach [54] was implemented to compress the SAR matrices.

To evaluate the efficiency of the GA-driven excitation vector in achieving a strong and uniform B_1^+ pattern, it was compared to the circular polarization (CP) mode [55]. The CP mode, serving as a reference, corresponds to a simple "Birdcage"-mode excitation. The CP-mode vector U_{CP} is defined as:

$$\vec{U}_{CP} = K_{CP} \times (u_1, u_2, \dots, u_8);$$

$$u_n = \exp(-2\pi i \cdot n/8)\,;\ 1 \leq n \leq 8, n \in \mathbb{N}$$

where $K_{CP}$is a real value constant used for controlling the total excitation vector power, i is the imaginary unit, and u_n correspond to the phase of each RF channel.

The effectiveness of the GA in reducing the implant induced SAR10g was compared to the orthogonal projection (OP) method [28]. In the OP method, the SAR caused by the implant is mitigated by projecting the excitation vector U_{CP} (or any other excitation vector) onto a vector perpendicular to the one that generates the worst-case implant SAR (U_{wc}). By employing this technique, the OP method enables the elimination of implant-induced SAR while still benefiting from the transmission field uniformity advantages provided by the U_{CP} excitation.

$$\vec{U}_{OP} = \widehat{U}_{CP} - \widehat{U}_{wc}\left(\widehat{U}_{CP} \, . \widehat{U}_{wc}\right),$$

$$\widehat{U}_{CP} = \frac{\vec{U}_{CP}}{\|\vec{U}_{CP}\|}, \widehat{U}_{wc} = \frac{\vec{U}_{wc}}{\|\vec{U}_{wc}\|}.$$

The U_{wc} is the eigenvector of the maximum eigenvalue of a single local RF power correlation matrix in the target ROI.

To validate the EMF simulations, experiments were conducted using cylindrical phantoms (300 mm in length and 170 mm in diameter) matching those used in the simulations. Two types of phantoms were employed to replicate the electrical properties of muscle tissue at 297.2 MHz: a liquid-sucrose-based phantom [56] and a solid polyvinylpyrrolidone (PVP)-based phantom [57]. The liquid-sucrose-based phantom was used for conventional MRI and B_1^+ mapping to allow for implant reorientation. Thermal experiments were carried out on the PVP phantom due to the absence of interfering 1H resonance peaks in the NMR spectra of PVP, which enhances the accuracy of MR thermal measurements [57].

In order to replicate the thermal characteristics of biological tissue without inducing extra fluid dynamics from thermal convection, a solution of PVP (33.9% w/w), agarose (0.4% w/w), and NaCl (1.1% w/w) was dissolved in deionized water. No gel agent was used for the sucrose-based phantom, which consisted of sucrose (48.9% w/w) and NaCl (1.9% w/w). A conductivity value of σ = 0.77 S/m was chosen to match the conductivity of muscle tissue across a wide frequency range, based on the electrical properties of various body tissues [58] and the permittivity was set to εr = 58.

To simulate a conducting implant, a copper wire (70 mm in length and 1 mm in outer diameter) was placed inside the phantoms. The maximum length of the implant was determined based on the maximum screw length of currently available biodegradable implants in commercial and clinical use [59]. This method offers a satisfactory approximation of an implant, as the primary origin of scattered fields is the induced current distribution on a metallic implant. These fields are less influenced by the implant's specific shape details [59] and metal characteristics [60]. The container for the phantoms was constructed from acrylic glass (PMMA) material. Cotton strings were employed to suspend the implant within the phantom, reducing undesired interference with electromagnetic fields (EMFs). A setup crafted from Acrylonitrile Butadiene Styrene (ABS) material through 3D printing was utilized to firmly place and secure the implant. (Figure 4).

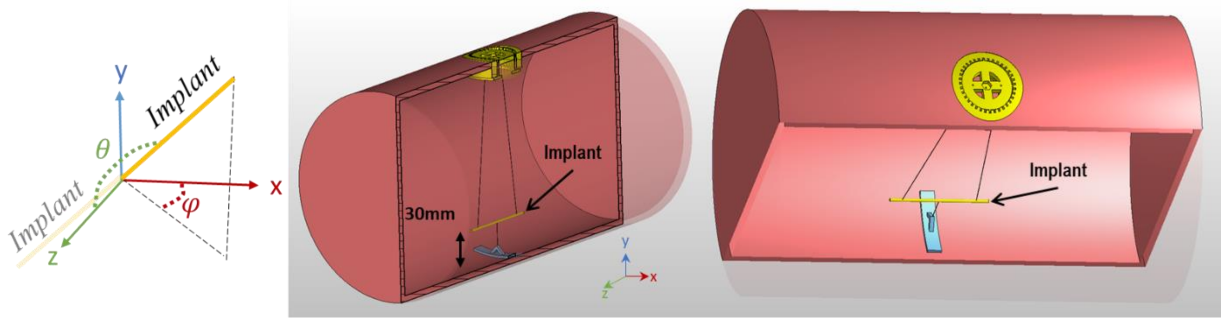

Figure 4: The cross-sectional view of the phantom and the system for positioning the implant. The implant is hung using cotton strings, maintaining a distance of 30 mm from the surface of the phantom. The orientation of the implant can be manipulated by adjusting the length of the strings and rotating the yellow implant adjuster located on the phantom's surface. The orientations are determined using a spherical coordinate system, with polar (θ) and azimuthal (ϕ) angles defined relative to the center of the implant when the origin is aligned with it (Modified from Berangi, Mostafa, Andre Kuehne, Helmar Waiczies, and Thoralf Niendorf. "MRI of Implantation Sites Using Parallel Transmission of an Optimized Radiofrequency Excitation Vector" Tomography 9(2), 2023, [52]).

2.2.3 MR Thermometry

The assessment of RF heating induced by implants using GA- and CP-based excitation vectors was performed through MR thermometry on the PVP phantom. Measurements for MR thermometry were executed at the iso-center of the MRI scanner, where the room temperature was maintained at 297 K. Temperature increment maps were calculated using gradient-echo imaging with a spatial resolution of $1.3 \times 1.3 \times 5.0\ mm^3$, with $TE_1 = 2.26$ ms, $TE_2 = 6.34$ ms, and TR = 246 ms. The proton resonance frequency shift method [50] was utilized before and after RF-induced heating to generate these temperature difference maps. The data from an extra oil sample placed within the field of view was utilized for magnetic field drift compensation [61]. For the RF heating experiment (Pin = 175 W, duration = 5 min), a turbo-spin-echo sequence was employed.

2.2.4 Transmission Field Mapping

The assessment of transmission field shimming methods was performed by B_1^+ mapping based on low flip angle gradient echo imaging. [62, 63]. Cross-sectional and sagittal slices at the implant's center, aligned with the phantom's central axis, were obtained. using the following parameters: TR = 10 s, TE = 2.31 ms, number of averages = 4, matrix size = 256 × 256, and slice thickness = 5 mm. This evaluation focused on the orientation representing the worst-case scenario, where the implant aligns parallel to the E-field lines of the RF arrays (in the designed RF array, along the main magnetic field B_0), guarantees the highest RF coupling between the E-field and the implant. The non-gel sucrose-based phantom, allowing convenient rotation of the implant, was utilized for B_1^+ mapping with various implant orientations.

Discrepancies observed between the simulated and the experimentally measured EMFs could be attributed to resistive losses, phase variations resulting from lumped elements, coupling between RF channel and the surroundings, and other factors. Even small variations can accumulate and impact the RF field pattern, particularly in the vicinity of the implant where EMFs undergo significant alterations. Precise understanding of EMF behavior in this region is crucial for suppressing implant-induced effects. To minimize these discrepancies, a calibration step was performed, involving a simulated B_1^+ map $(\mathrm{B}_{1,s}^{+})$ and its corresponding experimental map $(\mathrm{B}_{1,e}^{+})$, focused on a slice near the implant tip. This target slice was chosen from a region with no interference from the implant, or alternatively, a slice including the implant could be selected while any voxel influenced from the implant is excluded from the selected slice in the implantation regions. The optimization algorithm was tasked to minimize the variations between the measured and simulated B_1^+ maps through calculation of complex calibrating coefficients. The optimization was performed using the following error function:

$$\min_{X} \left\| (X * X_e * \mathrm{B}_{1,s}^{+}) - (X_e * \mathrm{B}_{1,e}^{+}) \right\|$$

Here, $\mathrm{B}_{1,s}^{+}$ and $\mathrm{B}_{1,e}^{+}$represent n×m complex matrices, with the n being the number of channels of the RF transceiver array and m the number of pixels in $\mathrm{B}_{1,e}^{+}$. The calibration coefficients are represented by X (optimization variables) and X_e is the excitation vector corresponding $\mathrm{B}_{1,e}^{+}$ field pattern. The excitation vector employed in the MRI experiments was determined by multiplying the calibration coefficients with the excitation vectors derived from the simulations.

The effectiveness of the GA-driven shimming was evaluated in multiple scenarios involving changes in the implant's orientation. Various orientations were established through a spherical coordinate system, where the origin was aligned with the center of the implant, and θ and φ denoted the azimuthal and polar angles, respectively. The results obtained using the GA approach were compared to those of the CP and OP reference methods as benchmarks.

2.2.5 RF Hardware

The initial values of the tuning and matching network were obtained from simulations and then fine-tuned to achieve a target of -15 dB for all scattering parameters (reflections and transmissions) in the RF transceiver array during manufacturing. In the phantom experiments, a multi-channel device (MRI.TOOLS GmbH, Berlin, Germany) was used to interface between the RF transceiver was to a 7.0 T MRI scanner (Magnetom, Siemens, Erlangen, Germany). The interface device included transmit-receive switches and RF power dividers. The MRI scanner operated in 8-channel pTx mode, allowing precise and independent control over the magnitude and phase of the channels.

3 Results

This chapter contains and uses results of my research that have been published in:

- **Paper 1**
  Jonathan Espiritu, Mostafa Berangi, Christina Yiannakou, Eduarda Silva, Roberto Fran-cischello, Andre Kühne, Thoralf Niendorf, Sören Könneker, Regine Willumeit-Römer, Jan-Marten Seitz, Evaluating metallic artefact of biodegradable magnesium-based im-plants in magnetic resonance imaging Bioactive Materials 15, 2022
- **Paper 2**
  Jonathan Espiritu, Mostafa Berangi, Hanna Cwieka, Kamila Iskhakova, Andre Kuehne, D.C. Florian Wieland, Berit Zeller-Plumhoff, Thoralf Niendorf, Regine Willumeit-Römer, Jan-Marten Seitz, Radiofrequency induced heating of biodegradable orthopedic screw implants during magnetic resonance imaging, Bioactive Materials 25, 2023
- **Paper 3:**
  Mostafa Berangi, Andre Kuehne, Helmar Waiczies and Thoralf Niendorf, MRI of Implantation Sites Using Parallel Transmission of an Optimized Radiofrequency Excitation Vector, Tomography 9(2), 2023
- **Abstract 1:**
  Mostafa Berangi, Andre Kuehne, Helmar Waiczies and Thoralf Niendorf “Excitation vector optimization for safe parallel transmission MRI of passively conducting implants in the presence of motion”, Joint Annual Meeting ISMRM-ESMRMB & ISMRT 31st Annual Meeting ISMRM, 2022, London. Abstract 2628.

and therefore, contains text, statements, passages and figures from these publications.

3.1 MR characteristics of titanium vs magnesium based implants

Differences between titanium (Ti) and magnesium (Mg) samples were observed by varying various MRI scanning parameters. The Mg samples consistently exhibited significantly fewer artifacts compared to the Ti samples across different main magnetic field strengths. In terms of sequence type, turbo spin echo sequences resulted in lower artifacts compared to gradient echo sequences. The averaged measurements of artifact diameter and length are summarized in Figure 5 illustrates the average distortions or artifacts based on the material and magnetic field strength. Increasing the magnetic field strength led to larger artifacts for both materials. In general, the use of Ti material and gradient echo sequences resulted in higher distortions compared to the use of Mg material and turbo spin echo sequences. Examining the influence of corrosion time on the size of artifacts caused by a Mg-based implant revealed statistically significant results. Regardless of magnetic field strength, a consistent decrease in image distortion was noted with extended in vitro corrosion times of the implant.

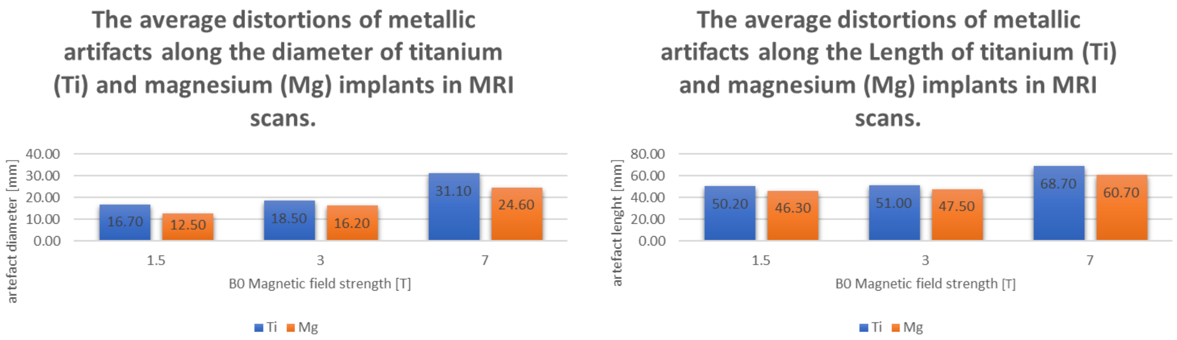

Figure 5: Measurements of the averaged MRI artefact extent in the screw samples. The distortions along diameter (left) and length (right) of Ti- and Mg- based screws in MRI are shown. (Modified from Jonathan Espiritu, Mostafa Berangi, Christina Yiannakou, Eduarda Silva, Roberto Francischello, Andre Kuehne, Thoralf Niendorf, Sören Könneker, Regine Willumeit-Römer, Jan-Marten Seitz, "Evaluating metallic artefact of biodegradable magnesium-based implants in magnetic resonance imaging", Bioactive Materials 15,2022, [41])

, [25])

3.2 Assessment of RF heating during an MRI examination

Findings from the heating measurements conducted during MRI examinations are summarized in Figure 6. An increase in corrosion time resulted in a decrease in the maximum temperature change (ΔT), although no clear quantitative correlation was evident. Non-degraded sample (0 weeks of corrosion, with 100% of the screw volume) induced the highest average temperature increase, while the sample at 3 weeks of corrosion had the lowest temperature increase. The maximum RF-induced heating was measured as ΔT = 1.20 ± 0.29 °C for the non-degraded Mg-based screw and ΔT = 1.16 ± 0.18 °C for the titanium equivalent. Nevertheless, there were no notable distinctions observed between them.

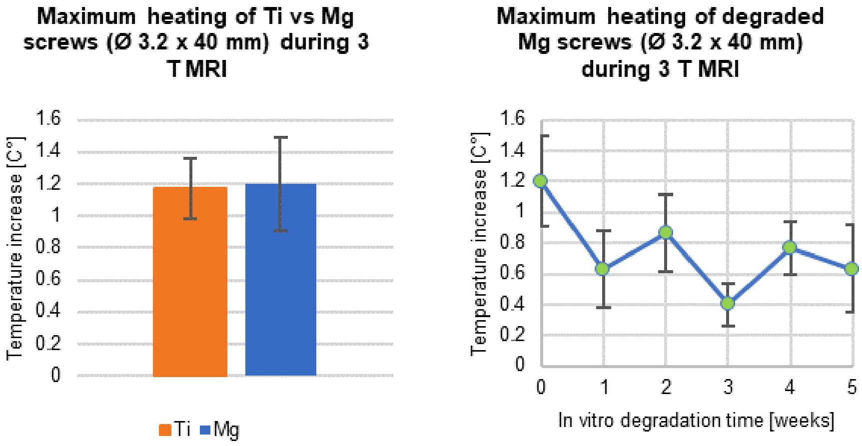

Figure 6: Maximum RF-induced temperature heating at the tip of the screws during MRI. Left: Comparison of Mg-based screw to commercial Ti-based equivalent screw. Right) A: influence of corrosion time on the maximum heating of biodegradable Mg-based screw. (Modified from Jonathan Espiritu, Mostafa Berangi, Hanna Cwieka, Kamila Iskhakova, Andre Kuehne, D.C. Florian Wieland, Berit Zeller-Plumhoff, Thoralf Niendorf, Regine Willumeit-Römer, Jan-Marten Seitz, “Radiofrequency induced heating of biodegradable orthopaedic screw implants during magnetic resonance imaging”, Bioactive Materials 25, 2023, [47])

3.3 EMF simulations of eight-channel RF transceiver configurations

The performance of eight configurations of RF transceiver arrays was evaluated by employing CP-mode, OP, and GA-derived transmission field shimming techniques. The maximum local specific absorption rate (SAR) limits the safety of each excitation. The strength and uniformity of the excitation vectors in the target region of interest (ROI) were assessed using mean value and the coefficient of variation parameter (COV) of the $\mathrm{B_1\_SAR_{max}}$. The results from electromagnetic field (EMF) simulations demonstrate that the mean $(\mathrm{B_1\_SAR_{max}})$ increases from configuration A to E and from F to H with GA-based shimming (Figure 7). The mean $(\mathrm{B_1\_SAR_{max}})$ across all configurations for GA, CP, and OP is 0.42 ± 43% (µT/√(W/kg)), 0.44 ± 9.4% (µT/√(W/kg)), and 0.22 ± 21% (µT/√(W/kg)), respectively.

Expanding the width of the loop elements utilized in configurations A-D leads to an increase in the mean value of $(\mathrm{B_1\_SAR_{max}})$ for every transmission field shimming approach (except for the CP mode in D) as shown in Figure 7. The mean$(\mathrm{B_1_SAR_{max}})$ obtained for GA versus CP transmission field shimming (%(MeanGA/MeanCP − 1) = −3.6% (A), −9.9% (B), −10.9% (C), and 16.8% (D)) and OP versus CP transmission field shimming (%(Mean$_{OP}$/Mean$_{CP}$ − 1) = −54.6% (A), −54.1% (B), −49.8% (C), and −33.2% (D)) reveals that the OP approach is inferior to the CP and GA approaches.

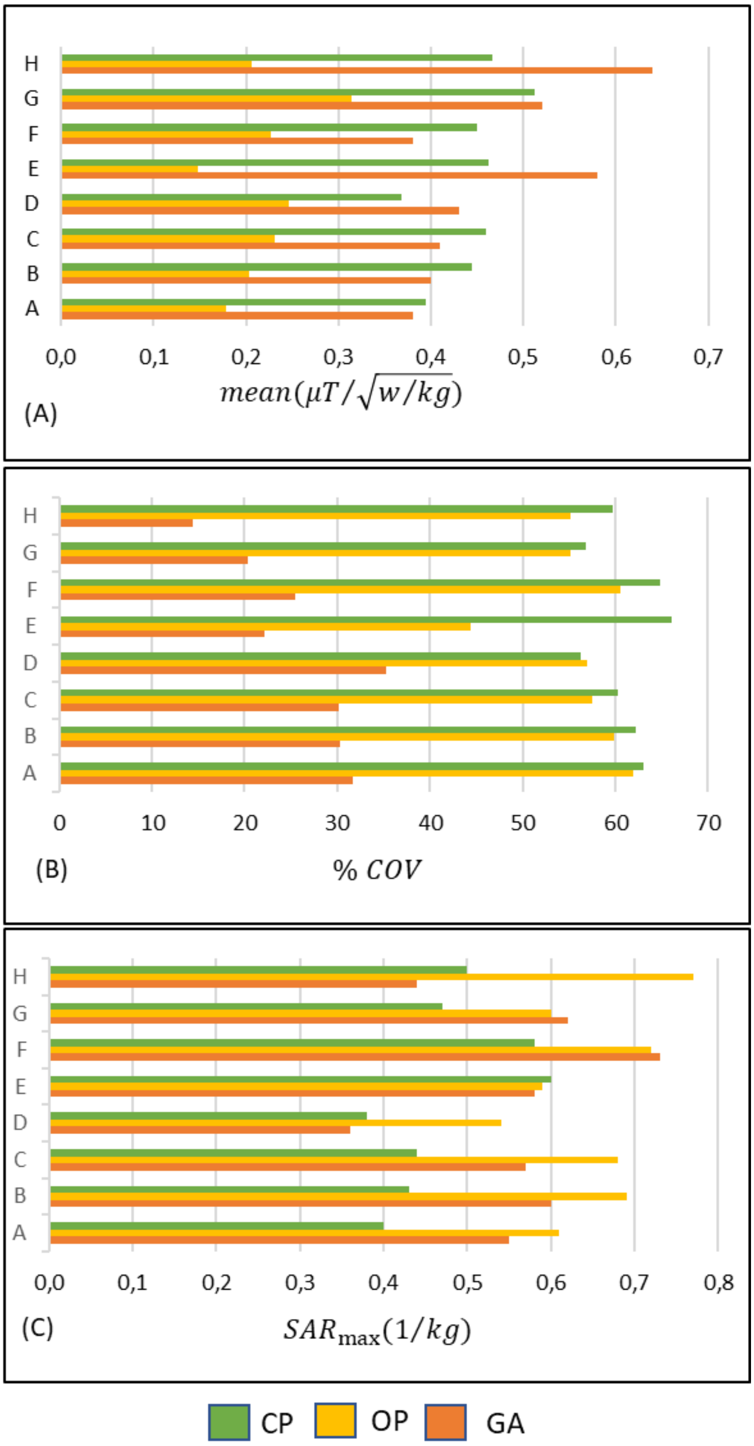

Figure 7: Comparative performance analysis of the eight different designs (A-H) of eight-channel RF transceiver configurations proposed in this thesis, employing circular polarization (CP), orthogonal projection (OP), and multi-objective genetic algorithm (GA) for transmission field shimming. (A) The mean $(\mathrm{B}_1\_\mathrm{SAR}_{\max})$ and (B) %COV $(\mathrm{B}_1\_\mathrm{SAR}_{\max})$ within the region of interest. (C) The maximum 10-gram averaged SAR throughout the entire phantom. (Modified

from Berangi, Mostafa, Andre Kuehne, Helmar Waiczies, and Thoralf Niendorf. "MRI of Implantation Sites Using Parallel Transmission of an Optimized Radiofrequency Excitation Vector" Tomography 9 (2), 2023, [52])

Evaluation of the homogeneity of $\mathrm{B_1\_}SAR_{\mathrm{max}}$ demonstrated that, except for configuration E, the OP algorithm achieved a comparable level of transmission field uniformity to that of the CP algorithm across all eight RF array configurations. However, the GA approach significantly improved the uniformity of the transmission field pattern compared to both the OP and CP methods (Figure 7_B).
The analysis of RF power deposition revealed that the average SAR10g,max (at 1 W input power) remained below 0.8 (W/kg) for all configurations of the RF transceiver array and the different RF transmission field shaping approaches (Figure 3C). In most cases, the circular polarization (CP) method resulted in lower SAR values compared to the multi-objective genetic algorithm (GA) or orthogonal projection (OP) approaches. The SAR values obtained from the GA approach were either similar to or lower than those obtained from the OP algorithm. Notably, for the loop-dipole (H) configuration, the maximum SAR10g,max obtained using the GA approach was 12% lower than that of the CP approach and 43.8% lower than that of the OP approach (Figure 7_C).
The implementation of the orthogonal projection (OP) algorithm effectively eliminated the occurrence of hot spots caused by the circular polarization (CP) mode. However, our simulations revealed that in certain scenarios, the OP excitation vectors resulted in a superficial SAR10g,max value outside of the implantation site, while still maintaining a maximum SAR10g,max within the range of results obtained from the CP mode.

By employing the multi-objective genetic algorithm (GA) for transmission field shimming, A 15.8% increase in SAR10g,max is observed for the eight-loop-dipole configuration (H) compared to the lowest SAR value among all configurations and shimming approaches (which was obtained in configuration D with CP shimming). However, this elevated SAR10g,max was counterbalanced by achieving the highest mean(of $\mathrm{B_1\_SAR_{max}}$) among all configurations and shimming approaches (25% greater than the second highest mean(of $\mathrm{B_1\_SAR_{max}}$) in configuration F with CP) and the most uniform excitation pattern of $\mathrm{B_1\_}SAR_{\mathrm{max}}$ (with a 67.6% lower coefficient of variation than the lowest observed with the OP algorithm in design G) within the target region of interest (ROI) that encompassed the implant.

3.4 Phantom MR Experiments

After conducting electromagnetic field (EMF) simulations, the eight-loop-dipole configuration (H) was chosen as the optimal design for fabricating an RF transceiver array for subsequent phantom experiment. Figure 8 illustrates the computer-aided design (CAD) representation and a photograph of the manufactured prototype of the selected configuration H. Additionally, the figure showcases the phantom container and power splitters utilized for feeding the RF array.

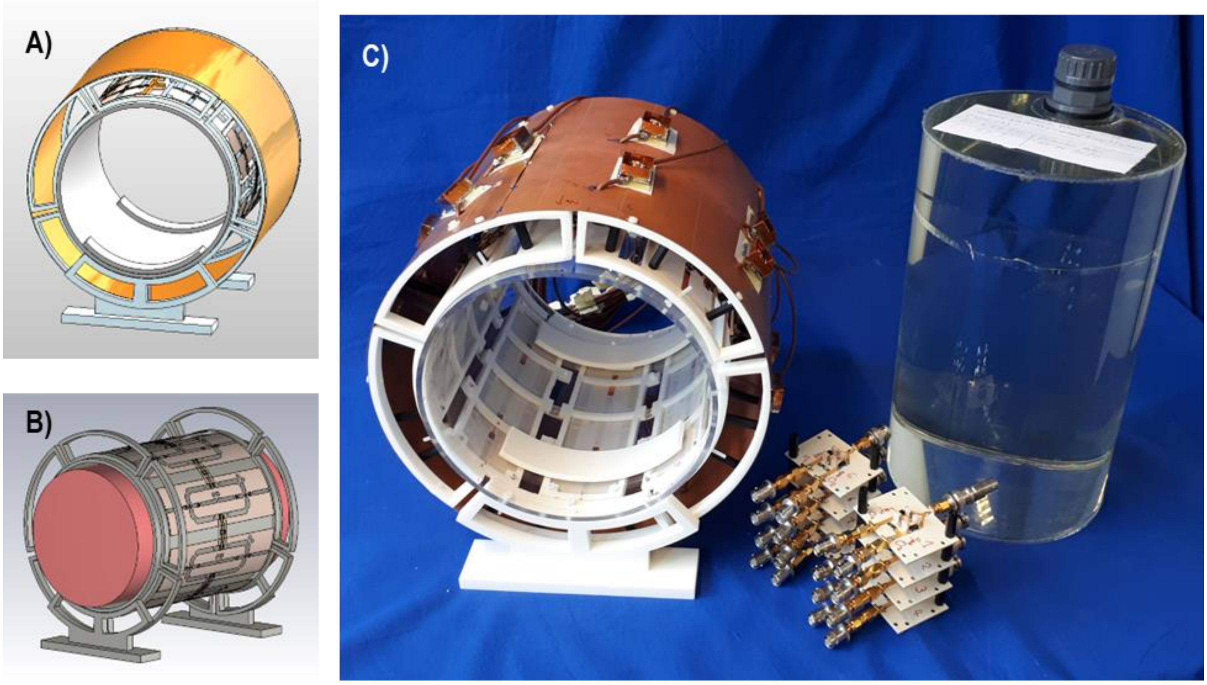

Figure 8: Experimental setup of the eight-channel loop-dipole RF transceiver array. (A, B) Computer-aided design representation of the RF transceiver array showcasing the loop-dipole configuration with decoupling transformers. (C) Photograph of the manufactured eight-channel loop-dipole RF transceiver array, including the phantom and the power splitters used for RF feeding of the array. (Modified from Berangi, Mostafa, Andre Kuehne, Helmar Waiczies, and Thoralf Niendorf. "MRI of Implantation Sites Using Parallel Transmission of an Optimized Radiofrequency Excitation Vector" Tomography 9(2), 2023, [52])

To evaluate the performance of the GA-based shimming method compared to the CP and OP approaches, experiments were conducted using a PVP-based gel phantom with the eight-loop-dipole RF transceiver array configured as previously mentioned. The implant was positioned parallel to the long axis of the phantom to align with the E-field lines of the RF array, resulting in the highest SAR induction within the implant. The metrics investigated in this study were the strength and uniformity of the B_1^+ field (expressed in μT/√(kW)) in terms of mean and COV% of $B_1^+/\sqrt{P_{fwd.}}$, respectively, where $P_{fwd.}$ is the sum of the input power to all RF channels.

The experimental B_1^+ mapping results, accompanied by the corresponding B_1^+ maps obtained from EMF simulations are represented in Figure 9 . The ROI containing the implant is highlighted in red. The B_1^+ maps obtained from the EMF simulations and the phantom experiments exhibit good agreement. The simulated B_1^+ maps reveal that the CP approach exhibits asymmetry in the B_1^+field around the implant, characterized by a pronounced B_1^+ void on one side and an elevated B_1^+ on the opposite side. This asymmetry is mitigated when employing the OP algorithm, although it leads to a reduction in the B_1^+ field in close proximity to the implant. In contrast to the CP and OP approaches, the GA-derived transmission field vectors yield a uniform and increased B_1^+ field within the target ROI containing the implant.

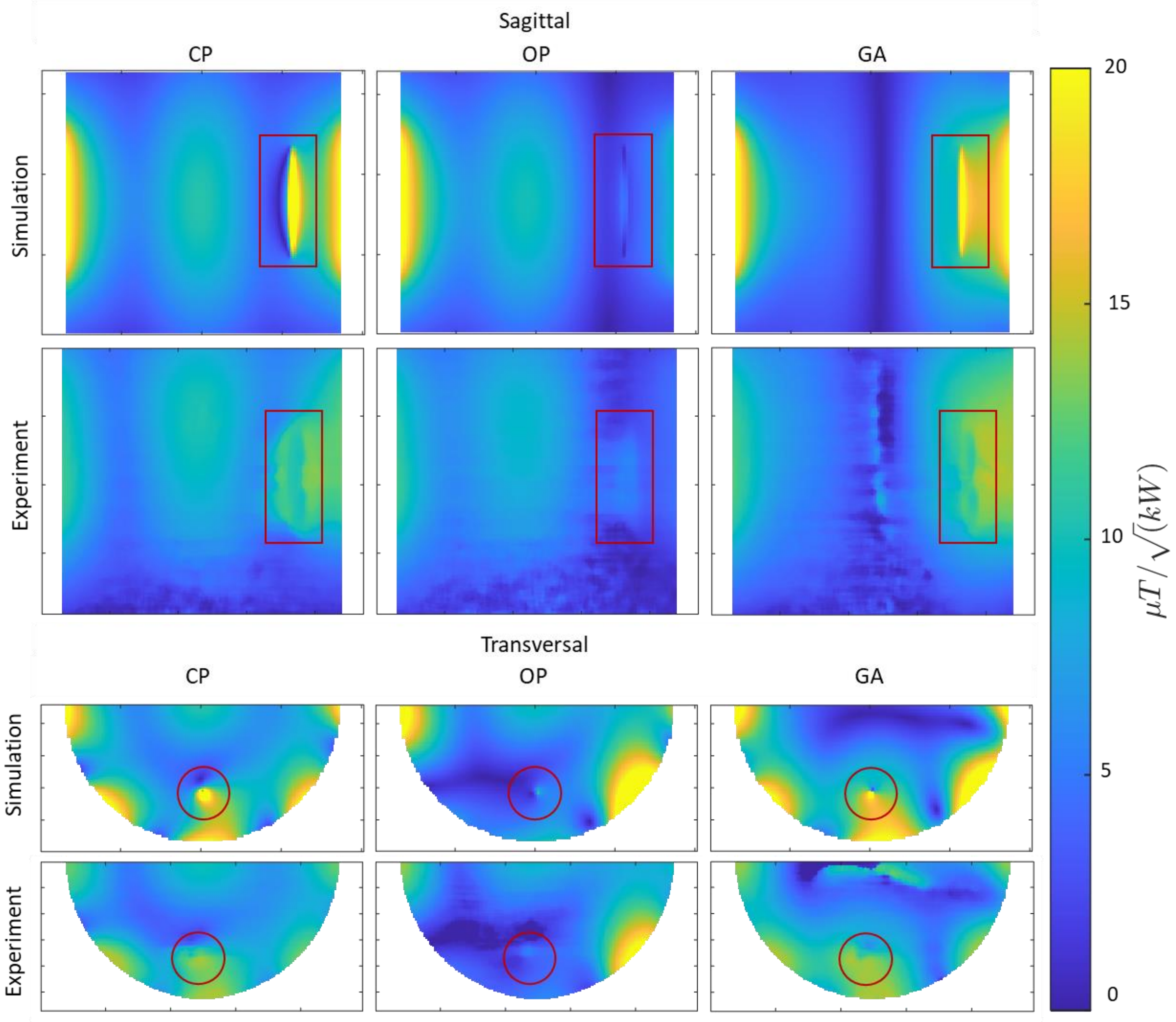

Figure 9*: Simulated and experimental outcomes for B_1^+ mapping using CP-, OP-, and GA-driven transmission field shimming algorithms are presented*. From top, the first and second rows present sagittal B_1^+ maps (encompassing the complete implant, including its tips) and the third and fourth rows show transversal B_1^+ maps (encompassing the areas with the most prominent RF distortion) derived from simulations and phantom experiments. The ROI containing the implant is indicated in red (figure from Berangi, Mostafa, Andre Kuehne, Helmar Waiczies, and Thoralf Niendorf. "MRI of Implantation Sites Using Parallel Transmission of an Optimized Radiofrequency Excitation Vector" Tomography 9(2), 2023, [52]).

Subsequently, the SAR elimination achieved with the GA is compared to the CP, employing point SAR maps along with the temperature difference maps obtained from both EMF simulations and phantom measurements. The OP-driven excitation vector was excluded from the heating measurements due to its weak and non-uniform B_1^+ field in the immediate vicinity of the sample implant. The simulated point SAR maps exhibited a similar pattern to the simulated E-field maps, as SAR is proportional to E^2. by aligning the implant parallel to the direction of the B_0, a strong coupling between the RF transceiver and the implant was observed where the implant behaved like a dipole antenna, resulting in elevated SAR values close to the tips of the sample implant. This effect arises from charge accumulation at the tips of the implant, leading to heightened SAR in close proximity to the implant. The movement of these charges along the implant's surface, known as induced currents, contributes to B_1^+ field inhomogeneities.

The SAR values achieved through the GA-based transmission field shimming approach were notably diminished in comparison to the CP mode, indicating a decreased induction of current on the implant using the GA-based approach (Figure 10). The decrease in SAR is accomplished by generating a diminished electric field in the proximity of the implant, mitigating the potential risks associated with excessive power deposition.

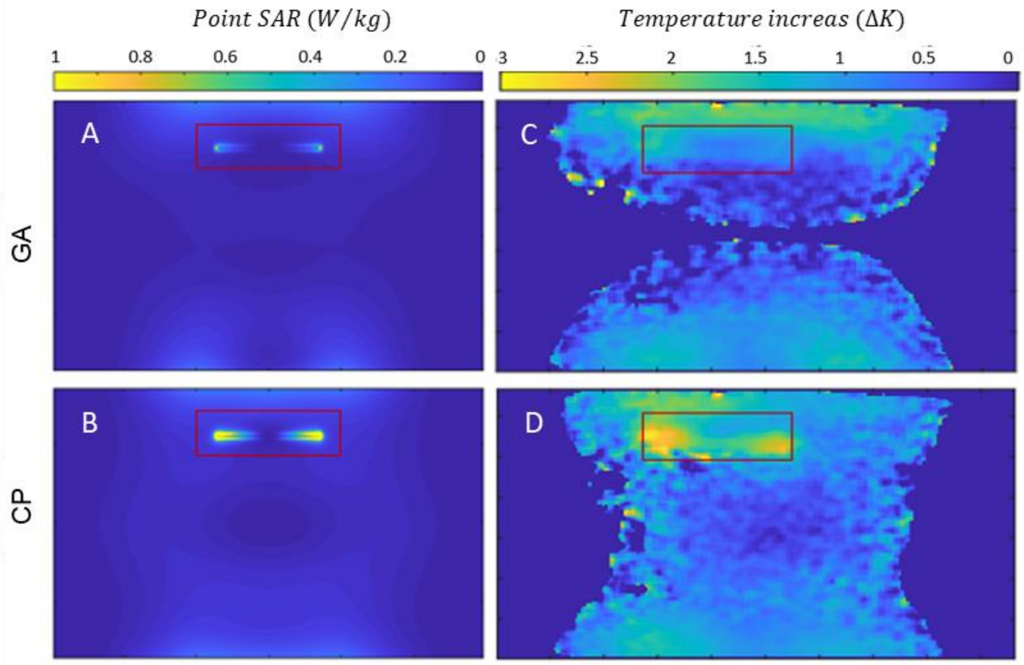

Figure 10: Maximum value of the simulated point SAR maps projected on the sagittal view of the phantom using GA-based (A) and CP-based (B) transmission field shimming for 1 W input power. Phantom experiment results of the temperature increase maps for a sagittal view using the GA-based (C) and CP-based (D) shimming. The region of interest (ROI) containing the implant is highlighted in red (figure from Berangi, Mostafa, Andre Kuehne, Helmar Waiczies, and Thoralf Niendorf. "MRI of Implantation Sites Using Parallel Transmission of an Optimized Radiofrequency Excitation Vector" Tomography 9(2), 2023, [52]).

The temperature difference maps derived from MR thermometry supported the SAR assessment results. The CP approach produced a temperature increase of ΔT = 2.5–

3.0 K at the implant's tips due to the induced transmission fields. In contrast, the GA approach generated transmission fields that did not contribute to any additional temperature rise around the implant (Figure 10). The temperature distribution in the vicinity of the implant was similar to the background temperature when using the GA approach.

B_1^+ maps were used to investigate the effect of different implant orientations relative to a reference position where the implant was oriented parallel to the long axis of the phantom. To facilitate repositioning, a liquid phantom material using sucrose was used. Implant orientations were defined in spherical coordinates with the implant center as the origin and polar (θ) and azimuthal (φ) angles determining the orientation. Transversal slices crossing the center of the implant were acquired as at the center of the implant the B_1^+ inhomogeneity induced by the implant is most prominent. Figure 11A (A–R) presents a summary of the B_1^+ maps obtained using CP, OP, and GA-based shimming algorithms. For an orientation of θ=90° and φ=0°, the implant-induced B_1^+ artifact was minimized (Figure 11A (J–L)). In this orientation, minimal current was induced on the implant due to the nearly parallel alignment of the RF transceiver array's E-fields with the implant's long axis. Other implant orientations exhibited significant B_1^+ inhomogeneities near the implant when using CP or OP transmission field shimming. The GA approach significantly improved B_1^+ uniformity. Regardless of the implant orientation, GA transmission field shimming consistently provided superior B_1^+ in terms of uniformity and strength compared to CP and OP transmission field shimming counterparts.

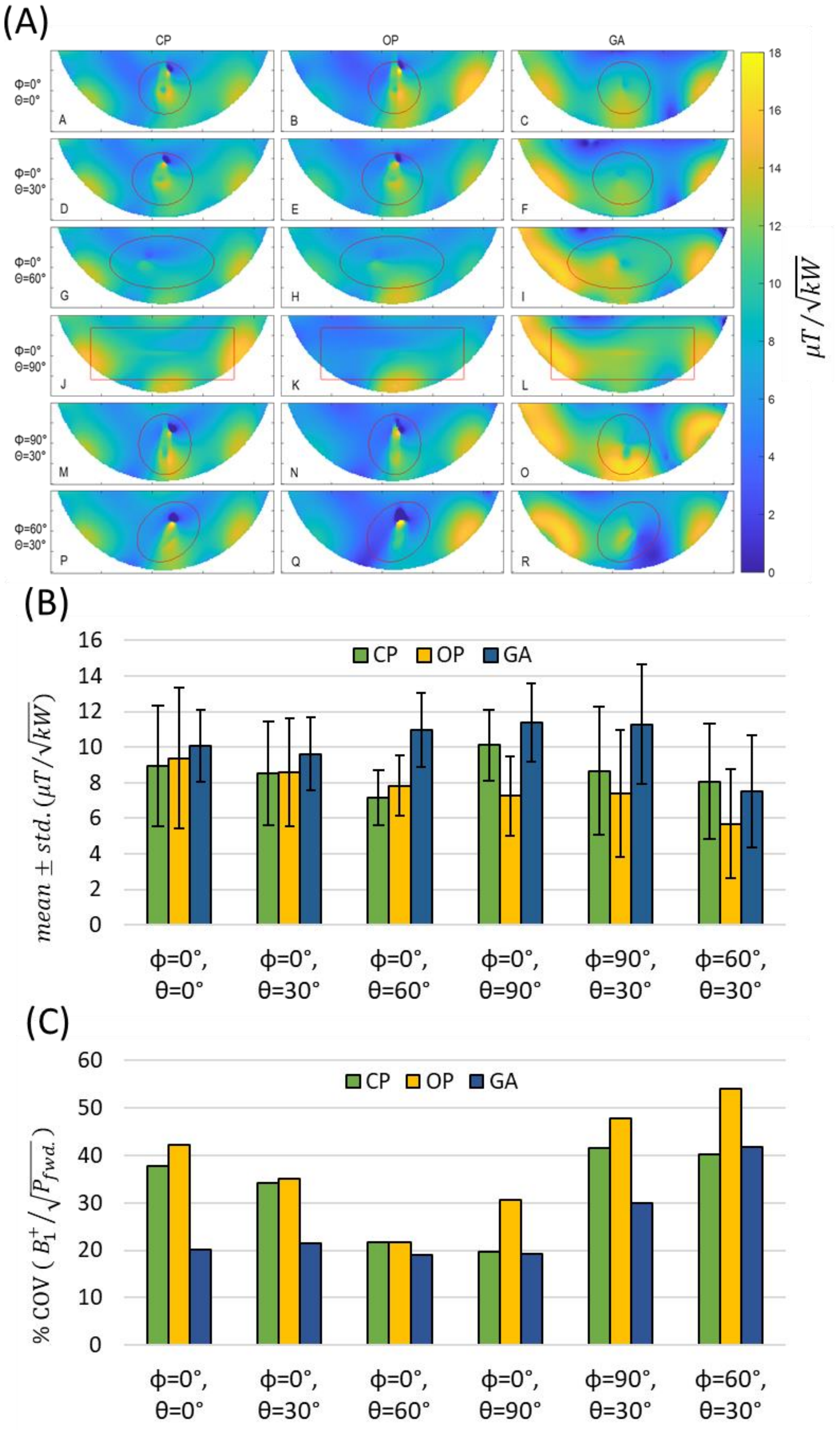

Figure 11: (A) The B_1^+ maps obtained using CP-, OP-, and GA-based transmission field shimming for various implant orientations (labeled from A to R). Implant orientation is defined in spherical coordinates (θ and φ) with the origin at the center of the implant. The red region indicates the ROI covering the implant in phantom. (B) Mean ± std. of $B_1^+/\sqrt{(\text{power}_{\text{Fwd.}})}$ and (C) Percentage coefficient of variation in $B_1^+/\sqrt{(\text{power}_{\text{Fwd.}})}$ within the ROI for different implant orientations using CP, OP, and GA transmission field shimming (figure from Berangi, Mostafa, Andre

Kuehne, Helmar Waiczies, and Thoralf Niendorf. "MRI of Implantation Sites Using Parallel Transmission of an Optimized Radiofrequency Excitation Vector" Tomography 9 (2), 2023, [52]).

3.5 MRI of Implants Using a High Spatial Resolution

To evaluate the clinical feasibility of transmission field shimming, a 3D gradient-echo MRI scan with specific imaging parameters (TR = 20 ms, TE = 2.7 ms, FA = 20°, isotropic spatial resolution = 0.5 mm^3, matrix size = 512 × 512 × 104, TA ≈ 17 min, receiver bandwidth = 501 Hz/Px) is conducted. The eight-loop-dipole configuration (H) was employed, along with excitation vectors derived from the CP, OP, and GA methods. From the acquired 3D data, imaging planes containing the implant and B_1^+ artifacts were manually selected using a custom MATLAB script. By utilizing minimum-intensity projection (MinIP), 2D MinIP images (Figure 12) were generated to highlight potential destructive interference in the vicinity of the implant. When employing CP and OP algorithms for transmission field shimming, a bow shaped B_1^+ artifact emerged near the implant. However, the GA transmission field shimming technique effectively eliminated B_1^+ artifacts, resulting in uniform images around the implant (Figure 12).

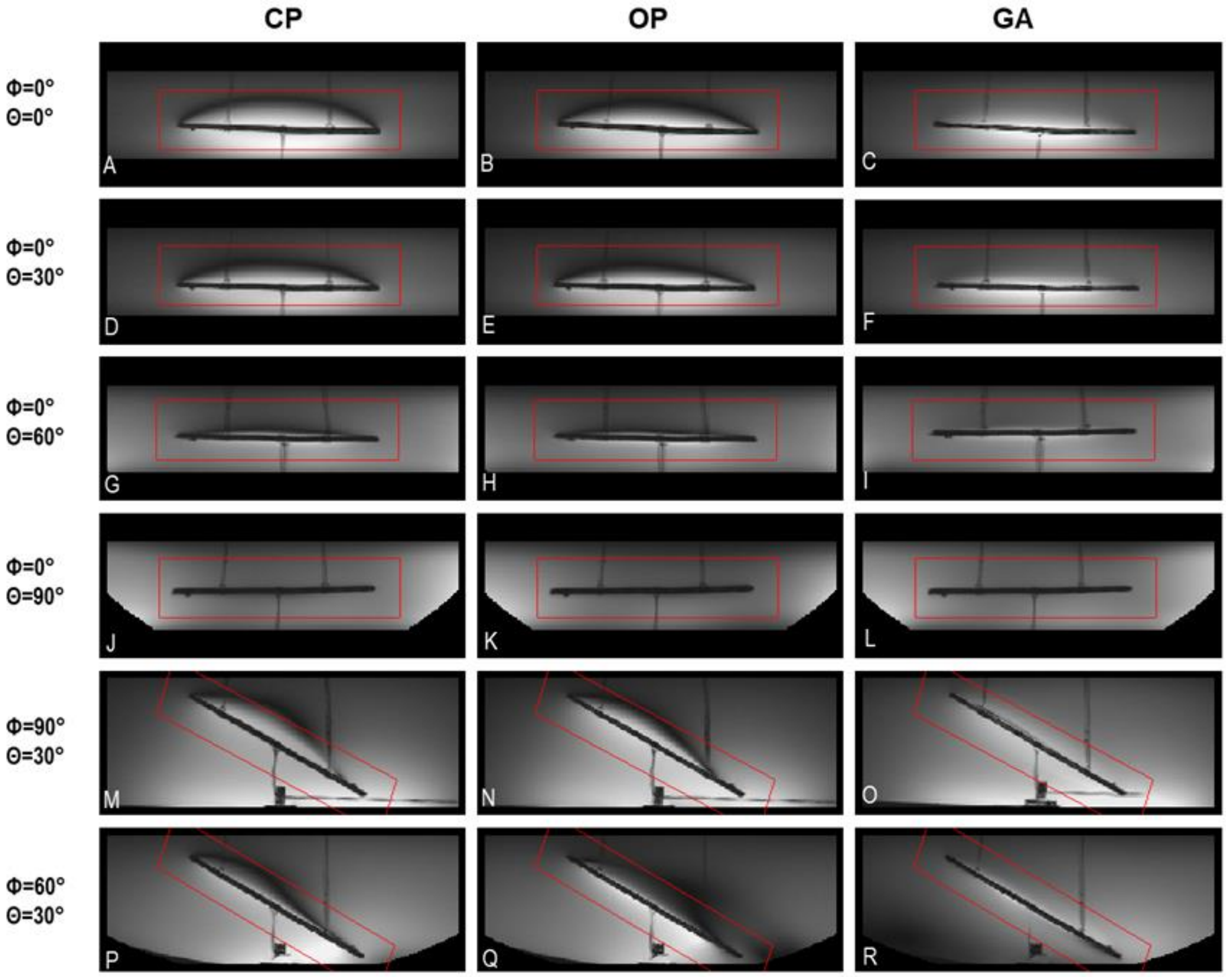

Figure 12: Minimum-intensity projections of B_1^+ artifacts near the implant obtained from 3D gradient-echo MRI. The B_1^+ artifacts were evaluated using CP-, OP-, and GA-based transmission field shimming techniques for various implant orientations (labeled A-R), corresponding to the excitation vector displayed in Figure 11. Implant orientation is defined using polar and azimuthal angles in spherical coordinates, with the origin at the center of the implant. The red region indicates the ROI under investigation (figure from Berangi, Mostafa, Andre Kuehne, Helmar Waiczies, and Thoralf Niendorf. "MRI of Implantation Sites Using Parallel Transmission of an Optimized Radiofrequency Excitation Vector" Tomography 9 (2), 2023, [52]).

3.6 EMF Simulations in a Realistic Human Voxel Model

The simulation utilized the eight-loop-dipole configuration (H) to replicate a realistic human model (Duke [64]), incorporating a sample screw (L = 70 mm, outer diameter D_{out} = 1 mm) implanted in the right tibia. For transmission field shaping (B_1^+ shimming), the GA approach was employed with the specific properties outlined in the transmission field shaping section. A cylindrical ROI (L = 110 mm, D = 40 mm) was defined for the analysis. To assess B_1^+ strength, uniformity within the ROI, and SAR reduction, the CP method was used as a benchmark. The results are depicted in Figure 13.

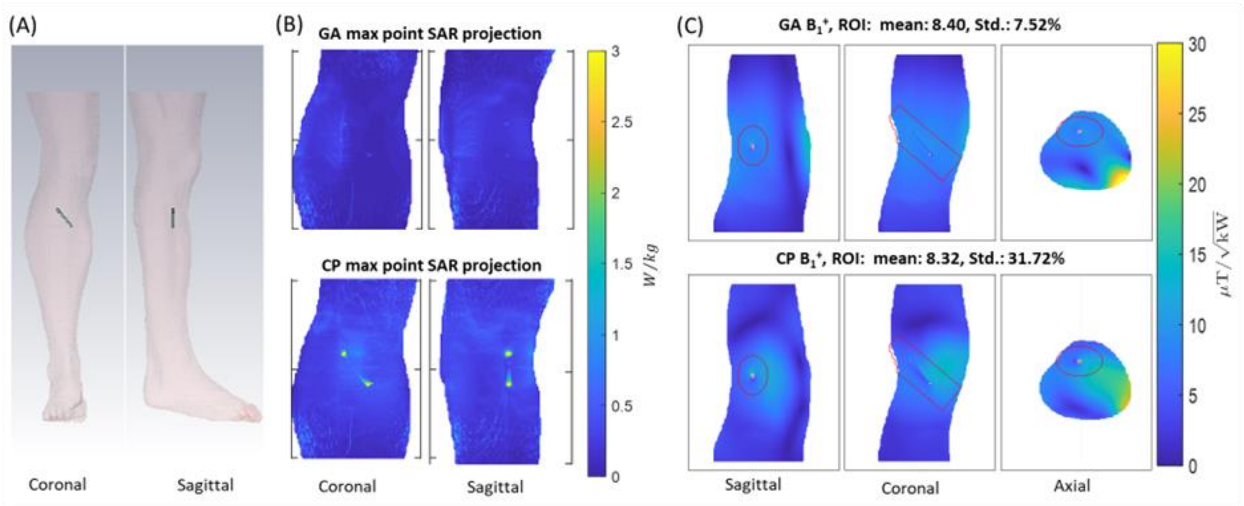

Figure 13: EMF simulation setup and results for sample screw implant in the tibia. (A) Setup overview illustrating the positioning of the sample screw implant within the tibia of the Duke human voxel model. (B) Maximum point SAR projections obtained for the GA (top) and CP (bottom) approaches with 1 W input power. (C) B_1^+ maps derived from slices through the center of the implant using the GA (top) and CP (bottom) approaches. The red region indicates the ROI of interest (figure from Berangi, Mostafa, Andre Kuehne, Helmar Waiczies, and Thoralf Niendorf. "MRI of Implantation Sites Using Parallel Transmission of an Optimized Radiofrequency Excitation Vector" Tomography 9 (2), 2023, [52]).

3.7 Robustness of the transmission field shimming against small implant displacement

Electromagnetic simulations using the eight-loop-dipole configuration (H) were performed and further processed using in-house MATLAB scripts. A cylindrical shape implant (R=2mm, L=70mm) was placed parallel to the phantom's long axis. By aligning the origin of the coordinate system with the center of the phantom (Figure 14_top), the center of the implant was placed at (x=0, y=-55 mm, z=0). B_1^+ field optimization was performed, and an optimum excitation vector (ev) was derived from the GA approach, used as a base ev and applied to scenarios where the implant is rotated and/or shifted with respect to its initial orientation/position. The scenarios used in the simulations are summarized in Table 2 where the position of the center of the implant is defined in Cartesian coordinates while variations in the implant's orientations are defined by a spherical coordinate system. The resulting B_1^+ and SAR maps were calculated, and the performance of the method was benchmarked against a circular polarization (cp) shim vector.

Figure 14 (bottom) shows transversal B_1^+ maps through the center of the implant and maximum projection point SAR maps obtained for GA and cp excitation vectors using the geometrical setups outlined in Table 2. The target ROI encompassing the implant is highlighted with a black contour. It is shown that CP B_1^+ shimming suffers from deficient B_1^+ in the vicinity of the implant due to strong signal voids in this region. From the safety perspective, the CP induces significant SAR elevation close to the implant tips which may result in hazardous risks of tissue burn. The optimized shim pattern derived from GA was able to eliminate the B_1^+ inhomogeneities for several implant orientations. The GA approach also yielded only minor SAR elevation close to the implant. These results demonstrate that the GA approach outperformed the CP for B_1^+ and SAR. In detail, the extreme case of the geometrical setup 5 ($\theta=7^0$, $\phi=45^0$) showed a maximum point SAR generated by the CP approach which was 709% higher than maximum point SAR facilitated by the GA approach. For the same setup, mean B_1^+ provided by the CP approach was 30% inferior to that supported by the GA approach.

Table 2: Experimental implant orientations used in the EMF simulations for assessing the robustness of the GA-based transmission field shimming against small implant displacement. Second column corresponds to the position of the implant's center relative to the origin of the coordinate system (phantom's center) as shown in Figure 14. The last two columns define the orientation of the implant using polar and azimuthal coordinate system.

	Implant centre	Polar angle (With respect to z)	Azimuthal angle (With respect to x)
Experiment	[x, y, z] mm	θ°	φ°
1	[0, -60, 0]	7	-45
2	[0, -55, 0]	0	-
3	[0, -55, 0]	15	-90
4	[0, -55, 0]	21	-44
5	[0, -55, 0]	7	-45
6	[0, -45, 0]	0	-

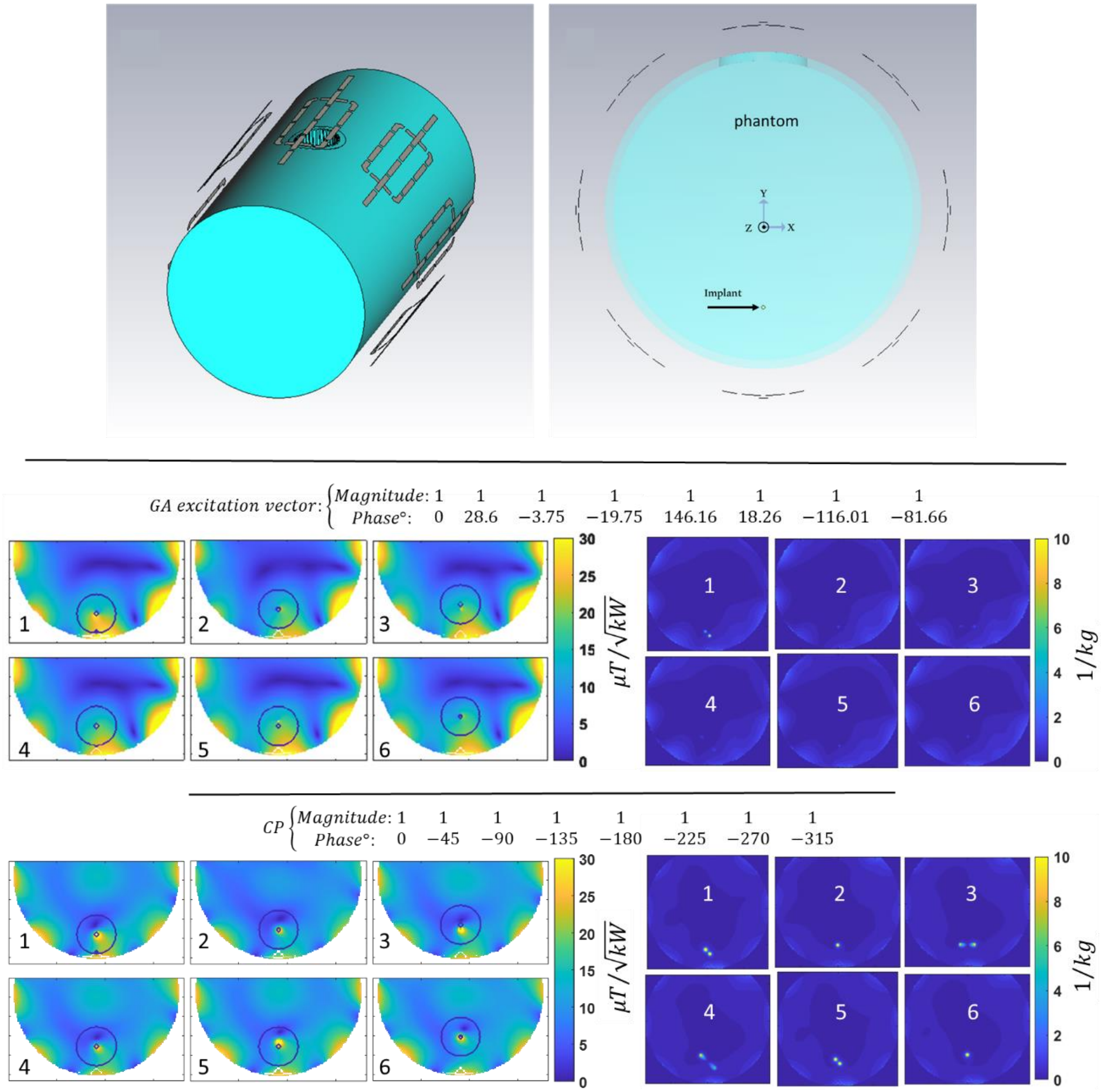

Figure 14: Assessment of small implant movements on GA against CP. Top) The simulation setup, showing the implant position and the definition of the coordinate system. Bottom) B_1^+ maps (left) and maximum projection maps of point SAR (right) derived from the GA approach (top row) and the CP approach bottom row) using the experimental setups in Table 2.

4 Discussion

This chapter contains and uses results of my research that have been published in:

- **Paper 1**
  Jonathan Espiritu, Mostafa Berangi, Christina Yiannakou, Eduarda Silva, Roberto Francischello, Andre Kühne, Thoralf Niendorf, Sören Könneker, Regine Willumeit-Römer, Jan-Marten Seitz, Evaluating metallic artefact of biodegradable magnesium-based im-plants in magnetic resonance imaging Bioactive Materials 15, 2022
- **Paper 2**
  Jonathan Espiritu, Mostafa Berangi, Hanna Cwieka, Kamila Iskhakova, Andre Kuehne, D.C. Florian Wieland, Berit Zeller-Plumhoff, Thoralf Niendorf, Regine Willumeit-Römer, Jan-Marten Seitz, Radiofrequency induced heating of biodegradable orthopedic screw implants during magnetic resonance imaging, Bioactive Materials 25, 2023
- **Paper 3**
  Mostafa Berangi, Andre Kuehne, Helmar Waiczies and Thoralf Niendorf, MRI of Implantation Sites Using Parallel Transmission of an Optimized Radiofrequency Excitation Vector, Tomography 9(2), 2023

❖ **Abstract 1**
Mostafa Berangi, Andre Kuehne, Helmar Waiczies and Thoralf Niendorf “Excitation vector optimization for safe parallel transmission MRI of passively conducting implants in the presence of motion”, Joint Annual Meeting ISMRM-ESMRMB & ISMRT 31st Annual Meeting ISMRM, 2022, London. Abstract 2628

and therefore, contains text, statements, passages and figures from these publications.

Postoperative care in orthopaedic surgery relies on precise imaging techniques to monitor bone healing, implant placement, and to ensure appropriate mechanical and physiological responses between the host and the implant. Early-stage research of biomaterials focuses on assuring these responses, while later stages require insights into product application, translational aspects, and medical imaging compatibility. The increasing number of orthopaedic implantations drives the need for post-surgery imaging, particularly MRI, which offers excellent bone-tissue contrast. However, a careful risk assessment of RF-induced heating of conducting implants is essential before utilizing MRI for monitoring implantation sites. This study contributes to the literature and pushes the boundaries of the state-of-the art by examining material characteristics, corrosion dynamics, and the influence of the degradation layer on RF-induced heating specifically in Mg-based implants, addressing a significant need and opportunity in the field. Furthermore, the possibility of achieving safe and distortion-free MRI at 7.0 T in the presence of metallic implants is investigated. This is accomplished by employing parallel radiofrequency transmission along with excitation vector optimization. The performance of eight different radiofrequency array configurations including loop elements and fractionated dipoles is evaluated based on metrics such as maximum 10g-average specific absorption rate (SAR10g,max), transmission field strength, and uniformity.

4.1 Summary of main results

In contrast to conventional titanium and stainless-steel materials, Mg-based implants undergo degradation over time when exposed to bodily fluids. Consequently, the chemical composition and physical geometry of the implant change during the healing process. Since material composition and the shape of the implant influence the RF-heating and artefact of metallic implants, our study used various imaging scenarios to characterize in vitro corroded Mg-based screws. It is important to acknowledge that the in vitro degradation technique utilized in this study offers only a limited representation of the intricate processes involved in degradation within the human body. This is due to our in vitro approach not considering the impact of biological material or cell adhesion [65]. During the degradation of Mg within the body, the underlying metallic material corrodes, giving rise to non-metallic degradation layers primarily composed of MgO and $Mg(OH)_2$ [66]. Introducing corrosion time as a parameter reveals a reduction in artifact production as the implant undergoes in vitro degradation. This decrease in artifact size is confirmed by our results obtained for a range of in vitro corrosion times.

The EMF simulations illustrated that utilizing the RF array configuration with eight loop-dipole channels, driven by optimized transmission field patterns obtained from a multi-objective GA, resulted in the strongest and most uniform transmission field B_1^+ within a specific region of interest (ROI) containing the implant. By utilizing B_1^+ mapping, MR thermometry, and 3D gradient-echo imaging on a muscle tissue-like phantom, it Is shown that the combination of the eight-channel loop-dipole RF array and the multi-objective GA effectively reduces implant-induced SAR and achieves the necessary uniformity of the transmission field for monitoring tissue healing and assessing the degradation of metallic implants using MRI. Although our study was conducted at 7.0 T, this approach can be readily adapted to other available pTx systems at different magnetic field strengths, such as 3.0 T and 1.5 T, as well as higher field strengths like 10.5 T or 14.0 T. Opting for dynamic pTx rather than static pTx would further improve the transmission field, especially in the presence of implants. While our clinical example focused on screw implants for bone fracture fixation in body extremities to demonstrate the proof of principle, our methodology can be conveniently applied to other body regions by customizing RF arrays for those specific regions.

4.2 Interpretation of results

Examining the electromagnetic properties of the degradation layer can provide insights into how it influences artifact production. Mainly composed of $Mg(OH)_2$ [67], the degradation layer consists of non-eclectically conducting material. Thus, the degradation layer might be considered as separation gap between metallic material and surrounding tissue which reduces the unwanted implant induced effects on implantation site. On the other hand, as the scattering magnetic and electric fields of the implant are reduced by distance from the implant hence the presence of this separation layer reduces the strength of the scattering fields sensed by the tissues in the implantation site.

The application of the CP excitation approach near the implant leads to the emergence of B_1^+ artifacts and excessive SAR caused by the implant. Conversely, the OP method can mitigate implant-induced SAR, albeit with the trade-off of B_1^+ degradation at the implant site, leading to uneven image intensity. Our findings indicate that the utilization of the GA-based approach effectively addresses both issues, making it a promising solution for safe clinical MRI of orthopedic implants without B_1^+ artifacts.

The GA-based transmission field shimming technique eliminates the impact of conducting implants on EMFs by suppressing RF-induced current on the implant surface. This is accomplished by establishing a region with a diminished electric field in the vicinity of the implant. Therefore, it is plausible to adapt the GA method for shaping the transmission field around other passive conducting devices, such as guide wires, standard titanium implants, intracoronary stents, catheters or metallic needles.

4.3 Critical consideration of the results versus the state of research

Heating caused by RF induction in conducting implants is influenced by the electromagnetic properties of the material and its physical geometry. In the body, elevated heating and artefact is more pronounced when the implant length is between half and a quarter of the RF wavelength (e.g., at 3.0 T ranging from 15 to 6.5 cm in tissue) [68]. While this range does not include the 40 mm length implants that were examined in this experiment. On the other hand, the uncoated and PEO-coated screws with lengths of 70 mm may be affected by this phenomenon. This observation is in accordance with our experiments, where the 70 mm un/coated Mg screw exhibits higher heating (1.6 °C and 2.1°C respectively) compared to the uncoated screw with a length of 40 mm (1.2 °C). Although no significant differences were found between the materials, the non-degraded implant displayed slightly increased RF heating compared to the titanium equivalent.

Simulations on the secondary E-field distribution of a linear implant while varying the material's conductivity revealed that increasing the conductivity of the material results in stronger scattered secondary field hotspots at the tips of the implant [69]. Considering that Mg-based implants exhibit higher conductivity compared to titanium [70], this may explain the slightly elevation of measured heating. However, investigation studies on high electrically conducive material (such as copper, aluminum, and silver) substantiated the assumption that the current distribution on perfect electric conductors and high-conductivity materials can be considered equal [60]. Therefore, it is not expected that there will be significant differences in heating profiles between Mg-based and titanium materials, as illustrated in Figure 6.

4.4 Strengths and limitations of the study(s)

The investigation of Mg-based implant heating and artefact in the MRI faces limitations due to the inherent degradation properties of these implants. The reactive nature of Mg-based alloys prevents repeated testing of samples due to their interaction with the water-based phantom medium. Consequently, multiple samples need to be prepared for each time-point, which leads to variations in non-uniform corrosion. Furthermore, extended placement of the samples in the phantom is not possible as it would result in the formation of hydrogen gas bubbles. Although for the heating experiments, the area surrounding the temperature probes was confirmed to be bubble-free prior to measurements, sporadic formation of small millimetre-sized bubbles on the implant was observed as a result of the corrosion process. This concern highlights the need to revise the ASTM F2182 procedures to incorporate validated and standardized protocols for the mapping of the heating induced by radiofrequency (RF) in biodegradable materials.

It is important to note that our study on elimination of implant induced heating has focused and hence limited on high-spatial-resolution gradient-echo imaging using MRI. Further investigation into alternative MRI techniques like echo-planar imaging or fast-spin-echo imaging is necessary and justified. Also, the RF transmission channels are limited to eight independent radiofrequency power amplifiers (RFPA) with a peak output power of 1 kW each, due to the design of the MR scanner system utilized. However, the latest commercially accessible implementations can overcome this limitation by supporting up to sixteen RFPAs, offering adjustable RF output power of up to 2 kW. Moreover, pioneering scalable prototypes enable up to thirty-two independent signal generators, RFPAs, and RF chains, providing even greater potential for parallel transmission MRI of the body at 7.0 T [71, 72]. EMF simulations have also examined parallel transmission employing RF transceiver array setups comprising as many as 48 channels [73]. Therefore, employing more RF transmission channels enhances the degrees of freedom and offers greater flexibility in shaping the transmission field. This advancement is particularly advantageous for suppressing induced currents on implants of varying geometry or size, potentially improving the overall performance of the proposed approach. However, it's important to note that increasing the number of RF channels to cover the same region of interest necessitates smaller transceiver elements, leading to reduced load noise from each element, but also introducing additional coil resistance (e.g., through more copper, lumped elements, etc.), which limits the signal-to-noise ratio of MRI. Moreover, increasing the channel count leads to an augmented amount of the overall losses in the transmission path due to the increased need for cabling and circuit elements. Therefore, the optimal number of independent RF transmission channels for MRI of implants depends on the specific application, implant configuration, and target anatomy.

4.5 Implications for practical application and directions of future research

MRI aided monitoring of implantation sites in patients with (bio-degradable) implants present an under-estimated and under-investigated clinical challenge. While RF-induced heating caused by a set of several permanent implants has been examined, future studies should also consider the heating caused by multiple implants composed of biodegradable materials. Additionally, the impact of implant fractures on RF power deposition of non-degradable and biodegradable implants has not been investigated so far. Therefore, it is important to investigate the effect of these configurations on heating profiles of Mg-based implants, which may result in a safety hazard for patients.

Any implant fracture alters the electromagnetic response of the implant, potentially leading to severe SAR elevation compared to the non-fractured counterpart. This scenario could occur in vivo [74] and could pose additional safety risks. The RF power deposition phenomenon of a fractured implant can be attributed to the concept of fractioned dipole [75] with capacitors placed at the fractured sections, where strong electric fields are formed at the fractured section of the implant, potentially leading to significant SAR elevation.

Based on the findings of this thesis for the case of non-fractured implant, it is hypothesised that general excitation schemes such as CP yield magnification of RF power deposition in fractured implants. On the other hand, attributing the fractured implant to the case of fractured dipole, it is assumed that there may exist optimum excitations that induce less current on the implant and therefore are less susceptible to SAR amplification induced by implant fractures. These hypothesises require more in-depth investigations and further comprehensive research is necessary to define the influence of implant fractures and other real-life scenarios on the safety of MRI aided monitoring of implantation sites.

5 Conclusions

The findings obtained in this thesis project demonstrated that Mg-based screws show a decrease in metallic artefact production over time in various MRI experiments of different degradation time points. In comparison to titanium alternatives, the Mg-based material generated significantly lower artefacts, making it a promising candidate for future orthopedic solutions with suitable MRI compatibility. Additionally, my evaluation of RF-induced heating of Mg-based implants during MRI revealed that as corrosion time and degradation layer formation progressed, the degradation of Mg-based screws led to a reduction in RF-induced heating. This decrease in heating may be attributed to the formation of corrosion layer which acts as a non-conductive region making distance between the implant induced electric fields induced and tissue. As the SAR elevation corresponds to the elevated electric fields as a result of charge (i.e. electrons) accumulation at the tips of implant and this electric field decays with inverse square of distance from the charges, the corrosion layer might be considered as a separator region leading to less implant induced SAR on adjacent tissues. The non-degraded Mg-based sample posed the highest heating risk immediately after implantation, while RF-induced heating was similar between native Mg-based screws, surface-treated Mg-based screws with PEO, and titanium equivalents. These findings suggest the need for revised industry safety standards to include testing of conducting medical devices using methodologies tailored for biodegradable materials. Additional clinical research is needed to assess degradation rates based on the extent of artifacts and to investigate alternative methods for monitoring degradation.

Reference list

1. Bernd Heublein, Roland Rohde, Volker Kaese, Matthias Niemeyer, W. Hartung, and Axel Haverich, *Biocorrosion of magnesium alloys: a new principle in cardiovascular implant technology?* Heart (British Cardiac Society), 2003. **89**(6): p. 651-656.
2. Gemma Marcucci and Maria Luisa Brandi, *Kyphoplasty and vertebroplasty in the management of osteoporosis with subsequent vertebral compression fractures.* Clin Cases Miner Bone Metab, 2010. **7**(1): p. 51-60.
3. Navdeep Singh, Uma Batra, Kamal Kumar, Neeraj Ahuja, and Anil Mahapatro, *Progress in bioactive surface coatings on biodegradable Mg alloys: A critical review towards clinical translation.* Bioact. Mater., 2022. **19**(NA): p. 717-757.
4. Ramachandran Krishnan, Selvakumar Pandiaraj, Suresh Muthusamy, Hitesh Panchal, Mohammad S. Alsoufi, Ahmed Mohamed Mahmoud Ibrahim, and Ammar Elsheikh, *Biodegradable magnesium metal matrix composites for biomedical implants: synthesis, mechanical performance, and corrosion behavior – a review.* J MATER RES TECHNOL, 2022. **20**(NA): p. 650-670.
5. Jonathan Espiritu, Martin Meier, and Jan-Marten Seitz, *The current performance of biodegradable magnesium-based implants in magnetic resonance imaging: A review.* Bioact. Mater., 2021. **6**(12): p. 4360-4367.
6. Hasan May, Yusuf Alper Kati, Gurkan Gumussuyu, Tuluhan Yunus Emre, Melih Unal, and Ozkan Kose, *Bioabsorbable magnesium screw versus conventional titanium screw fixation for medial malleolar fractures.* J Orthop Traumatol, 2020. **21**(1): p. 1-8.
7. Christian Plaass, Christian von Falck, Sarah Ettinger, Lena Sonnow, Franco Calderone, Andreas Weizbauer, Janin Reifenrath, Leif Claassen, Hazibullah Waizy, Kiriakos Daniilidis, Christina Stukenborg-Colsman, and Henning Windhagen, *Bioabsorbable magnesium versus standard titanium compression screws for fixation of distal metatarsal osteotomies - 3 year results of a randomized clinical trial.* J Orthop Sci, 2017. **23**(2): p. 321-327.
8. Roland Biber, Johannes Pauser, M. H. Brem, and Hermann Josef Bail, *Bioabsorbable metal screws in traumatology: A promising innovation.* Trauma Case Rep., 2017. **8**(NA): p. 11-15.
9. Kevin M. Koch, Anja C. S. Brau, Weitian Chen, Garry E. Gold, Brian A. Hargreaves, Matthew F. Koff, Graeme C. McKinnon, Hollis G. Potter, and Kevin F. King, *Imaging near metal with a MAVRIC-SEMAC hybrid.* Magn. Reson. Med., 2010. **65**(1): p. 71-82.
10. Kevin M. Koch, Brian A. Hargreaves, K. Butts Pauly, Weitian Chen, Garry E. Gold, and Kevin F. King, *Magnetic resonance imaging near metal implants.* Journal of magnetic resonance imaging : JMRI, 2010. **32**(4): p. 773-787.
11. Catherine L. Hayter, Matthew F. Koff, and Hollis G. Potter, *Magnetic resonance imaging of the postoperative hip.* J. Magn. Reson. Imaging, 2012. **35**(5): p. 1013-1025.
12. Pia M. Jungmann, Christoph A. Agten, Christian W. Pfirrmann, and Reto Sutter, *Advances in MRI around metal.* J. Magn. Reson. Imaging, 2017. **46**(4): p. 972-991.
13. Aritrick Chatterjee, Carla Harmath, and Aytekin Oto, *New prostate MRI techniques and sequences.* Abdom. Radiol. (NY), 2020. **45**(12): p. 4052-4062.

14. Patrick W. Stroman, Howard J. M. Warren, Gabriela Ioachim, Jocelyn M. Powers, and Kaitlin McNeil, *A comparison of the effectiveness of functional MRI analysis methods for pain research: The new normal.* PLoS One, 2020. **15**(12): p. e0243723-NA.
15. Claudia Nuñez-Peralta, Jorge Alonso-Pérez, and Jordi Díaz-Manera, *The increasing role of muscle MRI to monitor changes over time in untreated and treated muscle diseases.* Curr. Opin. Neurol., 2020. **33**(5): p. 611-620.
16. International Electrotechnical Commission (IEC), *60601-2-33 Medical electrical equipment-part 2-33: particular requirements for the basic safety and essential performance of magnetic resonance equipment for medical diagnosis, Edition 3.2. 2015*. 2015.
17. Brian A Hargreaves, Pauline W Worters, Kim Butts Pauly, John M Pauly, Kevin M Koch, and Garry E Gold, *Metal-induced artifacts in MRI.* AJR Am. J. Roentgenol., 2011. **197**(3): p. 547-55.
18. Kevin M. Koch, John E. Lorbiecki, R. Scott Hinks, and Kevin F. King, *A multispectral three-dimensional acquisition technique for imaging near metal implants.* Magn. Reson. Med., 2009. **61**(2): p. 381-390.
19. Wenmiao Lu, Kim Butts Pauly, Garry E. Gold, John M. Pauly, and Brian A. Hargreaves, *SEMAC: Slice Encoding for Metal Artifact Correction in MRI.* Magn. Reson. Med., 2009. **62**(1): p. 66-76.
20. Zang-Hee Cho, D. J. Kim, and Y. K. Kim, *Total inhomogeneity correction including chemical shifts and susceptibility by view angle tilting.* Med. Phys., 1988. **15**(1): p. 7-11.
21. Brian A. Hargreaves, Weitian Chen, Wenmiao Lu, Marcus T. Alley, Garry E. Gold, Anja C. S. Brau, John M. Pauly, and Kim Butts Pauly, *Accelerated slice encoding for metal artifact correction.* JMRI, 2010. **31**(4): p. 987-996.
22. Christina A. Chen, Weitian Chen, Stuart B. Goodman, Brian A. Hargreaves, Kevin M. Koch, Wenmaio Lu, Anja C. S. Brau, Christine E. Draper, Scott L. Delp, and Garry E. Gold, *New MR imaging methods for metallic implants in the knee: artifact correction and clinical impact.* JMRI, 2011. **33**(5): p. 1121-1127.
23. Lukas Winter, Frank Seifert, Luca Zilberti, Manuel Murbach, and Bernd Ittermann, *MRI-Related Heating of Implants and Devices: A Review.* J. Magn. Reson. Imaging, 2021. **53**(6): p. 1646-1665.
24. Lukas Winter, Eva Oberacker, Celal Özerdem, Yiyi Ji, Florian von Knobelsdorff-Brenkenhoff, Gerd Weidemann, Bernd Ittermann, Frank Seifert, and Thoralf Niendorf, *On the RF heating of coronary stents at 7.0 Tesla MRI.* Magn. Reson. Med., 2015. **74**(4): p. 999-1010.
25. Jonathan Espiritu, Mostafa Berangi, Christina Yiannakou, Eduarda Silva, Roberto Francischello, Andre Kuehne, Thoralf Niendorf, Sören Könneker, Regine Willumeit-Römer, and Jan-Marten Seitz, *Evaluating metallic artefact of biodegradable magnesium-based implants in magnetic resonance imaging.* Bioact. Mater., 2022. **15**: p. 382-391.
26. Dawei Li, Jianfeng Zheng, Yan Liu, Changwang Pan, Wolfgang Kainz, Fan Yang, Wen Wu, and Ji Chen, *An efficient approach to estimate MRI RF field induced in vivo heating for small medical implants.* IEEE Trans. Electromagn. Compat., 2015. **57**(4): p. 643-650.
27. Kenneth B. Baker, Jean A. Tkach, John A. Nyenhuis, Michael Phillips, Frank G. Shellock, Jorge Gonzalez-Martinez, and Ali R. Rezai, *Evaluation of specific absorption rate as a dosimeter of MRI-related implant heating.* J. Magn. Reson. Imaging, 2004. **20**(2): p. 315-320.

28. Lukas Winter, Berk Silemek, Johannes Petzold, Harald Pfeiffer, Werner Hoffmann, Frank Seifert, and Bernd Ittermann, *Parallel transmission medical implant safety testbed: Real-time mitigation of RF induced tip heating using time-domain E-field sensors.* Magn. Reson. Med., 2020. **84**(6): p. 3468-3484.
29. Yigitcan Eryaman, Esra Abaci Turk, Cagdas Oto, Oktay Algin, and Ergin Atalar, *Reduction of the radiofrequency heating of metallic devices using a dual-drive birdcage coil.* Magn. Reson. Med., 2013. **69**(3): p. 845-852.
30. Yigitcan Eryaman, Bastien Guerin, Can Akgun, Joaquin L. Herraiz, Adrian Martin, Angel Torrado-Carvajal, Norberto Malpica, Juan A. Hernandez-Tamames, Emanuele Schiavi, Elfar Adalsteinsson, and Lawrence L. Wald, *Parallel transmit pulse design for patients with deep brain stimulation implants.* Magn. Reson. Med., 2015. **73**(5): p. 1896-1903.
31. Bastien Guerin, Leonardo M. Angelone, Darin Dougherty, and Lawrence L. Wald, *Parallel transmission to reduce absorbed power around deep brain stimulation devices in MRI: Impact of number and arrangement of transmit channels.* Magn. Reson. Med., 2020. **83**(1): p. 299-311.
32. Yigitcan Eryaman, Naoharu Kobayashi, Sean Moen, Joshua Aman, Andrea Grant, J. Thomas Vaughan, Gregory Molnar, Michael C. Park, Jerrold Vitek, Gregor Adriany, Kamil Ugurbil, and Noam Harel, *A simple geometric analysis method for measuring and mitigating RF induced currents on Deep Brain Stimulation leads by multichannel transmission/reception.* Neuroimage, 2019. **184**: p. 658-668.
33. C. E. McElcheran, L. Golestanirad, M. I. Iacono, P. S. Wei, B. Yang, K. J. T. Anderson, G. Bonmassar, and S. J. Graham, *Numerical Simulations of Realistic Lead Trajectories and an Experimental Verification Support the Efficacy of Parallel Radiofrequency Transmission to Reduce Heating of Deep Brain Stimulation Implants during MRI.* Sci. Rep., 2019. **9**(1).
34. Yigitcan Eryaman, Burak Akin, and Ergin Atalar, *Reduction of implant RF heating through modification of transmit coil electric field.* Magn. Reson. Med., 2011. **65**(5): p. 1305-1313.
35. Theresa Bachschmidt, Michael Köhler, Jürgen Nistler, Christian Geppert, Peter M. Jakob, and Mathias Nittka, *Polarized multichannel transmit MRI to reduce shading near metal implants.* Magn. Reson. Med., 2015. **75**(1): p. 217-226.
36. Jasmine Vu, Bach T. Nguyen, Bhumi Bhusal, Justin J. Baraboo, Joshua M. Rosenow, Ulas Bagci, Molly G. Bright, and Laleh Golestanirad, *Machine Learning-Based Prediction of MRI-Induced Power Absorption in the Tissue in Patients With Simplified Deep Brain Stimulation Lead Models.* IEEE Trans. Electromagn. Compat., 2021. **63**(5): p. 1757-1766.
37. Peter R. S. Stijnman, Bart R. Steensma, Cornelis A. T. van den Berg, and Alexander J. E. Raaijmakers, *A perturbation approach for ultrafast calculation of RF field enhancements near medical implants in MRI.* Sci. Rep., 2022. **12**(1).
38. Yeoheung Yun, Zhongyun Dong, Namheon Lee, Yijun Liu, Dingchuan Xue, Xuefei Guo, Julia Kuhlmann, Amos Doepke, H. Brian Halsall, and William Heineman, *Revolutionizing biodegradable metals.* Mater. Today, 2009. **12**(10): p. 22-32.
39. Jan-Marten Seitz, Arne Lucas, and Martin Kirschner, *Magnesium-Based Compression Screws: A Novelty in the Clinical Use of Implants.* JOM, 2016. **68**(4): p. 1177-1182.
40. Jonathan Espiritu, Mostafa Berangi, Hanna Cwieka, Kamila Iskhakova, Andre Kuehne, D. C. Florian Wieland, Berit Zeller-Plumhoff, Thoralf Niendorf, Regine

Willumeit-Römer, and Jan-Marten Seitz, *Radiofrequency induced heating of biodegradable orthopaedic screw implants during magnetic resonance imaging.* Bioactive materials, 2023. **25**(NA): p. 86-94.

41. Jonathan Espiritu, Mostafa Berangi, Christina Yiannakou, Eduarda Silva, Roberto Francischello, Andre Kuehne, Thoralf Niendorf, Sören Könneker, Regine Willumeit-Römer, and Jan Marten Seitz, *Evaluating metallic artefact of biodegradable magnesium-based implants in magnetic resonance imaging.* Bioact. Mater., 2022. **15**: p. 382-391.
42. *Guide for in vitro Degradation Testing of Absorbable Metals.* 2018.
43. *Test Method for Evaluation of MR Image Artifacts from Passive Implants.* 2008.
44. *Test Method for Measurement of Radio Frequency Induced Heating On or Near Passive Implants During Magnetic Resonance Imaging.* 2008.
45. Wolfgang R. Nitz, Arnulf Oppelt, Wolfgang Renz, C. Manke, Markus Lenhart, and Johann Link, *On the heating of linear conductive structures as guide wires and catheters in interventional MRI.* JMRI, 2001. **13**(1): p. 105-114.
46. Peter Nordbeck, Florian Fidler, Ingo Weiss, Marcus Warmuth, Michael Friedrich, Philipp Ehses, Wolfgang Dr Geistert, Oliver Ritter, Peter M. Jakob, Mark E. Ladd, Harald H. Quick, and Wolfgang R. Bauer, *Spatial distribution of RF-induced E-fields and implant heating in MRI.* Magn. Reson. Med., 2008. **60**(2): p. 312-319.
47. Jonathan Espiritu, Mostafa Berangi, Hanna Cwieka, Kamila Iskhakova, Andre Kuehne, D. C. Florian Wieland, Berit Zeller-Plumhoff, Thoralf Niendorf, Regine Willumeit-Römer, and Jan-Marten Seitz, *Radiofrequency induced heating of biodegradable orthopaedic screw implants during magnetic resonance imaging.* Bioact. Mater., 2023. **25**: p. 86-94.
48. M. Arcan Ertürk, Alexander J.E. Raaijmakers, Gregor Adriany, Kâmil Uğurbil, and Gregory J. Metzger, *A 16-channel combined loop-dipole transceiver array for 7 Tesla body MRI.* Magn. Reson. Med., 2017. **77**(2): p. 884-894.
49. Riccardo Lattanzi, Graham C. Wiggins, Bei Zhang, Qi Duan, Ryan Brown, and Daniel K. Sodickson, *Approaching ultimate intrinsic signal-to-noise ratio with loop and dipole antennas.* Magn. Reson. Med., 2018. **79**(3): p. 1789-1803.
50. M. Clemens and T. Weiland, *Discrete electromagnetism with the finite integration technique.* PIER, 2001.
51. Roberta Kriegl, Jean-Christophe Ginefri, Marie Poirier-Quinot, Luc Darrasse, Sigrun Goluch, Andre Kuehne, Ewald Moser, and Elmar Laistler, *Novel inductive decoupling technique for flexible transceiver arrays of monolithic transmission line resonators.* Magn. Reson. Med., 2014. **73**(4): p. 1669-1681.
52. Mostafa Berangi, Andre Kuehne, Helmar Waiczies, and Thoralf Niendorf, *MRI of Implantation Sites Using Parallel Transmission of an Optimized Radiofrequency Excitation Vector.* Tomography, 2023. **9**(2): p. 603-620.
53. Kalyanmoy Deb, *Multi-objective Optimisation Using Evolutionary Algorithms: An Introduction*, in *Multi-objective Evolutionary Optimisation for Product Design and Manufacturing*, L. Wang, A.H.C. Ng, and K. Deb, Editors. 2011, Springer London: London. p. 3-34.
54. Gabriele Eichfelder and Matthias Gebhardt, *Local specific absorption rate control for parallel transmission by virtual observation points.* Magn. Reson. Med., 2011. **66**(5): p. 1468-1476.
55. Vijayanand Alagappan, Juergen Nistler, Elfar Adalsteinsson, Kawin Setsompop, Ulrich Fontius, Adam Zelinski, Markus Vester, Graham C. Wiggins, Franz Hebrank, Wolfgang Renz, Franz Schmitt, and Lawrence L. Wald, *Degenerate*

mode band-pass birdcage coil for accelerated parallel excitation. Magn. Reson. Med., 2007.

56. Qi Duan, Jeff H. Duyn, Natalia Gudino, Jacco A. de Zwart, Peter van Gelderen, Daniel K. Sodickson, and Ryan Brown, *Characterization of a dielectric phantom for high-field magnetic resonance imaging applications.* Med. Phys., 2014. **41**(10): p. 102303-102303.
57. Carlotta Ianniello, Jacco A. de Zwart, Qi Duan, Cem M. Deniz, Leeor Alon, Jae-Seung Lee, Riccardo Lattanzi, and Ryan Brown, *Synthesized tissue-equivalent dielectric phantoms using salt and polyvinylpyrrolidone solutions.* Magn. Reson. Med., 2017. **80**(1): p. 413-419.
58. C. Gabriel, *Compilation of the dielectric properties of body tissues at RF and microwave frequencies*. 1996: King's College London.
59. Davide Santoro, Lukas Winter, Alexander Müller, Julia Vogt, Wolfgang Renz, Celal Özerdem, Andreas Grässl, Valeriy Tkachenko, Jeanette Schulz-Menger, and Thoralf Niendorf, *Detailing radio frequency heating induced by coronary stents: a 7.0 Tesla magnetic resonance study.* PLoS One, 2012. **7**(11): p. e49963-e49963.
60. Miloslav Capek, Jan Eichler, and Pavel Hazdra, *Evaluating radiation efficiency from characteristic currents.* IET Microw. Antennas Propag., 2015. **9**(1): p. 10-15.
61. Lukas Winter, Eva Oberacker, Katharina Paul, Yiyi Ji, Celal Oezerdem, Pirus Ghadjar, Alexander Thieme, Volker Budach, Peter Wust, and Thoralf Niendorf, *Magnetic resonance thermometry: Methodology, pitfalls and practical solutions.* Int. J. Hyperthermia, 2016. **32**(1): p. 63-75.
62. Sohae Chung, Daniel Kim, Elodie Breton, and Leon Axel, *Rapid B1+ mapping using a preconditioning RF pulse with TurboFLASH readout.* Magn. Reson. Med., 2010. **64**(2): p. 439-446.
63. E. K. Insko and L. Bolinger, *Mapping of the Radiofrequency Field.* Journal of Magnetic Resonance, Series A, 1993. **103**(1): p. 82-85.
64. Marie-Christine Gosselin, Esra Neufeld, Heidi Moser, Eveline Huber, Silvia Farcito, Livia Gerber, Maria Jedensjö, Isabel Hilber, Fabienne Di Gennaro, Bryn A. Lloyd, Emilio Cherubini, Dominik Szczerba, Wolfgang Kainz, and Niels Kuster, *Development of a new generation of high-resolution anatomical models for medical device evaluation: the Virtual Population 3.0.* Phys. Med. Biol., 2014. **59**(18): p. 5287-5303.
65. Regine Willumeit-Römer, *The Interface Between Degradable Mg and Tissue.* JOM, 2019. **71**(4): p. 1447-1455.
66. Jan-Marten Seitz, Rainer Eifler, Bach, and Hans Jürgen Maier, *Magnesium degradation products: Effects on tissue and human metabolism.* J. Biomed. Mater. Res. A, 2013. **102**(10): p. 3744-3753.
67. Ralf Rettig and Sannakaisa Virtanen, *Composition of corrosion layers on a magnesium rare-earth alloy in simulated body fluids.* J. Biomed. Mater. Res. A, 2009. **88**(2): p. 359-369.
68. Eva Oberacker, Katharina Paul, Till Huelnhagen, Celal Oezerdem, Lukas Winter, Andreas Pohlmann, Laura Boehmert, Oliver Stachs, Jens Heufelder, Andreas Weber, Matus Rehak, Ira Seibel, and Thoralf Niendorf, *Magnetic resonance safety and compatibility of tantalum markers used in proton beam therapy for intraocular tumors: A 7.0 Tesla study.* Magn. Reson. Med., 2016. **78**(4): p. 1533-1546.

69. Lukas Winter, Frank Seifert, Luca Zilberti, Manuel Murbach, and Bernd Ittermann, *MRI-Related Heating of Implants and Devices: A Review.* J. Magn. Reson. Imaging, 2021. **53**(6): p. 1646-1665.
70. MatWeb. *MatWeb: Material Property Data*. 1996-2022 [cited 2022 14 July]; Available from: https://www.matweb.com/index.aspx.
71. L. Poulo, L. Alon, C. Deniz, R. Haefner, D. Sodickson, B. Stoeckel, and Y. A. Zhu, *32-channel parallel exciter/amplifier transmit system for 7T imaging*, in *Proc. Int. Soc. Magn. Reson. Med*. 2011. p. 1867-1867.
72. Haopeng Han, Eva Oberacker, Andre Kuehne, Shuailin Wang, Thomas Wilhelm Eigentler, Eckhard Grass, and Thoralf Niendorf, *Multi-Channel RF Supervision Module for Thermal Magnetic Resonance Based Cancer Therapy.* Cancers (Basel), 2021. **13**(5).
73. Thomas Fiedler, Stephan Orzada, Martina Flöser, Stefan H. G. Rietsch, Harald H. Quick, Mark E. Ladd, and Andreas K. Bitz, *Performance analysis of integrated RF microstrip transmit antenna arrays with high channel count for body imaging at 7 T.* NMR Biomed., 2021. **34**(7): p. e4515-NA.
74. Sinduja Seshadri and Jonathan B Scott. *Enhancing skin-effect using surface roughening and its potential to reduce RF heating from implant leads*. in *ENZCon 2017, Electronics New Zealand Conference 2017*. 2017.
75. Alexander J.E. Raaijmakers, Michel Italiaander, Ingmar J. Voogt, Peter R. Luijten, Johannes M. Hoogduin, Dennis W.J. Klomp, and Cornelis A.T. van den Berg, *The fractionated dipole antenna: A new antenna for body imaging at 7 Tesla.* Magn. Reson. Med., 2016. **75**(3): p. 1366-1374.

Statutory Declaration

“I, Mostafa, Berangi, by personally signing this document in lieu of an oath, hereby affirm that I prepared the submitted dissertation on the topic Development of Parallel Radiofrequency Transmission Approaches for Magnetic Resonance Imaging of Conductive Bio-degradable Implants/Entwicklung paralleler Hochfrequenztechnologie für die Magnetresonanztomographie elektrisch leitfähiger, biologisch abbaubarer Implantate, independently and without the support of third parties, and that I used no other sources and aids than those stated.
All parts which are based on the publications or presentations of other authors, either in letter or in spirit, are specified as such in accordance with the citing guidelines. The sections on methodology (in particular regarding practical work, laboratory regulations, statistical processing) and results (in particular regarding figures, charts and tables) are exclusively my responsibility.

Furthermore, I declare that I have correctly marked all of the data, the analyses, and the conclusions generated from data obtained in collaboration with other persons, and that I have correctly marked my own contribution and the contributions of other persons (cf. declaration of contribution). I have correctly marked all texts or parts of texts that were generated in collaboration with other persons.

My contributions to any publications to this dissertation correspond to those stated in the below joint declaration made together with the supervisor. All publications created within the scope of the dissertation comply with the guidelines of the ICMJE (International Committee of Medical Journal Editors; http://www.icmje.org) on authorship. In addition, I declare that I shall comply with the regulations of Charité – Universitätsmedizin Berlin on ensuring good scientific practice.

I declare that I have not yet submitted this dissertation in identical or similar form to another Faculty.

The significance of this statutory declaration and the consequences of a false statutory declaration under criminal law (Sections 156, 161 of the German Criminal Code) are known to me.”

Date Signature

Declaration of your own contribution to the publications

Mostafa Berangi contributed the following to the below listed publications:

Peer-reviewed journal publications:

Publication 1: Jonathan Espiritu, **Mostafa Berangi**, Christina Yiannakou, Eduarda Silva, Roberto Francischello, Andre Kühne, Thoralf Niendorf, Sören Könneker, Regine Willumeit-Römer i, Jan-Marten Seitz, Evaluating metallic artefact of biodegradable magnesium-based implants in magnetic resonance imaging Bioactive Materials, 2022

Contribution: Data curation, Formal analysis, Investigation, Methodology, Writing—review and editing.

-Investigation and simulation of the physical phenomena leading to implant-induced artefact,

-Design, simulation, and manufacturing of the parallel transceiver array antenna tailored for 7.0 T MRI measurements

-preparation of the phantom for 3.0 T & 7.0 T MRI data acquisition

-Data acquisition using 3.0 T & 7.0 T MRI scanners,

-Review and editing of the manuscript.

Publication 2: Jonathan Espiritu, **Mostafa Berangi**, Hanna Cwieka, Kamila Iskhakova, Andre Kuehne, D.C. Florian Wieland, Berit Zeller-Plumhoff, Thoralf Niendorf, Regine Willumeit-Römer, Jan-Marten Seitz, Radiofrequency induced heating of biodegradable orthopaedic screw implants during magnetic resonance imaging, Bioactive Materials, 2023

Contribution: Data curation, Formal analysis, Investigation, Methodology, Writing—review and editing.

-Investigation and simulation of the physical phenomena leading to implant-induced heating,

-preparation of the phantom for 3.0 T MRI data acquisition

-MRI Data acquisition using 3.0 T MRI scanner,

-Temperature measurement using fiber optic thermometer in 3.0 T MRI scans,

-Review and editing the manuscript.

Publication 3: **Mostafa Berangi**, Andre Kuehne, Helmar Waiczies and Thoralf Niendorf, MRI of Implantation Sites Using Parallel Transmission of an Optimized Radiofrequency Excitation Vector, Tomography, 2023

Contribution: Methodology, Software, Validation, Formal analysis, Investigation, Data curation, Writing—original draft, Writing—review and editing, Visualization.

-Investigation and simulation of the physical phenomena leading to implant-induced heating and B_1^+ non-uniformity,

-Design, development and manufacturing of the liquid and gel-based phantom for B_1^+ artefact measurement tailored for 7.0 T MRI scanner,

-Design, simulation and manufacturing of the parallel transceiver array antenna tailored for 7.0 T MRI measurements,

-Implementation of radio frequency B_1^+ shimming approach in MATLAB using a multi-objective genetic algorithm,

-MRI Data acquisition using parallel radiofrequency transmission of the 7.0 T MRI scanner,

-Temperature increment measurement using MR thermometry,

-Data analysis and radiofrequency B_1^+ calibration,

-Writing the draft and editing the manuscript.

Signature, date and stamp of first supervising university professor / lecturer

Signature of doctoral candidate

Excerpt from Journal Summary List

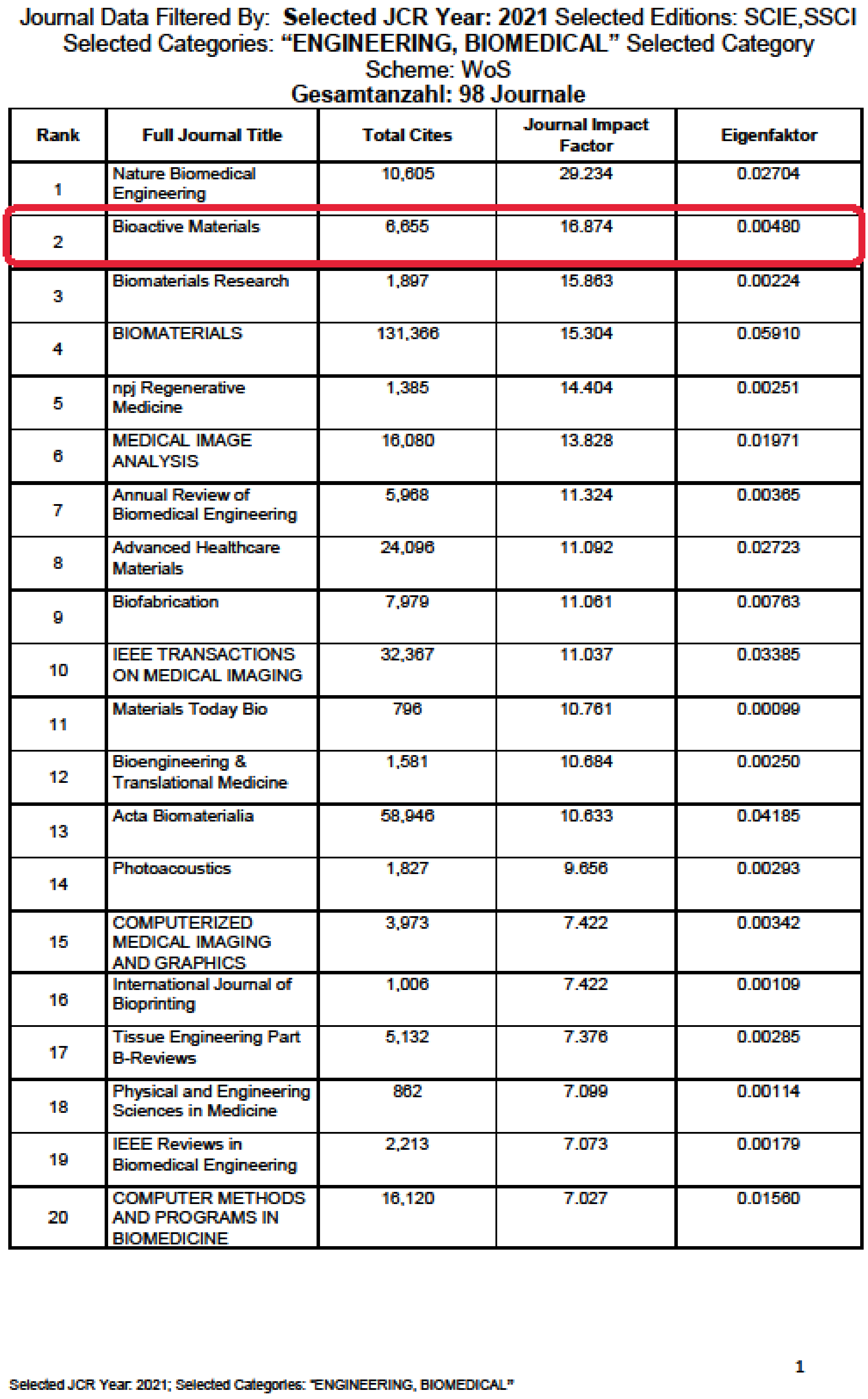

Journal Data Filtered By: **Selected JCR Year: 2021** Selected Editions: SCIE,SSCI Selected Categories: **"ENGINEERING, BIOMEDICAL"** Selected Category Scheme: WoS
Gesamtanzahl: 98 Journale

Rank	Full Journal Title	Total Cites	Journal Impact Factor	Eigenfaktor
1	Nature Biomedical Engineering	10,605	29.234	0.02704
2	Bioactive Materials	6,655	16.874	0.00480
3	Biomaterials Research	1,897	15.863	0.00224
4	BIOMATERIALS	131,366	15.304	0.05910
5	npj Regenerative Medicine	1,385	14.404	0.00251
6	MEDICAL IMAGE ANALYSIS	16,080	13.828	0.01971
7	Annual Review of Biomedical Engineering	5,968	11.324	0.00365
8	Advanced Healthcare Materials	24,096	11.092	0.02723
9	Biofabrication	7,979	11.061	0.00763
10	IEEE TRANSACTIONS ON MEDICAL IMAGING	32,367	11.037	0.03385
11	Materials Today Bio	796	10.761	0.00099
12	Bioengineering & Translational Medicine	1,581	10.684	0.00250
13	Acta Biomaterialia	58,946	10.633	0.04185
14	Photoacoustics	1,827	9.656	0.00293
15	COMPUTERIZED MEDICAL IMAGING AND GRAPHICS	3,973	7.422	0.00342
16	International Journal of Bioprinting	1,006	7.422	0.00109
17	Tissue Engineering Part B-Reviews	5,132	7.376	0.00285
18	Physical and Engineering Sciences in Medicine	862	7.099	0.00114
19	IEEE Reviews in Biomedical Engineering	2,213	7.073	0.00179
20	COMPUTER METHODS AND PROGRAMS IN BIOMEDICINE	16,120	7.027	0.01560

1

Selected JCR Year: 2021; Selected Categories: "ENGINEERING, BIOMEDICAL"

Publication 1

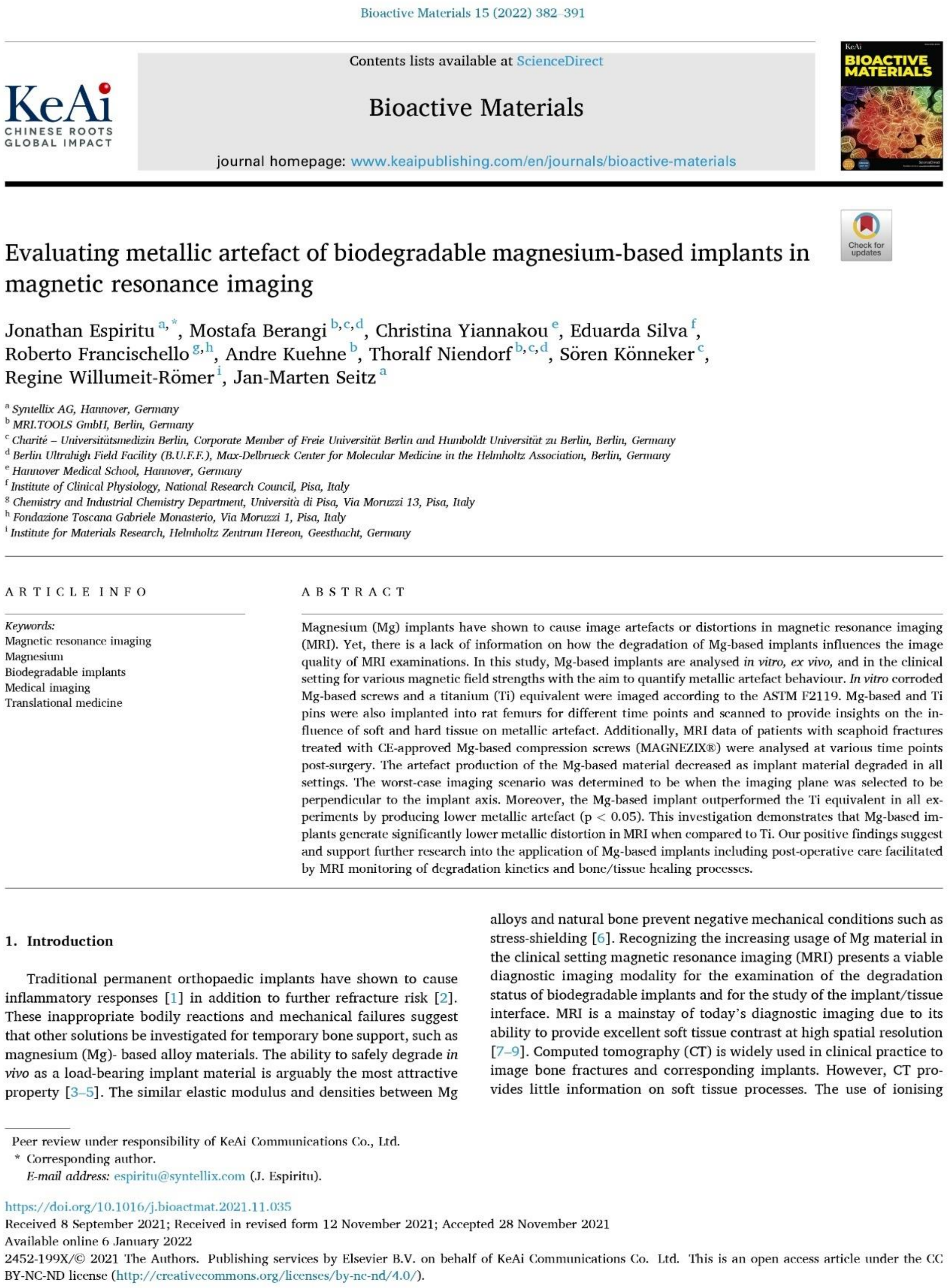

Bioactive Materials 15 (2022) 382–391

KeAi
CHINESE ROOTS
GLOBAL IMPACT

Contents lists available at ScienceDirect

Bioactive Materials

journal homepage: www.keaipublishing.com/en/journals/bioactive-materials

Evaluating metallic artefact of biodegradable magnesium-based implants in magnetic resonance imaging

Jonathan Espiritu [a,*], Mostafa Berangi [b,c,d], Christina Yiannakou [e], Eduarda Silva [f], Roberto Francischello [g,h], Andre Kuehne [b], Thoralf Niendorf [b,c,d], Sören Könneker [c], Regine Willumeit-Römer [i], Jan-Marten Seitz [a]

[a] *Syntellix AG, Hannover, Germany*
[b] *MRI.TOOLS GmbH, Berlin, Germany*
[c] *Charité – Universitätsmedizin Berlin, Corporate Member of Freie Universität Berlin and Humboldt Universität zu Berlin, Berlin, Germany*
[d] *Berlin Ultrahigh Field Facility (B.U.F.F.), Max-Delbrueck Center for Molecular Medicine in the Helmholtz Association, Berlin, Germany*
[e] *Hannover Medical School, Hannover, Germany*
[f] *Institute of Clinical Physiology, National Research Council, Pisa, Italy*
[g] *Chemistry and Industrial Chemistry Department, Università di Pisa, Via Moruzzi 13, Pisa, Italy*
[h] *Fondazione Toscana Gabriele Monasterio, Via Moruzzi 1, Pisa, Italy*
[i] *Institute for Materials Research, Helmholtz Zentrum Hereon, Geesthacht, Germany*

ARTICLE INFO

Keywords:
Magnetic resonance imaging
Magnesium
Biodegradable implants
Medical imaging
Translational medicine

ABSTRACT

Magnesium (Mg) implants have shown to cause image artefacts or distortions in magnetic resonance imaging (MRI). Yet, there is a lack of information on how the degradation of Mg-based implants influences the image quality of MRI examinations. In this study, Mg-based implants are analysed *in vitro, ex vivo,* and in the clinical setting for various magnetic field strengths with the aim to quantify metallic artefact behaviour. *In vitro* corroded Mg-based screws and a titanium (Ti) equivalent were imaged according to the ASTM F2119. Mg-based and Ti pins were also implanted into rat femurs for different time points and scanned to provide insights on the influence of soft and hard tissue on metallic artefact. Additionally, MRI data of patients with scaphoid fractures treated with CE-approved Mg-based compression screws (MAGNEZIX®) were analysed at various time points post-surgery. The artefact production of the Mg-based material decreased as implant material degraded in all settings. The worst-case imaging scenario was determined to be when the imaging plane was selected to be perpendicular to the implant axis. Moreover, the Mg-based implant outperformed the Ti equivalent in all experiments by producing lower metallic artefact ($p < 0.05$). This investigation demonstrates that Mg-based implants generate significantly lower metallic distortion in MRI when compared to Ti. Our positive findings suggest and support further research into the application of Mg-based implants including post-operative care facilitated by MRI monitoring of degradation kinetics and bone/tissue healing processes.

1. Introduction

Traditional permanent orthopaedic implants have shown to cause inflammatory responses [1] in addition to further refracture risk [2]. These inappropriate bodily reactions and mechanical failures suggest that other solutions be investigated for temporary bone support, such as magnesium (Mg)- based alloy materials. The ability to safely degrade *in vivo* as a load-bearing implant material is arguably the most attractive property [3–5]. The similar elastic modulus and densities between Mg alloys and natural bone prevent negative mechanical conditions such as stress-shielding [6]. Recognizing the increasing usage of Mg material in the clinical setting magnetic resonance imaging (MRI) presents a viable diagnostic imaging modality for the examination of the degradation status of biodegradable implants and for the study of the implant/tissue interface. MRI is a mainstay of today's diagnostic imaging due to its ability to provide excellent soft tissue contrast at high spatial resolution [7–9]. Computed tomography (CT) is widely used in clinical practice to image bone fractures and corresponding implants. However, CT provides little information on soft tissue processes. The use of ionising

---

Peer review under responsibility of KeAi Communications Co., Ltd.

* Corresponding author.
E-mail address: espiritu@syntellix.com (J. Espiritu).

https://doi.org/10.1016/j.bioactmat.2021.11.035
Received 8 September 2021; Received in revised form 12 November 2021; Accepted 28 November 2021

Abbreviations

AP	Anterior/Posterior
ASTM	American Society of Testing and Materials
B 0	Main Magnetic Field
DICOM	Digital Imaging and Communications in Medicine
FOV	Field of View
GRE	Gradient Echo
HF	Head/Foot
LR	Left/Right
Mg MRI	Magnetic Resonance Imaging
ORTH	Orthogonal
PAR	Parallel
RF	Radio Frequency
SAG	Sagittal
TAV	Total Artefact Volume
TE	Echo Time
Ti	Titanium
tp	Time Point
TR	Repetition Time
TRA	Transverse
TSE	Turbo Spin Echo
w	Weighted

radiation in serial CT examinations adds to the cumulative radiation dose of patients which may be associated with a small but significantly increased risk of malignancy [10]. Since MRI does not administer any type of ionising radiation, long-term harmful effects are considered insignificant [11]. However, diagnostic imaging quality can be compromised by image artefacts attributed to the patient (motion and flow artefacts), signal processing (wrap around and chemical shifts), or to the hardware (static magnetic field or radiofrequency (RF) transmission field inhomogeneities).

In MRI metallic implants may cause image distortion artefacts, or susceptibility artefacts. Metals have intrinsic magnetic susceptibilities that produce significant local field disturbances. These local changes in the resonance frequency shift image pixels away from their true positions leading to significant geometric distortions including signal reduction or voids (black areas in the image) and signal enhancements (bright areas in the image). These distortions are created by perturbations of the static magnetic field and are related to the specific material properties of the implant. Although there have been many methods demonstrating a reduction in artefacts [12], complete metallic artefacts cannot be removed.

Metallic implants made of materials, like Mg, have shown to cause image artefacts due to the inherent magnetic susceptibility of the material. However, their impact on MRI quality is less compared to other current permanent metallic implants [13].

The evaluation of artefact production in MRI is necessary when choosing a biomaterial. Artefact limitation is vital since compromised or poor image quality may disturb medical diagnosis or anatomical visualisation. The aim of this investigation is to quantify the metallic artefact production of Mg-based implants during the degradation process in various MRI settings with the ultimate goal to support the use of Mg-based implants in the clinical setting due to successful visualisation in MRI. To benchmark the MRI performance of Mg-based implants standard, commercial Ti based implants are used as a reference.

2. Materials and methods

2.1. *In vitro investigation*

Orthopaedic compression screws 40 mm in length and diameter of 3.2 mm made of WE43-based material manufactured by Syntellix AG (Hannover, Germany) underwent *in vitro* degradation. The volume of the WE43 screw is 151.51 mm^3 with a surface area of 552.54 mm^2. Chemical composition of WE43 includes Yttrium (3.7–4.3%), Rare Earth Elements (2.4–4.4%), Zirconium (0.4%), with the remainder composing of Mg [14]. A non-degraded WE43 screw and a titanium equivalent of similar geometry were included for comparative results (Fig. 1).

The WE43 samples were degraded via a modified ASTM F3268 Standard [15] with Dulbecco's Phosphate Buffered Saline (DPBS). A total of five screws were degraded in the DPBS with different immersion times varying by one week with a total of five time points (1 week, 2 weeks, 3 weeks, 4 weeks, and 5 weeks). After immersion time was completed, the samples were cleaned with distilled water to remove any excess salts and rinsed with ethanol to prevent further oxidation before drying and storage.

Fig. 1. 40 mm Mg-based orthopaedic compression screw MAGNEZIX® CS ø3.2 (top) and Ti market-equivalent (bottom).

For the in vitro MRI measurements, a 1.5 T (GE Signa Artist, GE Healthcare, Waukesha, USA), 3.0 T (Skyra Fit, Siemens, Erlangen, Germany) and 7.0 T (Magnetom, Siemens, Erlangen, Germany) MRI Scanner were used. Further details on the imaging protocol and imaging techniques employed for the *in vitro* measurements are documented in Table 1.

The following *in vitro* procedure has been adapted from ASTM F2119 [16] and consists of two parts: (1) the acquisition of images with the test object's long axis perpendicular to the main magnetic field (B_0), and (2) the acquisition of images with the test object's long axis parallel to the main magnetic field. Implant orientation relative to the main magnetic field, imaging sequence applied, slice orientation, phase-encoding direction, and material were varied for each combination before each image acquisition. The test object was suspended in a home built phantom acrylic container via a 3D printed holder filled with $CuSO_4$ solution (Merck Millipore, USA) to reduce T_1 relaxation effects. Artefact dimensions were determined by applying the ASTM F2119 definition for artefacts via a custom MATLAB (The MathWorks Inc., USA) script. Examples of measurements completed by the script are shown in Fig. 2. The diameter artefact is measured by determining the longest artefact along the diameter of the screw. The length artefact is determined by measuring the longest artefact along the length of the screw. The largest

Table 1
Parameters of sequences used for *in vitro* MRI investigations.

B_0 Field Strength [T]	1.5		3.0		7.0	
RF Coil Type	Spinal		Spinal		Basic Volume	
Sequence	GRE	TSE	GRE	TSE	GRE	TSE
TR [ms]	100	500	500	1190	550	1190
TE [ms]	15	20	13	20	13	30
FOV [mm]	300	300	180	200	185	185
Matrix Size [pixel]	256	256	256	256	256	256
Slice Thickness [mm]	2	2	2	2	2	2

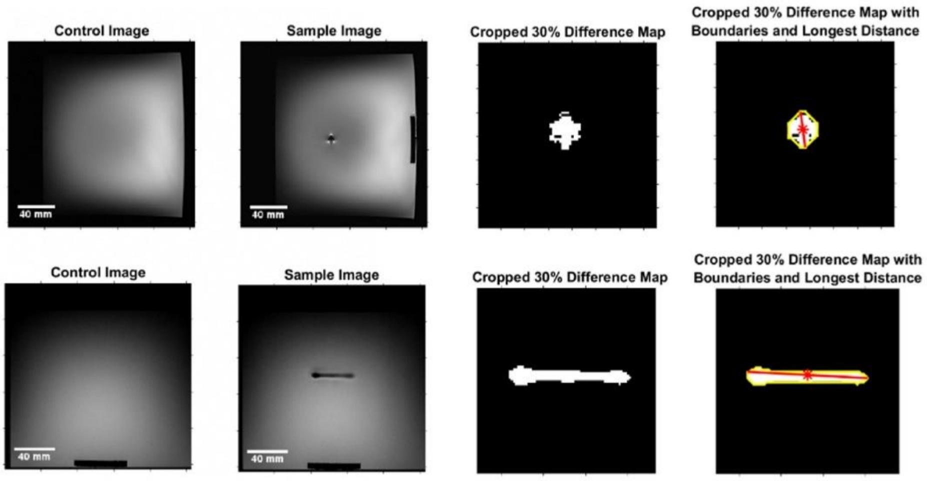

Fig. 2. Script workflow of diameter (to p) and length (bottom) artefact measurement of image data acquired at 3 T MRI. A control and a sample image are loaded and compared to detect a 30% intensity change. This change is used to create a binary image where a longest distance can then be measured (red indicator line).

measurements are taken as the 'worst-case' artefact.

Calculation of test object distortion was performed to determine the artefact size in relation to the test object dimension. Test object distortion is calculated by:

$$\frac{\text{Total artefact length measured} - \text{test object dimension}}{\text{Test object dimension}}$$

2.2. Ex vivo investigation

2.2.1. Experimental animals

All *in vivo* experiments were carried out in accordance with the National Ethical Guidelines (Italian Ministry of Health; D.L.vo 26/2014) and the guidelines from Directive 2010/63/EU of the European Parliament. The protocol was approved by the Instituto Superiore di Sanità on behalf of Italian Ministry of Health and Ethical Panel (Prot. n° 299/2020-PR) and the local ethics committee. Additionally, the protocol conformed to the ARRIVE guidelines [17].

A total of three 12-week-old female Wistar rats were used in this experiment. On surgery, animals were anesthetized with an intraperitoneal injection of 5 mg/kg Xylazine (Rompum Elanco, Italy) and 10 mg/kg Zoletil (Virbac, Switzerland). The depth of anaesthesia was controlled by toe pinch response.

2.2.2. Surgical approach

Through a lateral approach, an incision was made on the skin and the muscles are carefully teased away to expose the mid-diaphyseal region of the femur. A drill with 1.55 mm diameter is used to prepare the transcortical implantation bed with the longitudinal axis of this drill perpendicular to the longitudinal axis of the femoral diaphysis. Drilling is performed at low rotational speed and profuse physiological saline (Fresenius Kabi, Italy) irrigation is applied via syringe to minimise frictional heat and thermal necrosis. A pin implant of 8 mm in length and 1.5 mm in diameter made of WE43 or Ti was implanted in this procedure. The cylindrical implant is inserted by gentle tapping, resulting in a uniform press fit. After transcortical placement is ensured, the operating field is cleaned with sterile cotton tips for remaining bone debris and the wound is closed with resorbable sutures (Johnson & Johnson Medical, Italy). Thereafter, the contralateral side is operated in the same way and using the same implant type.

The sacrifice of the animals at various time-points is performed with a lethal dose of isoflurane (IsoFlo, Zoetis, Italy); hind paws are explanted cutting through the hip joint and stored at −20 °C until further analysis.

2.2.3. Explant imaging

The explants were scanned to obtain information on the influence of hard and soft tissue on the artefact production, moving closer to mimicking the true physiological environment. *Ex vivo* MRI measurements of the hind paws were performed at Consiglio Nationale delle Ricerche Area della Ricerca di Pisa (Pisa, Italy) using a 7 T small animal MRI scanner (Bruker Avance III HD 300). Further details and sequences employed for measurements are documented in Table 2.

DICOM images were loaded and analysed with MATLAB. The artefact area of each scan was measured within each sequence set for one explant containing a WE43-based pin one day after surgery, one explant containing a WE43-based pin thirty days after surgery, and one explant containing a Ti-based equivalent. A single time-point was selected for Ti since the material is not expected to degrade, unlike the WE43 material. A total of 18 tracings were completed (six tracings per sample). To calculate the total artefact volume (TAV) for each scan, the artefact areas measured for each slice were summed and multiplied by the slice thickness as described by the Debatin method [18].

2.3. Clinical investigation

2.3.1. Clinical trial

Imaging data in humans was provided by the randomised controlled clinical trial SCAMAG (Comparison of scaphoid fracture osteosynthesis

Table 2
MRI sequences applied during explant imaging at 7 T.

B_0 Field Strength [T]	7.0
RF Coil	Quadrature Bird Cage
Sequence	T1 RARE
TR [ms]	1500
TE [ms]	7
Spatial resolution [mm]	0.12
FOV [mm]	30
Matrix Scan [pixel]	256
Slice Thickness [mm]	0.8

by magnesium-based headless Herbert screws with titanium Herbert screws) [19]. The trial is a blinded observer controlled parallel two-group post-market trial with a follow-up of one year per patient. Each involved patient is treated with either a Ti or Mg-based compression screw. The primary aim of SCAMAG is to demonstrate Mg-based compression screws as non-inferior when compared to Ti in the treatment of scaphoid fractures. The study protocol adheres to the SPIRIT [20] and CONSORT [21] statements. The SCAMAG trial was approved by the ethics committee of the Hanover Medical School (MHH) on September 27, 2017 (registration number: 7614) including registration with the German Register for Clinical Trials (DRKS, drks.de) on December 4, 2017 (registration number: DRKS00013368).

2.3.2. *Patient imaging*

Randomly chosen patients involved in the study treated with Mg-based compression screw (MAGNEZIX® CS, Syntellix AG, Hannover, Germany) participated in MRI examinations. The scans were performed on a 3 T MR scanner (Vario, Siemens, Erlangen, Germany) at the Medical School Hannover (Hannover, Germany). Typical wrist imaging MRI protocols were performed for this study, which are summarised in Table 3.

DICOM images were loaded and analysed with MATLAB R2019b (The MathWorks Inc., US). A total of four patient follow-up scans were included in this analysis. The first, second, third, and fourth patients were treated with a single compression screw of sizes Ø 2.7 mm with length 26 mm, Ø 3.2 mm with length 26 mm, Ø 3.2 mm with length 20 mm, Ø 3.2 mm with length 24 mm, respectively. The artefact area of each scan was measured within each sequence set for the available time points: 1.5-, 3-, 6-, and 12-months post operation. A total of 64 tracings were completed. The TAV was calculated similarly as in Section 2.2.

2.4. *Statistics*

Statistical analyses were performed using RStudio (RStudio, USA). A p-value of <0.05 was chosen to be statistically significant.

To compare the artefacts produced by Ti, Mg, and various time-corroded Mg samples in the *in vitro* measurements with respect to implant orientation, sequence type, slice orientation, and encoding direction, an analysis of variance (ANOVA) was completed. If a significant p-value was determined, pairwise comparisons were performed using a Tukey's post hoc multiple comparison procedure.

For *ex vivo* investigations, the ANOVA test was applied to determine differences between material implanted into the rat femur. The ANOVA test was also applied in the clinical cases to determine the significant effects of slice orientation and healing time on the TAV.

Table 3

MRI scanning protocols from SCAMAG clinical trial. Scanning sequences used include proton density-weighted turbo spin echo with fat saturation (PDw TSE with FS) and T1/T2-weighted turbo spin echo (T1/T2w TSE).

Field Strength [T]	3.0			
Sequence	PDw TSE with fat saturation	T1w TSE	T2w TSE	T2w TSE
Slice Plane	Axial	Coronal 1	Coronal 2	Sagittal
TR [ms]	3220–4290	485–586	3090–3160	2430–2920
TE [ms]	37	32	39	97
Spatial resolution [mm]	0.22	0.20	0.25	0.25
FOV [mm]	100 × 80	100 × 80	100 × 80	100 × 80
Slice Thickness [mm]	2	2	2	2

3. Results

3.1. *In vitro results*

3.1.1. *Titanium vs magnesium*

By varying different MRI scanning parameters (seen in Fig. 3) the significant differences were found for the Ti and Mg samples. For all main field magnetic strengths, the Mg-samples produced significantly less artefacts than the Ti counterparts. Turbo spin echo sequences produced lower artefacts versus gradient echo sequence. The averaged diameter- and length-measured artefacts are summarised in Table 4. Averaged distortions or artefact measured based on material and magnetic field strength are documented in Fig. 4. An increase in magnetic field strength results in an increase in artefact size for both materials. The application of the gradient echo sequence and use of Ti material generally produced higher distortions than the turbo spin echo sequence and the use of Mg with the exception of the PAR-TSE-TRA-AP/LR protocol at 3.0 T and 7.0 T of the PAR-TSE-SAG-AP protocol at 7.0 T. The Tukey post-hoc test revealed significant pairwise differences between the artefacts size obtained at 1.5 T and 7 T and at 3 T versus 7 T. No significant difference in artefact size was found between 1.5 T and 3 T. The p-values of parameters changed in this investigation are listed in Table 5.

3.1.2. *The influence of Mg in vitro corrosion time on artefact production*

Examining the effect of the Mg implant corrosion time on the artefact size revealed statistically significant results (Table 6). For all magnetic field strengths a general decrease of image distortion was found for increasing *in vitro* corrosion times of the implant (Fig. 5).The spin echo sequence produced lower artefacts than the gradient echo sequence (Fig. 6).

3.2. *Ex vivo results*

Fig. 7 illustrates MR images obtained for rat explants with Mg and Ti pins using the small bore animal 7 T MRI scanner. Ti produced higher distortion of approximately 3 times more TAV than the Mg-based samples ($p < 0.05$) when scanned with the Turbo RARE sequence. TAV averaging highlighted in Fig. 8 indicates a very minor decrease in TAV from one day to thirty days of the Mg samples post-surgery, although not significant. The implantation of the pin into the femur with hard tissue (bone) and soft tissue (muscle) disturbs the anatomic integrity of the images by introducing artefacts as illustrated in Fig. 7.

3.3. *Clinical results*

Fig. 9 shows a decrease in the hypointense area surrounding the implant after one month, three months, and twelve months post-surgery for a single patient. The rest of the patient data follows a comparable trend (Fig. 10). Significant differences were found between healing times and imaging slice positions. An increase in implant degradation and patient healing time resulted in a decrease in artefact production. Imaging the implant at 1.5 months with a T2w TSE sequence in the sagittal direction produced the largest TAV of approximately 650 mm^3. Since the screw is implanted into the scaphoid bone, the shape of the implant in Fig. 9 is defined since it is primarily surrounded by one type of material, spongy bone.

4. Discussion

Postoperative care in the field of orthopaedic surgery relies heavily on precise imaging techniques. Early-stage research of biomaterials concentrates on the assurance of appropriate mechanical and physiological responses between the host and the implant. Further along a product's developmental stage requires insight on product application and translational aspects. Medical imaging compatibility is one of the

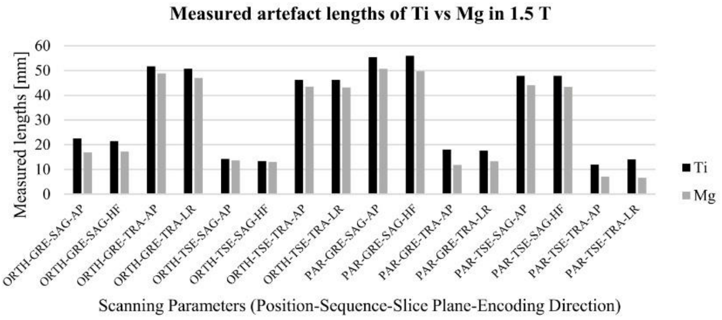

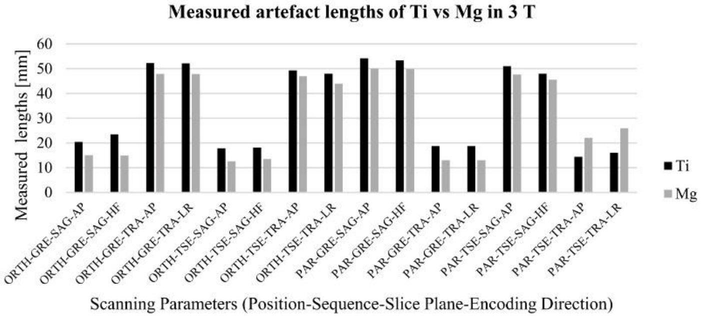

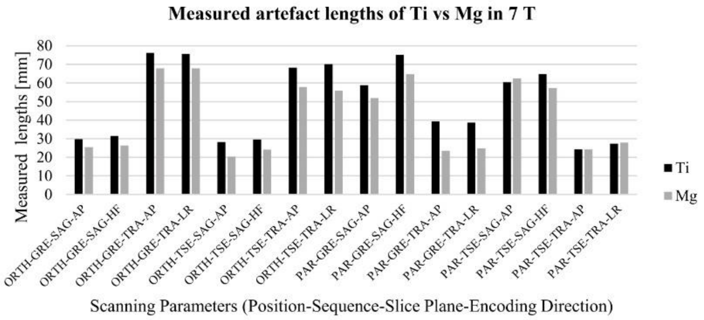

Fig. 3. Measured artefact lengths of Ti and Mg in various magnetic strengths. Implant position relative to the main magnetic field, sequence applied, slice plane, and phase encoding direction were altered for artefact measurements. (Reading format of y-axis: IMPLANT POSITION-SEQUENCE-SLICE PLANE-ENCODING DIRECTION).

Table 4
Average measured metallic artefact of Ti and Mg in MRI along the diameter and length of the implant.

B_0 Field Strength [T]	1.5		3.0		7.0	
Material	Ti	Mg	Ti	Mg	Ti	Mg
Average Diameter [mm]	16.7 ± 3.9	12.5 ± 3.9	18.5 ± 2.7	16.2 ± 5.0	31.1 ± 5.3	24.6 ± 2.2
Average Length [mm]	50.2 ± 3.9	46.3 ± 3.2	51.0 ± 2.4	47.5 ± 2.1	68.7 ± 6.9	60.7 ± 5.9

many focusses. The artefact production of an implant material may sometimes be overlooked but is a key property of the material and must be considered during a product's design process. Previous studies have documented artefact behaviour of magnesium-based implants in MRI [22–24]. Our study is the first which reports on the assessment of artefact behaviour of WE43-based implants in *in vitro, ex vivo,* and clinical environments. Our work adds to the literature by examining the impact of the magnetic field strength on the artefact behaviour. More importantly, our study provides clinically meaningful insights on how degradation time affects artefact behaviour for the experimental setups used in this work.

A well-known and commercially equivalent orthopaedic implant material like Ti is widely used today [25]. With research and popularity

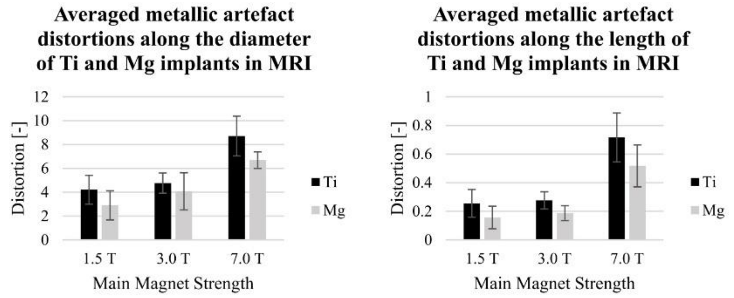

Fig. 4. Averaged artefact distortions of diameter (left) and length (right) measurements of Ti and Mg in MRI.

Table 5
ANOVA and post hoc significance of varied parameters on metallic artefact produced by Ti vs Mg in MRI. Encoding directions are abbreviated as follows: anterior/posterior (AP), head/foot (HF), and right/left (RL).

Parameter	Diameter p-value	Length p-value
B_0 Magnetic Strength	<0.05	<0.05
3 T:1.5 T	0.11	0.73
7 T:1.5 T	<0.05	<0.05
7 T:3 T	<0.05	<0.05
Implant Position	0.68	0.57
Imaging technique (GRE:TSE)	<0.05	<0.05
Phase Encoding Direction	0.62	0.47
HF:AP	0.77	0.67
RL:AP	0.66	0.99
RL:HF	0.98	0.70
Material	<0.05	<0.05

Table 6
ANOVA and post hoc significance of varied parameters on metallic artefact produced by corroded Mg samples for different time points (tp). Encoding directions are abbreviated as follows: anterior/posterior (AP), head/foot (HF), and right/left (RL).

Parameter	Diameter p-value	Length p-value
B_0 Magnetic Strength	<0.05	<0.05
3 T:1.5 T	<0.05	0.40
7 T:1.5 T	<0.05	<0.05
7 T:3 T	<0.05	<0.05
Implant Position	0.60	0.13
Imaging Technique (GRE:TSE)	<0.05	<0.05
Encoding Direction	0.44	0.12
HF:AP	0.51	0.54
RL:AP	0.61	0.82
RL:HF	0.99	0.32
Corrosion Time	<0.05	<0.05
1tp:0tp	0.24	0.98
2tp:0tp	0.21	0.61
3tp:0tp	<0.05	0.11
4tp:0tp	<0.05	0.05
5tp:0tp	<0.05	<0.05
2tp:1tp	0.98	0.95
3tp:1tp	0.98	0.43
4tp:1tp	0.47	0.26
5tp:1tp	0.08	<0.05
3tp:2tp	0.99	0.91
4tp:2tp	0.51	0.79
5tp:2tp	0.09	0.24
4tp:3tp	0.89	0.99
5tp:3tp	0.35	0.82
5tp:4tp	0.94	0.94

of magnesium-based implants increasing, a comparison between the two materials is conceptually appealing. Our findings demonstrate that the Mg-based material outperforms Ti in the *in vitro* environment by producing lower metallic distortion artefacts. Magnetic field perturbations are present around metallic objects in MRI which leads to a modification of hydrogen nuclei precession rates. The change in precession rates results in signal losses or pixel shifts and may manifest in local hypointensities or hyperintensities in MR images. Magnetic field variations are dependent on the magnetic susceptibility of the implant and the surrounding environment (in our case a $CuSO_4$ solution). Since the difference between the magnetic susceptibility of Ti and $CuSO_4$ is pronounced versus the difference between Mg and $CuSO_4$, larger magnetic field distortions are to be expected around a Ti implant.

When introducing corrosion time as a parameter, a decrease in artefact production is noticed as the implant is degraded *in vitro*. As Mg degrades in the body, the base metallic material corrodes forming non-metallic degradation layers composing mainly of MgO and $Mg(OH)_2$ [26]. As such, the base metallic material begins to shrink in volume resulting in a reduced artefact size. This decrease in artefact size is confirmed by our results obtained for a range of *in vitro* corrosion times. The question of how the degradation layer affects artefact production can be answered by analysing the magnetic properties of the degradation layer. Mainly composing of $Mg(OH)_2$ [27], the degradation layer consists of diamagnetic material. As *in vivo* degradation occurs, calcium and magnesium apatite corrosion products additionally form [28]. However, since calcium phosphates are intrinsically diamagnetic, these compounds are trivial with respect to magnetic field interference. Thus, the degradation layer dampens the effects of magnetic field variations caused by the base metallic material. This layer has been reported to be on the micrometer scale [29], which may be assumed to have an almost negligible damping effect.

Standards and norms governed by global organisations, such as ASTM F2119, are referred to by regulatory bodies to ensure patient safety and quality control. Our *in vitro* investigations, based on the ASTM F2119 standard, also considered how parameters such as implant position, encoding direction, and imaging techniques affected artefact production. Of the three, the only parameter that significantly affected artefact production was the MR imaging technique used. In both *in vitro* investigations, GRE imaging generally produced larger artefact size versus fast spin-echo imaging. Spin echo based imaging techniques are less affected by susceptibility artefacts than gradient echo techniques because of the use of a train of refocusing pulses that helps to partially compensate for dephasing of spins caused by metallic objects. Additionally, imaging the diameter of the screw produced larger artefact size than imaging the length of the screw.

Our results add to the literature by providing important insights on how the main magnetic field strength of an MRI system contributes to metallic artefact production. An early study by Ludeke et al. describe show the magnitude of susceptibility artefacts increases with magnetic field strength [30]. This relationship is exemplified in Figs. 4 and 5 where an increase of distortion was observed when moving from 1.5 T to 3.0 T and 7.0 T. It should be noted that conductive implants interact

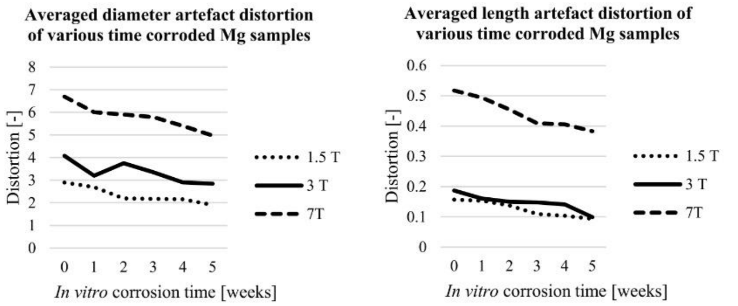

Fig. 5. Averaged diameter (left) and length (right) artefact distortions of Mg-based samples as a function of *in vitro* corrosion time.

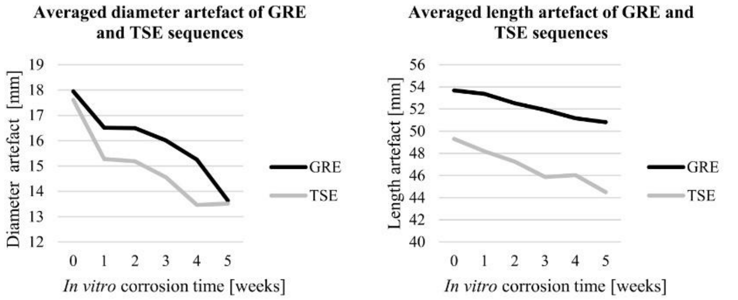

Fig. 6. Averaged diameter (left) and length (right) measured artefacts of Mg-based samples as a function of *in vitro* corrosion time and scanning sequences.

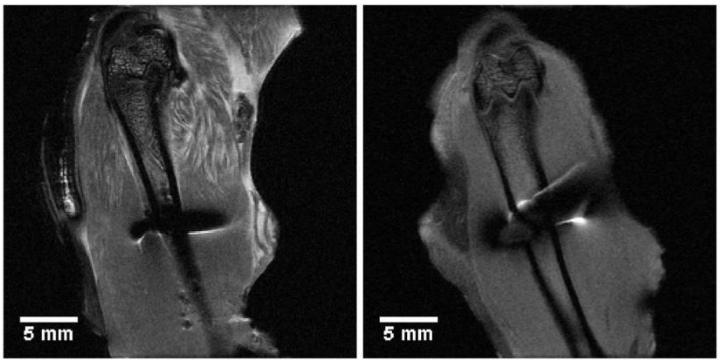

Fig. 7. Example of T1-weighted images of rat femur explants with WE43 and Ti pins implanted transcortical to bone.

with radio frequency (RF) signals from MRI transmitters. These interferences may cause extra artefacts and may even elevate local RF power deposition and energy absorption in the neighbouring region of the implants which may exceed regulatory limits and RF exposure guidelines [31,32].

Explants analysed in this investigation underwent freezing at −20 °C and thawing before scanned in a small animal 7.0 T MRI system. MRI availability could not be synchronised with the euthanasia of the animals and therefore animals needed to be stored. The freezing and thawing cycle has shown to effect MRI by significantly reducing the effective transversal relaxation time T_2* [33]. Such an effect should be considered when interpreting the results. However, the motivation behind our explant analysis is to provide insights into artefact production in hard and soft tissue. Although there were no significant differences obtained for the WE43 samples at different time points, Ti showed an approximately three times larger TAV than the WE43 material.

The clinical results and analysis revealed important information on artefact production of Mg-based implants used to treat scaphoid fractures. Averaging measurements of the four patients included in this investigation followed a similar trend of artefact reduction with patient healing time. The decrease in distortion also provides proof of implant degradation or a loss of metallic base material. More importantly, after averaging all patients and artefacts derived for each imaging plane, an extrapolation of the healing time can be made until the artefact size

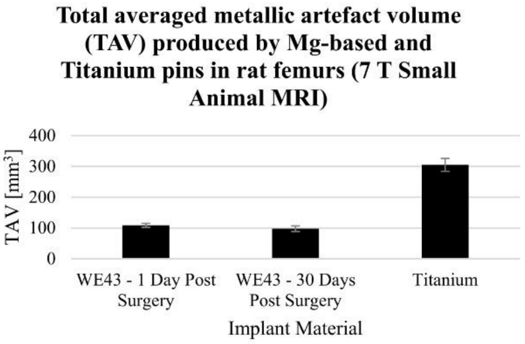

Fig. 8. Total averaged artefact volume produced by pins implanted into rat femurs imaged in 7 T small animal MRI.

reaches zero. Although this extrapolation has limitations (such as implant size), complete disappearance of artefact is approximately reached at 2.1 years, which is in accordance with a one-to-three-year implant resorption period [4,34,35]. Many methods have been employed to track implant degradation rates *in vitro* and *in vivo*, such as computed tomography segmentation and hydrogen gas release [36]. The reduction in metallic artefact size measured in MRI with progressing degradation may offer a viable alternative for screw degradation monitoring and tracking.

This investigation utilised two parameters to quantify artefact production caused by the Mg-based and Ti implants. Distortion quantifications were employed in the *in vitro* measurements while total artefact volume (TAV) was employed in the *ex vivo* and clinical analysis. The inclusion of two measurement methods was chosen to describe the artefact production behaviour of the implants in more than one way. Analysing the two measured quantities show an agreement in the decline of metallic distortion trend of Mg during the degradation process.

Metal artefact reduction techniques are widely used today to negate the effects of metallic implants in MRI [37]. Various specialised software and MRI vendors provide dedicated imaging techniques tailored for reducing metallic artefacts. Since these approaches vary from MRI vendor to vendor, our study excluded their impact as it is out of the scope of this study. However, the literature reports that some metal artefact reduction techniques do not produce statistically significant results when applied to Mg [24]. Examining the efficacy of these metal artefact reduction techniques on Mg-based material warrants further investigation.

A limitation of the *in vitro* aspect of this study is found in the natural behaviour of Mg itself. The inherent corrosion process of the implants made it impractical for samples to be tested more than once due to the interaction with $CuSO_4$ solution. Regarding explant analysis, the movement of blood is avoided in the *ex vivo* animal studies so that blood motion artefacts are eliminated. An increase in explant samples and clinical patients would enhance the statistical power of our findings.

Future studies should include the examination of different animal models to gain insights for other orthopaedic applications or solutions. Alternative *in vitro* implant degradation methods can be used to mimic specific environments. These methods should also be analysed to investigate how the degradation method affects artefact production. Furthermore, the inclusion of multi-modal data such as clinical computed tomography can be explored in quantifying an implant volume to MRI artefact production ratio.

Assessing the artefact production behaviour of Mg-based implants *in vitro, ex vivo,* and in clinical application provides valuable insights into the material's properties and its implications for MRI image quality. Our results demonstrate that Mg-based implants displayed a decrease in metallic artefact production with implant degradation. As the implant degrades and artefact production decreases, better visualisation of bone healing is achieved. To summarise, the Mg-based implant outperformed the Ti material by inducing lower artefact size.

5. Conclusion

In this investigation, *in vitro, ex vivo,* and clinical studies demonstrate a reduction in artefact size with implant degradation time for Mg-based screws. The largest artefact behaviour or "worst-case" scenario caused by the WE43 implants were found when imaging the non-degraded state in the *in vitro* and *ex vivo* experiments. In the clinical study, the largest

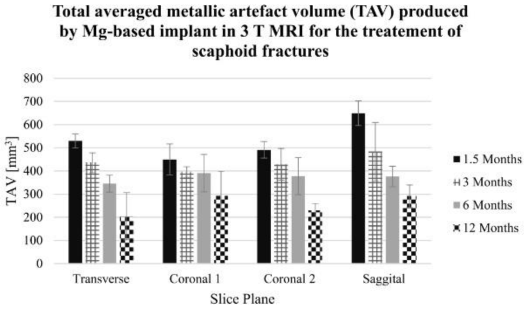

Fig. 10. Total artefact volume produced by Mg-based implant as a function of healing time in different slice planes in 3 T MRI.

Fig. 9. T2-weighted images of scaphoid with Mg-based screw one (left), three months (middle), and twelve months (right) after surgery. White arrows indicate position of implant.

TAV was observed when imaging the implant at 1.5 months in the sagittal plane. When compared against Ti-based implants, the Mg-based material induces significantly lower artefacts. Translational findings from this study suggests that Mg-based implant material should be promoted for future orthopaedic solutions due to lower artefact production. Further clinical studies are required to determine degradation rates based on artefact production as an alternative approach for degradation tracking.

CRediT authorship contribution statement

Jonathan Espiritu: Conceptualization, Methodology, Software, Validation, Formal analysis, Investigation, Resources, Data curation, Writing – original draft, Visualization. **Mostafa Berangi:** Investigation, Data curation. **Christina Yiannakou:** Formal analysis, Investigation, Resources, Data curation. **Eduarda Silva:** Methodology, Resources. **Roberto Francischello:** Data curation, Resources. **Andre Kuehne:** Investigation, Data curation, Writing – review & editing, Supervision. **Thoralf Niendorf:** Resources, Writing – review & editing. **Sören Könneker:** Methodology, Resources, Data curation. **Regine Willumeit-Römer:** Conceptualization, Supervision, Project administration, Funding acquisition. **Jan-Marten Seitz:** Conceptualization, Validation, Resources, Writing – review & editing, Supervision, Project administration, Funding acquisition.

Declaration of competing interest

Authors Kuehne and Berangi are employees of MRI.TOOLS GmbH. Author Niendorf is CEO and founder of MRI.TOOLS GmbH. Syntellix AG is a medical technology manufacturer of metallic and bio-absorbable clinical implants. Authors Espiritu and Seitz are employed as Research Associate and Chief Technical Officer, respectively.

Acknowledgements

We would like to thank Eileen Höltje and Fabian Willers from Syntellix AG (Hannover, Germany) and Roman Leicht from MRI.TOOLS GmbH (Berlin, Germany) for their support with the experiments. We would also like to acknowledge the help from Petra Keilberg, Gianni Novani, Hana Hlavata, and Matteo Bianchi from the Fondazione Toscana Gabriele Monasterio Hospital (Pisa, Italy) and Luca Menichetti from the Institute of Clinical Physiology, National Research Council (Pisa, Italy) for their support. This project has received funding from the European Union's Horizon 2020 research and innovation programme under the Marie Skłodowska-Curie grant agreement No 811226.

References

[1] B. Heublein, R. Rohde, V. Kaese, M. Niemeyer, W. Hartung, A. Haverich, Biocorrosion of magnesium alloys: a new principle in cardiovascular implant technology? Heart 89 (6) (2003) 651–656.
[2] G. Marcucci, M.L. Brandi, Kyphoplasty and vertebroplasty in the management of osteoporosis with subsequent vertebral compression fractures, Clin. Cases Mineral Bone Metabol. 7 (1) (2010) 51–60.
[3] H. May, Y.A. Kati, G. Gumussuyu, T.Y. Emre, M. Unal, O. Kose, Bioabsorbable magnesium screw versus conventional titanium screw fixation for medial malleolar fractures, J. Orthop. Traumatol. 21 (9) (2020).
[4] C. Plaass, C. von Falck, S. Ettinger, L. Sonnow, F. Calderone, A. Weizbauer, J. Reifenrath, L. Claassen, H. Waizy, K. Daniilidis, C. Stukenborg-Colsman, H. Windhagen, Bioabsorbable magnesium versus standard titanium compression screws for fixation of distal metatarsal osteotomies – 3 year results of a randomized clinical trial, J. Orthop. Sci. 23 (2) (2018) 321–327.
[5] R. Biber, J. Pauser, M. Brem, H.J. Bail, Bioabsorbable metal screws in traumatology: a promising innovation, Trauma Case Rep. 8 (2017) 11–15.
[6] H. Brar, J. Wong, M. Manuele, Investigation of mechanical and degradation properties of Mg-Sr and Mg-Zn-Sr alloys for use as potential biodegradable implants materials, J. Mech. Behav. Biomed. Mater. 7 (2012) 87–95.
[7] A. Chatterjee, C. Harmath, A. Oto, New prostate MRI techniques and sequences, Abdominal Radiol. 45 (2020) 4052–4062.
[8] P. Stroman, H. Warren, G. Ioachim, J. Powers, K. McNeil, A comparison of the effectiveness of functional MRI analysis methods for pain research: the new normal, PLoS One 15 (12) (2020).
[9] C. Nunez-Peralta, J. Alonso-Perez, J. Diaz-Manera, The increasing role of muscle MRI to monitor changes over time in untreated and treated muscle diseases, Curr. Opin. Neurol. 33 (5) (2020) 611–620.
[10] D.P. Frush, K. Applegate, Computed tomography and radiation: understanding the issues, J. Am. Coll. Radiol. 1 (2) (2004) 113–119.
[11] E. Weidman, K. Dean, W. Rivera, M. Loftus, T. Stokes, R. Min, MRI saftey: a report of current practise and advancements in patient preparation and screening, Clin. Imag. 39 (6) (2015) 935–937.
[12] P.M. Jungmann, C.A. Agten, C.W. Pfirrmann, R. Stutter, Advances in MRI around metal, J. Magn. Reson. Imag. 46 (4) (2017) 972–991.
[13] J. Espiritu, M. Meier, J.-M. Seitz, The current performance of biodegradable magnesium-based implants in magnetic resonance imaging: a review, Bioact. Mater. 6 (12) (2021) 4360–4367.
[14] Azo Materials, Magnesium Elektron WE43 Alloy (UNS M18430), 18 June 2013 [Online]. Available: https://www.azom.com/article.aspx?ArticleID=9279. (Accessed 7 October 2021).
[15] ASTM International, ASTM standard F3268-18a, in: Standard Guide for in Vitro Degradation Testing of Absorbable Metals, West Conshohocken, PA, 2018.
[16] ASTM International, ASTM standard F2119-07, in: Standard Test Method for Evaluation of MR Image Artifacts from Passive Implants, West Conshohocken, PA, 2013.
[17] V. Hurst, A. Ahluwalia, S. Alam, M. Avey, M. Baker, W. Browne, A. Clark, I. Cuthill, U. Dirnagl, M. Emersion, P. Garner, S. Holgate, D. Howells, N. Karp, S. Lazic, K. Lidster, C. MacCallum, M. Macleod, E. Pearl, O. Petersen, et al., The ARRIVE guidelines 2.0: updated guidelines for reporting animal research, PLoS Biol. 18 (7) (2020).
[18] J.F. Debatin, S.N. Nadel, H. Sostman, C. Spritzer, A.J. Evans, T.M. Grist, Magnetic resonance imaging—Cardiac ejection fraction measurements, Invest. Radiol. 27 (3) (1992) 198–203.
[19] S. Könneker, K. Krockenberger, C. Pieh, C. von Falck, B. Brandewiede, P. Vogt, M. Kirschner, A. Ziegler, Comparison of SCAphoid fracture osteosynthesis by MAGnesium-based headless Herbert screws with titanium Herbert screws: protocol for the randomized controlled SCAMAG clinical trial, BMC Muscoskel. Disord. 20 (2019) 357.
[20] A. Chan, J. Tetylaff, D. Altman, A. Laupacis, P. Gotzsche, K. Krleza-Jeric, A. Hrobjartsson, H. Mann, K. Dickersin, J. Berlin, C. Dore, W. Parulekar, W. Summerskill, T. Groves, K. Schulz, H. Sox, F. Rockhold, D. Rennie, D. Moher, SPIRIT 2013 statement: defining standard protocol items for clinical trials, Ann. Intern. Med. 158 (3) (2013) 200–207.
[21] CONSORT Group, CONSORT 2010 Statement: updated guidelines for reporting parallel group randomised trials, PLoS Med. (2010).
[22] T. Ernstberger, G. Buchhorn, G. Heidrich, Intervertebral test spacers and postfusion MRI artifacting: a comparative in vitro study of magnesium versus titanium and carbon fiber reinforced polymers as biomaterials, Open Med. 4 (4) (2009) 496–500.
[23] L. Fili, R. Luechinger, T. Frauenfelder, S. Beck, R. Guggenberger, N. Farshad-Amacker, G. Andreisek, Metal-induced artifacts in computed tomography and magnetic resonance imaging: comparison of a biodegradable magnesium alloy versus titanium and stainless steel controls, Skeletal Radiol. 44 (6) (2015) 849–856.
[24] L. Sonnow, S. Könneker, P.M. Vogt, F. Wacker, C. von Falck, Biodegradable magnesium Herbert, BMC Med. Imag. 17 (16) (2017).
[25] M.S.K. Kaur, Review on titanium and titanium based alloys as biomaterials for orthopaedic applications, Mater. Sci. Eng. C 102 (2019) 844–862.
[26] J. Seitz, R. Eifler, F. Bach, H. Maier, Magnesium degradation products: effects on tissue and human metabolism, J. Biomed. Mater. Res. 102 (10) (2014) 3744–3753.
[27] R. Rettig, S. Virtanen, Composition of corrosion layers on a magnesium rare-earth alloy in simulated body fluids, J. Biomed. Mater. Res. 88A (2) (2008) 359–369.
[28] J. Seitz, R. Eifler, W. Bach, H. Maeir, Magnesium degradation products: effects on tissue and human, J. Biomed. Mater. Res. 102 (10) (2013) 3744–3753.
[29] R. Willumeit-Römer, The interface between degradable Mg and tissue, JOM 71 (4) (2019) 1447–1455.
[30] K.M. Lüdeke, P. Röschmann, R. Tischler, Susceptibility artefacts in NMR imaging, Magn. Reson. Imag. 3 (4) (1985) 329–343.
[31] International Electrical Commision, International standard, medical equipment - Part 2: particular requirements for the safety of magnetic resonance equipment for medical diagnosis, 2nd Revision, in: International Electrotechnical Commission 60601-2-33, 2002, pp. 29–31.
[32] ICNIRP, Guidelines for limiting exporsure to time-varying electric, magnetic, and electromagnetic fields (up to 300 GHz), Health Phys. 74 (4) (1998) 494–522.
[33] S.L. Pownder, P.H. Shah, H.G. Potter, M.F. Koff, The effect of freeze-thawing on magnetic resonance imaging T2* of freshly harvested bovine patellar tendon, Quant. Imag. Med. Surg. 5 (3) (2015) 368–373.
[34] H. Waizy, J. Diekmann, A. Weizbauer, J. Reifenrath, I. Bartsch, V. Neubert, R. Schavan, H. Windhagen, In vivo study of a biodegradable orthopedic screw (MgYREZr-alloy) in a rabbit model for up to 12 months, J. Biomater. Appl. 28 (5) (2013) 667–675.

[35] H. Waizy, J. Seitz, J. Reifenrath, A. Weizbauer, F. Bach, A. Meyer-Lindenberg, B. Denkena, H. Windhagen, Biodegradable magnesium implants for orthopedic applications, J. Mater. Sci. 48 (2013) 39–50.
[36] L. Liu, K. Gebresellasie, B. Collins, H. Zhang, Z. Xu, J. Sankar, Y. Lee, Y. Yun, Degradation rates of pure zinc, magnesium, and magnesium alloys measured by volume loss, mass loss, and hydrogen evolution, Appl. Sci. 8 (9) (2018) 1459.
[37] M. Reichert, T. Ai, J.N. Morelli, M. Nittka, U. Attenberger, V.M. Runge, Metal artefact reduction in MRI at both 1.5 and 3.0Tusing slice encoding for metal artefact correction and view angle tilting, Br. J. Radiol. 88 (2015) 1048.

Publication 2

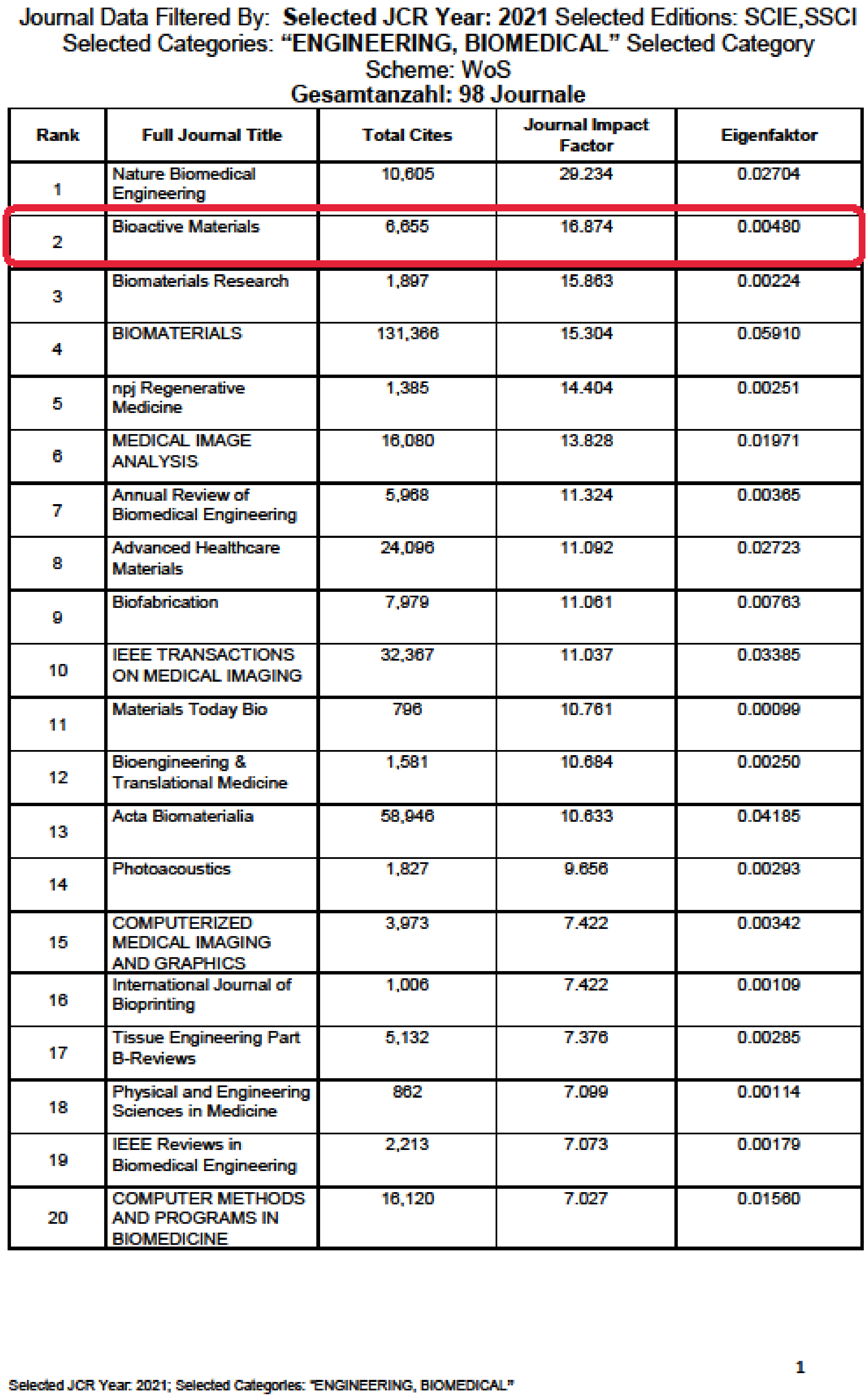

Journal Data Filtered By: **Selected JCR Year: 2021** Selected Editions: SCIE,SSCI
Selected Categories: **“ENGINEERING, BIOMEDICAL”** Selected Category
Scheme: WoS
Gesamtanzahl: 98 Journale

Rank	Full Journal Title	Total Cites	Journal Impact Factor	Eigenfaktor
1	Nature Biomedical Engineering	10,605	29.234	0.02704
2	Bioactive Materials	6,655	16.874	0.00480
3	Biomaterials Research	1,897	15.863	0.00224
4	BIOMATERIALS	131,366	15.304	0.05910
5	npj Regenerative Medicine	1,385	14.404	0.00251
6	MEDICAL IMAGE ANALYSIS	16,080	13.828	0.01971
7	Annual Review of Biomedical Engineering	5,968	11.324	0.00365
8	Advanced Healthcare Materials	24,096	11.092	0.02723
9	Biofabrication	7,979	11.061	0.00763
10	IEEE TRANSACTIONS ON MEDICAL IMAGING	32,367	11.037	0.03385
11	Materials Today Bio	796	10.761	0.00099
12	Bioengineering & Translational Medicine	1,581	10.684	0.00250
13	Acta Biomaterialia	58,946	10.633	0.04185
14	Photoacoustics	1,827	9.656	0.00293
15	COMPUTERIZED MEDICAL IMAGING AND GRAPHICS	3,973	7.422	0.00342
16	International Journal of Bioprinting	1,006	7.422	0.00109
17	Tissue Engineering Part B-Reviews	5,132	7.376	0.00285
18	Physical and Engineering Sciences in Medicine	862	7.099	0.00114
19	IEEE Reviews in Biomedical Engineering	2,213	7.073	0.00179
20	COMPUTER METHODS AND PROGRAMS IN BIOMEDICINE	16,120	7.027	0.01560

Selected JCR Year: 2021; Selected Categories: "ENGINEERING, BIOMEDICAL"

1

Bioactive Materials 25 (2023) 86–94

Contents lists available at ScienceDirect

Bioactive Materials

journal homepage: www.keaipublishing.com/en/journals/bioactive-materials

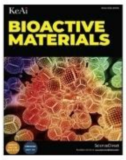

Radiofrequency induced heating of biodegradable orthopaedic screw implants during magnetic resonance imaging

Jonathan Espiritu [a,*], Mostafa Berangi [b,c,d], Hanna Cwieka [e], Kamila Iskhakova [e], Andre Kuehne [b], D.C. Florian Wieland [e], Berit Zeller-Plumhoff [e], Thoralf Niendorf [b,c,d], Regine Willumeit-Römer [e], Jan-Marten Seitz [a]

[a] *Syntellix AG, Hannover, Germany*
[b] *MRI.TOOLS GmbH, Berlin, Germany*
[c] *Charité – Universitätsmedizin Berlin, Corporate Member of Freie Universität Berlin and Humboldt Universität zu Berlin, Berlin, Germany*
[d] *Berlin Ultrahigh Field Facility (B.U.F.F.), Max-Delbrueck Center for Molecular Medicine in the Helmholtz Association, Berlin, Germany*
[e] *Institute of Metallic Biomaterials, Helmholtz Zentrum Hereon, Geesthacht, Germany*

ARTICLE INFO

Keywords:
Biodegradable implants
Magnesium
Medical imaging
Magnetic resonance imaging
Patient safety

ABSTRACT

Magnesium (Mg)-based implants have re-emerged in orthopaedic surgery as an alternative to permanent implants. Literature reveals little information on how the degradation of biodegradable implants may introduce safety implications for patient follow-up using medical imaging. Magnetic resonance imaging (MRI) benefits post-surgery monitoring of bone healing and implantation sites. Previous studies demonstrated radiofrequency (RF) heating of permanent implants caused by electromagnetic fields used in MRI. Our investigation is the first to report the effect of the degradation layer on RF-induced heating of biodegradable orthopaedic implants.

WE43 orthopaedic compression screws underwent *in vitro* degradation. Imaging techniques were applied to assess the corrosion process and the material composition of the degraded screws. Temperature measurements were performed to quantify implant heating with respect to the degradation layer. For comparison, a commercial titanium implant screw was used.

Strongest RF induced heating was observed for non-degraded WE43 screw samples. Implant heating had shown to decrease with the formation of the degradation layer. No statistical differences were observed for heating of the non-degraded WE43 material and the titanium equivalent. The highest risk of implant RF heating is most pronounced for Mg-based screws prior to degradation. Amendment to industry standards for MRI safety assessment is warranted to include biodegradable materials.

1. Introduction

Rise in aging population, technological advancements, and availability of better medical facilities drive the prevalence of orthopaedic implantations [1]. With the resorption of biodegradable materials, the need for implant removal using secondary surgery is averted along with significant reduction of patient burden and health care costs. Interest in magnesium (Mg)-based materials has shown exponential increase as a contemporary alternative to traditional permanent implants [2–5]. The appeal is warranted by the material's appropriate biocompatibility [6] and mechanical properties [3].

Postoperative care of orthopaedic implants is aided by imaging of implantation sites to monitor the healing process of surrounding bone and tissues, and to assess the implant status [7–9]. MRI presents a viable approach for the examination of implantation sites due to its superb bone-soft tissue contrast and the use of non-ionizing radiation. Mg-based implants have shown to be compatible with MRI providing good visualization due to their lower metallic artefact production [9]. However, the metallic and electrically conductive nature of Mg-based and other metallic implants constitutes challenges for MRI. Implant and tissue heating due to interactions between conductive implants and electromagnetic (EM) fields may lead to tissue heating and thus compromise patient safety [10].

Implant heating may be induced by exposure to two time-varying

---

Peer review under responsibility of KeAi Communications Co., Ltd.

* Corresponding author.

E-mail address: espiritu@syntellix.com (J. Espiritu).

https://doi.org/10.1016/j.bioactmat.2023.01.017
Received 23 November 2022; Received in revised form 19 January 2023; Accepted 21 January 2023

fields required for MRI: RF field transmission (B_1^+) induced heating and heating caused by switched magnetic field gradients (B_G) [10]. MRI uses radiofrequency (RF) power transmission for signal and image generation. Having base frequencies in the MHz, B_1^+ is provided by a transmit RF coil used for spin excitation. Spatial encoding used for MR image generation is achieved by switched magnetic field gradients B_G, with frequencies found in the kHz range [11,12]. Following Faraday's law, time-varying magnetic fields are inherently accompanied by electric fields (E-fields), generating so called eddy currents. Induced eddy currents can deposit power into implants and further induce secondary EM fields around the implant, which may cause tissue heating. Owing to the material, shape, location, orientation, and degradation state of a conductive implant, the level of RF power deposition induced heating and heating induced by switched magnetic field gradients may vary [13,14].

Due to the geometry of orthopaedic screws, RF heating is of critical concern. The specific absorption rate (SAR) describes the temporal averaged absorbed RF power P_{RF} over time per exposed mass Δm [10]:

$$SAR = \frac{\langle P_{RF} \rangle_t}{\Delta m} = \frac{\sigma \langle |E|^2 \rangle_t}{2\rho}$$

As such, the SAR is governed by tissue parameters and MRI hardware. Electrical conductivity σ and mass density ρ are inherent to the surrounding tissue, while the E-field E is dictated by the imaging hardware. To limit heating and to prevent high SAR, MR techniques and protocols have been modified by reducing the power of RF excitation pulses and by increasing the repetition time between RF excitation pulses. A plethora of reports presents more sophisticated MRI hardware and methodology tailored for mitigation of RF induced implant heating [15–17]. Pioneering approaches include modification of RF transmission fields using RF arrays and parallel transmission with maximum and null current modes [18,19].

The induced eddy currents caused by the effective transmission field B_1^+ are condensed to the surface of the metal due to the "skin effect", a law of electrodynamics. Though the heating of the small implant mass (such as a screw) may be negligible, the secondary (scattered) E-field induced by the eddy currents becomes hazardous at critical locations along the implant [10]. RF currents indirectly induced in the neighbouring tissue by the secondary E-field are thus the major contributor to RF induced heating. Furthermore, thin wires, screws, and other one-dimensional-like geometries may succumb to the "antenna effect". This effect describes intensity peaks when the implant length falls within one-quarter to one-half of the RF wavelength found in tissue [20]. Thus, elevated heating may be observed for thin geometries since the secondary E-field is optimal under these conditions, more predominantly at the implant tip ends.

Prior to market entry, various tests are undertaken to ensure medical devices conform to their respective standards. With support from governmental agencies, international standards have been established to ensure patient safety during MRI studies [10]. Noteworthy standards regarding implant heating in MRI include ASTM F2182 [21], IEC 60601-2-33 [22], and ISO/TS 10974 [23]. To this end, responsibility falls upon manufacturers of medical devices to minimize hazardous risk and uphold patient safety.

Previous studies have documented heating caused by permanent metallic implants in MRI [11,24–26]. Furthermore, particular studies have utilised computational modelling methods to estimate RF-induced heating [27–30]. Mg-based materials have additionally been employed for thermal ablation of tumours utilising the eddy thermal effect [31]. However, the literature does not reveal reports elucidating RF induced heating of biodegradable orthopaedic implants. How the degradation layer can affect potential heating in MRI is of high clinical relevance, still unknown and warrants additional exploration. To close this gap, this study first carefully characterizes the degradation layer of *in vitro* corroded Mg-based biodegradable orthopaedic compression screws (WE43) using micro computed tomography, X-ray diffraction, scanning electron microscopy and energy dispersive X-Ray electron microscopy. This material characterization is followed by an examination of the impact of the degradation layer state on RF-induced heating in MRI of WE43 materials. For evaluation, temperature profiles obtained for WE43 material are benchmarked against temperature profiles derived from a commercial titanium implant screw equivalent. We hypothesise that the degradation layer formed around the base material of a Mg-based biodegradable screw over time disrupts secondary E-field distribution which may lessen RF heating of the surrounding environment, and may benefit MRI aided monitoring of implantation sites.

2. Materials and methods

2.1. Sample preparation

Mg-based (WE43) orthopaedic compression screws (Syntellix AG, Hannover, Germany) 40 mm in length and 3.2 mm in diameter underwent *in vitro* degradation. The WE43 alloy is comprised of magnesium alloyed with Yttrium, Rare Earth Elements, and Zirconium [32]. To compare the heating profile of a non-degraded WE43 sample to alternatives, a titanium commercial equivalent was included (Fig. 1). The WE43 samples were immersed and corroded in a modified ASTM F3268 Standard [33] with Dulbecco's Phosphate Buffered Saline (DPBS). As described by the standard, the temperature of the corrosion medium was kept at 37 ± 1 °C with a pH of approximately 7.4 ± 0.2. A specimen was placed in 2.5 L of the medium which was kept constant and replaced if evaporation were to occur. If a measured pH registered above a pH of 7.6, the corrosion medium was treated with a HCl buffering solution.

24 screws were immersed and degraded in the solution for eight time points (three samples per time point) ranging from one-week to eight-weeks with an increment of one week. Once the specified immersion time elapsed, the samples underwent cleaning with distilled water and were rinsed with ethanol to remove salts and prevent further oxidation. The Ti sample was assumed to have negligible degradation within the time frame of this degradation setup.

2.2. Material characterisation

A randomly selected subset of the degraded screws for each time-period was chosen to be imaged with various techniques to provide qualitative and quantitative data of the degradation layer developed under the chosen corrosion method.

2.2.1. Micro-computed tomography

The *in vitro* degraded screws underwent micro-computed tomography (µCT) to observe changes to the geometry of the screw as corrosion time continued. The samples were first imaged by a laboratory µCT scanner (Phoenix Nanotom by Baker Hughes, Celle, Germany) with scanning parameters described in Table 1. The scans were reconstructed in Datos|x (Baker Hughes, Celle, Germany) where potential movement caused by the rotating stage was corrected using an optimisation function. The raw data was then segmented using Fiji/ImageJ [34] by first applying anisotropic diffusion to reduce noise. Then, a trainable WEKA segmentation [35] was applied to segment the base material, degradation layer, and background. Additionally, the segmented base material was utilised to calculate the mass loss of the degraded samples.

2.2.2. X-ray diffraction

X-ray diffraction (XRD) was performed at P07 side station at the PETRA III storage ring at Deutsches Elektronen-Synchrotron (DESY, Hamburg, DE) [36] to describe the crystalline structure of the degradation layer. An X-ray beam with an energy of 87.1 keV and 0.5 beam size was applied to the top of two-, four-, six-, and eight-week time point screw samples a total of three times each. A Perkin Elmer XRD 1621 Flat Panel Detector (PerkinElmer, Waltham, United States) was placed at

Fig. 1. 40 mm Mg-based orthopaedic compression screw MAGNEZIX® CS ø 3.2 (top) and Ti equivalent (bottom), reproduced under the CC BY-NC-ND 4.0 License [9].

Table 1
μCT measurement parameter details applied to image the degraded WE43 screw samples.

Scanning Parameter	Value
Sample distance [mm]	20
Detector distance [mm]	200
Timing per projection [ms]	2400
Frames per projection	5
Number of images	2000
Voltage [kV]	125
Current [μA]	45
Isotropic voxel size [μm]	5

1.485 m from the samples. The samples were subjected to 0.5 s of exposure time. Lanthanum hexaboride (Lab6) was used as a calibrant. The acquired XRD images were processed using Dawn Science 2.18.0 (Diamond Light Source, Didcot, UK) [37]. Diffractograms were analysed using MATLAB R2018 (The MathWorks Inc., US) and averaged along with a slice in a direction perpendicular to the screw axis. The final plots were normalized according to Mg (101) peak intensity.

2.2.3. Scanning electron microscopy and energy dispersive X-ray spectroscopy

Scanning electron microscopy (SEM) and energy dispersive X-ray spectroscopy (EDX) analysis were employed to characterise the cross section along the longitudinal axis of the degraded screws in terms of qualitative imaging and elemental composition of the degradation layer. Imaging was acquired by a Tescan Vega SB-U III (Tescan, Czech Republic) at Helmholtz-Zentrum Hereon (Geesthacht, Germany). Images were taken in backscattered electron mode (BSE mode) to emphasize the differences between the residual material and the degradation layer. The EDX measurements were performed as mapping of a chosen region of interest. The SEM and EDX measurements details can be found in Table 2. Zero-, Two-, four-, six-, eight-week degraded samples were embedded in methyl methacrylate liquid and powder (Demotec®, Demotec, Germany) before being ground and polished on a Saphir 320/Rubin 520 machine (QATM, Advanced Materialography, Germany). Subsequently, the samples were sputtered with carbon to provide appropriate conductivity for the SEM and EDX measurements.

2.3. Temperature measurements during MRI examination

A 3.0 T (Skyra Fit, Siemens, Erlangen, Germany) MRI scanner was used for *in vitro* measurements. The various degraded samples and titanium equivalent underwent a procedure adapted from ASTM F2182 [21]. The MR scanning parameters used during the heating measurements are summarized in Table 3.

Table 2
SEM and EDX measurement parameter details applied to image the degraded WE43 screw samples.

Parameter	SEM	EDX
Voltage [kV]	15	15
Magnification [x]	50	2000
Beam intensity [−]	10	15

A rectangular case with dimensions defined by the ASTM Standard was constructed from acrylic glass and was filled with a phantom gel. The tissue-mimicking phantom was prepared with 1.32 g/L of NaCl (Sigma Aldrich, Taufkirchen, Germany), 10 g/L of polyacrylic acid (Sigma Aldrich, Taufkirchen, Germany), and 25 L of distilled water. Prior to each specimen heating test, local incident field calibration was performed as described by ASTM F2182 [21].

A non-conducting 3D-printed holder was developed to hold the specimen and to guide fibre-optic probes from the thermometry system (model T1; Neoptix Inc., Québec, Canada) to the tips of the implants which define the highest heating points [38]. A total of three probes were used, two placed at the implant ends, and one control probe placed on the opposite side of the phantom to measure heating sans implant influence. The position of the probes was adjusted between every sample scan to ensure the distance between the probes and the implant was consistent. The holder with a single screw sample was placed centred 2 cm from the phantom wall and aligned to the main magnetic field, as this position has been previously determined as the location with maximum heating [39]. The acrylic case was then placed in a Styrofoam insulation container for scanning as illustrated in Fig. 2.

Prior to heating measurements, the gel phantom was brought to scanning room temperature 24 h beforehand. The temperature was recorded 2 min before and 2 min after the scanning sequence was applied at intervals of 1 s. For each sample, one measurement was taken without the sample, and another measurement was taken with the sample placed in the phantom to assess the increase in temperature due to the device itself. Screw samples from weeks six to eight did not

Table 3
MRI scanning parameters used during heating measurements of the screw samples.

B0 Field strength [T]	3.0
RF coil type (transmission)	Body RF coil
RF coil type (reception)	32 channel spine RF array
Imaging technique	Turbo-spin-echo (TSE)
TR [ms]	5820
Inter-echo time TE [ms]	6.8
Echo train length	8
Imaging Plane	Transversal
Excitation flip angle [°]	120
Pulse Width [ms]	1.28
Transmitter Power [W]	90.7
FOV [mm]	450
Matrix size [pixel]	512
Slice thickness [mm]	3.4
Total slices	24
Whole body-SAR [W/kg]	2
Patient Body Weight [kg]	70
Number of Averages	20
Scan time [s]	939

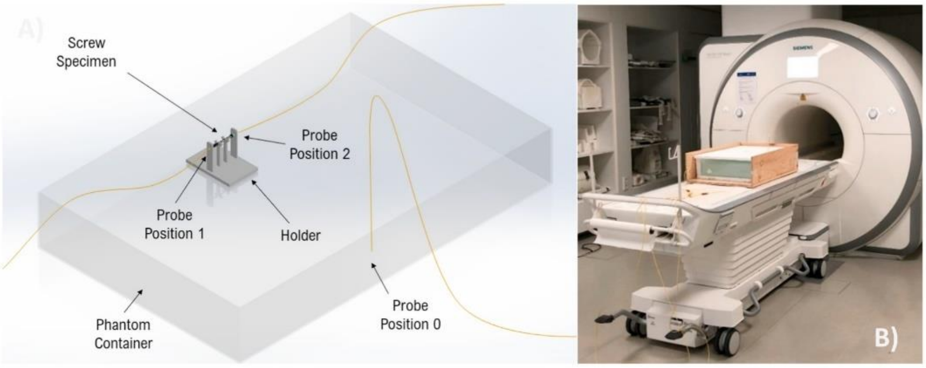

Fig. 2. Heating measurement setup based on ASTM F2182 depicting the MRI scanner (A) and the phantom (B). For the temperature measurements the phantom setup was moved into the isocenter of the MR scanner.

succumb to heating measurements as the samples fractured during the *in vitro* degradation process.

2.4. Statistics

Statistical analyses were performed using RStudio (RStudio, USA). A p-value of <0.05 was chosen to be statistically significant. To compare the increases in temperature and mass loss between the various degraded WE43 time-points, a two-way analysis of variance (ANOVA) was performed. Additionally, the ANOVA test was also applied to determine the differences between the WE43 material and the equivalent titanium implant. If any significant results were determined, a Turkey's post hoc comparison procedure was utilised to perform pairwise comparisons.

3. Results

3.1. Material characterisation

3.1.1. Micro-computed tomography

The degraded specimens were scanned via μCT to capture the physical geometry of both the base material and the degradation products. Time-points after the fifth week were excluded due to specimen breaking during corrosion process. An example is outlined in Fig. 3. Non-uniform pitting corrosion is clearly visible from the μCT images (Fig. 3A). Segmentation applied to the μCT images (Fig. 3B) successfully differentiated base material from the degradation products. From the segmented images, it is evident that the degradation layer unevenly penetrates the base material from the inner canulation and more evidently from the outer surface of the screws. A build-up of degradation product is also visible in the cannulation. A fully realised 3D object file of the base material is visible in Fig. 3C.

The segmented base material was utilised to calculate any significant differences between the mass loss during the selected degradation periods. The statistical tests revealed a significant difference between the degraded timepoints ($p < 0.05$). A summary of the pairwise comparisons are shown in Table 4.

3.1.2. X-ray diffraction

$Mg(OH)_2$, MgO, $MgCO_3$, $CaCO_3$, and $MgHCO_3{\cdot}3H_2O$ degradation products were identified by means of XRD as shown in Fig. 4 (left). The more predominant peaks observed were contributed by $Mg(OH)_2$ and MgO, suggesting the presence of higher crystalline phases of these products. With respect to the time course, the intensity of the $Mg(OH)_2$

Table 4
Post hoc significant differences of paired degradation time points (tp).

Pairwise comparison of degraded tps	p-value
1tp:0tp	<0.05
2tp:0tp	<0.05
3tp:0tp	<0.05
4tp:0tp	<0.05
5tp:0tp	<0.05
2tp:1tp	0.55
3tp:1tp	<0.05
4tp:1tp	<0.05
5tp:1tp	<0.05
3tp:2tp	0.31
4tp:2tp	<0.05
5tp:2tp	<0.05
4tp:3tp	<0.05
5tp:3tp	<0.05
5tp:4tp	0.99

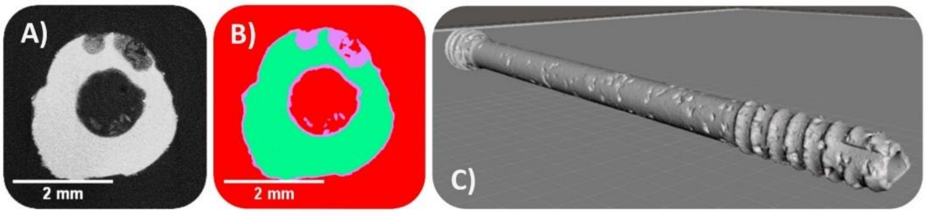

Fig. 3. Exemplary results derived from μCT of degraded specimens. The raw μCT data (A) showing a cross-section approximately 12 mm from the top of the screw is first segmented (B) to create a 3D view (C). The segmented image shows the base metallic material in green, degradation product in purple, and background pixels in red.

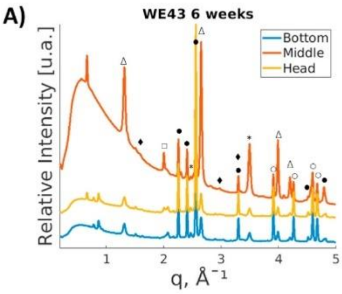

Fig. 4. Diffractograms for the middle section of the screws after two, four, six, and eight weeks in solution (A). Peak assignment is illustrated with the following symbols: ● for Mg, Δ for $Mg(OH)_2$, ○ for MgO, * for $MgCO_3$, ◊ for CaCO3, and □ for $MgHCO_3{\cdot}3H_2O$. Diffractograms of the head, middle, and bottom parts of three averaged samples after eight weeks of immersion time (B). The intensities are normalized with respect to (101) Mg Bragg's peak.

peaks increased with degradation period, while MgO remained at a constant intensity. Additionally, Fig. 4 (right) shows the averaged diffractograms from different locations along the screw. The head, middle, and bottom of the 8-week corroded samples were selected for analysis due to large presence of degradation products. The differences in diffractograms taken at the head and bottom of the screw are negligible. However, there is a significant increase of $Mg(OH)_2$ peaks in the middle section where most degradation products settled within the cannulation. Moreover, most of the diffractograms demonstrated a strong amorphous signal with a peak at 0.55 $Å^{-1}$. Other identified degradation products ($MgCO_3$, $CaCO_3$, $MgHCO_3{\cdot}3H_2O$) did not show significant changes in intensity with time.

3.1.3. *Scanning electron microscopy and energy dispersive X-ray*

Fig. 5 shows SEM images captured with 50x magnification of the degraded WE43 screw heads of the cannulated screws over the immersion time. For comparison a non-degraded sample (0 weeks) is used as a reference. Material degradation is clearly visible with the loss of screw threads as immersion time persists. The regular and cracked degradation layer develops in the same fashion in the cannulation of the screw as on the exterior surface. A decrease in surface smoothness is noticeable as corrosion continues.

EDX was applied to identify and determine the distribution of elements throughout the degradation layer. The following elements were detected: Mg, Y, Nd, Zr, Na, Cl, K, P, O, and Ca. The elemental composition was measured as maps and is plotted as graphs of weight percentage (Fig. 6). Based on SEM and EDX results, the main composition of the degradation layer at two weeks is made of Mg and O. Y, Zr, and Nd are found to have high concentration near the top of the degradation layer and decreases to expected values near the base material. After four weeks, Mg and O remain the main components of the degradation layer with both contents above 25%. The distribution of the other elements remains constant throughout the whole degradation layer with O significantly decreasing near the base material. Results after six weeks display similar distribution of elements as seen after four weeks. About half of the degradation layer is now comprised of O. The degradation layer is thick with many visible cracks. At eight weeks, the degradation is at the highest and is spread well into the cannulation. The degradation layer consists of mainly Mg and O (25% and 50% respectively) with Mg rapidly growing as a residual material. There are no observations of smooth changes at the interface between the degradation layer and base material of the screw.

3.2. *Heating measurements during MRI examination*

Results derived from the heating measurements are summarized in Fig. 7. As corrosion time increased, a decline in maximum temperature change ΔT was observed, however, there was no apparent quantifiable correlation. The highest average temperature increase was seen at 0-weeks corrosion at 100% of the screw volume and the lowest temperature increase was observed at 3-weeks of corrosion time. The maximum RF-induced heating was measured to be $\Delta T = 1.20 \pm 0.29$ °C for the non-degraded WE43 screw and $\Delta T = 1.16 \pm 0.18$ °C for the titanium equivalent. However, no significant differences were observed.

4. Discussion

The increasing number of orthopaedic implantations continues to drive the need for post-surgery imaging to monitor bone healing and implant placement. MRI of implantation sites provides excellent bone-tissue contrast that may aid postoperative care of orthopaedic implants. Careful risk assessment of RF induced heating of conducting implants is mandatory before MRI can be applied for monitoring of implantation sites. Recognizing this need and opportunity, this study adds to the literature by examining the material characteristics, corrosion dynamics, and the influence of the degradation layer on RF-induced heating of Mg-based implants.

Unlike standard titanium and stainless-steel material, Mg-based implants degrade over time when exposed to bodily fluid. As a result, the chemical composition of the implant and physical geometry change as healing occurs. Since material composition and implant form influence the RF-heating of metallic implants, our study used various imaging techniques to characterise *in vitro* corroded WE43 screws. It is noted that the *in vitro* degradation technique employed in this investigation

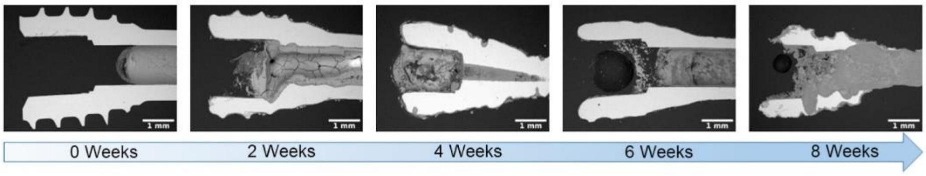

Fig. 5. SEM images of the WE43 screw heads after several time points of *in vitro* immersion.

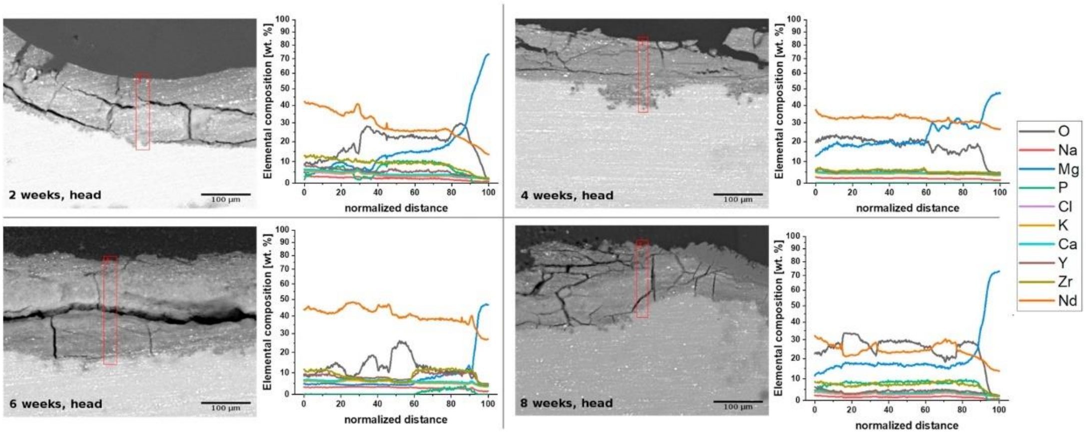

Fig. 6. Regions of interest measured EDX maps and graphs of weight percentage depending on normalized distance where 0 is the sample surface and 100 is the residual metal. Results of samples after 2, 4, 6 and 8 weeks of *in vitro* immersion.

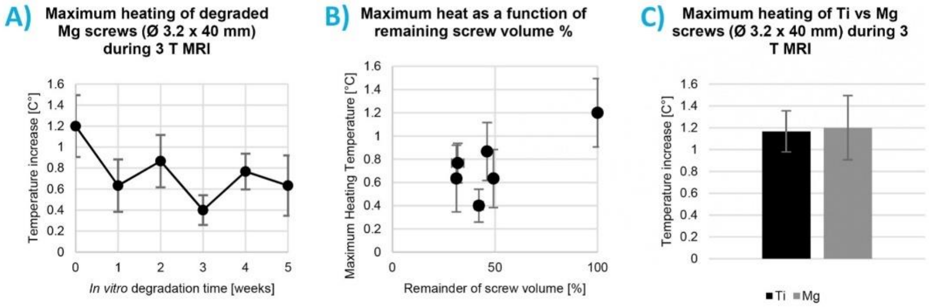

Fig. 7. Maximum RF-induced temperature heating at the tip of the screws of different length. A: influence of corrosion time on heating. B: maximum heating as a function of remainder screw volume. C: Comparison of Mg to commercial Ti equivalent.

provides only a partial impression of the complex processes in which degradation occurs in the human body, because our *in vitro* approach does not factor in the influence of biological material or cell adhesion [40].

The results derived from µCT and SEM provide insight into the physical corrosion of the screw structure *in vitro,* which is supported by previous literature [40]. The segmented µCT images reveal a statistically significant reduction in base metallic WE43 material surrounded by degradation layer as weeks progress. The non-uniformity of degradation is apparent with pit formations of various sizes. SEM images depict surface cracking of the irregular degradation layer. Additionally, the loss of threads is apparent in both µCT and SEM images as the original screw shape begins to lose definition and transforms into a tube-like structure over time. The pitting behaviour seen in Figs. 3 and 5 causes a non-uniform degradation layer and a buildup of degradation product found in the canulation of the screw.

XRD findings identified different crystalline degradation products along various locations of the screw in Fig. 4. The main degradation products were found to be $Mg(OH)_2$ and MgO, which correlates with published papers [41–44]. At eight weeks of degradation, a strong amorphous signal is visible in the middle of the screw, originating from the cannulation which is confirmed by µCT. The presence of this signal suggests the degradation products found in the middle of the screw may possess a non-crystalline amorphous phase, which may be contributed by phosphorus and calcium components [45]. Additionally, a strong Mg $(OH)_2$ signal increases over time and may be the main precipitant in the cannulation of the screw. The lower signals analysed at both ends of the screw suggest a lower presence of degradation material. Thus, the degradation material is mostly composed of $Mg(OH)_2$ in both crystalline and amorphous forms, which is supported by previous works [40].

The EDX analysis revealed high contents of Mg and O as main composition of the degradation layer, confirming degradation products identified in the XRD results. As time persists, O is determined to take further composition of the degradation material. Interestingly, Zr and the rare-earth elements Nd and Y were found to have high concentrations near the surface of the degradation layer, decreasing towards the base material. This "sticking" of rare-earth elements to the surface of the degradation layer is caused by mobility of Yttrium [46]. EDX results suggest compounds consisting of the rare-earth elements are situated near the surface of the samples. Though undetected by XRD in this investigation, previous *in vitro* studies show the identification of Y_2O_3, $Mg_{24}Y_5$, and $Mg_{24}Nd_5$ [47,48].

RF induced heating of conducting implants is influenced by a material's electromagnetic properties and by the physical geometry. Elevated heating is expected at implant lengths half to a quarter of 3.0 T RF wavelengths (13–6.5 cm in tissue) in the body [10], which is not relevant for the 40 mm length implants investigated in this experiment. Since heating is dependent on implant length and main magnetic field strength, the measured temperatures of the selected 40 mm length screws analysed in this investigation may not be representative for all degradable systems. Moreover, the reported material temperature increases of approximately 1 °C is well under the threshold in which thermal necrosis may occur at 47 °C [49]. Though there were no significant differences between the materials, the non-degraded WE43 implant yielded a minor increase in RF heating over the titanium equivalent (Fig. 7). Winter et al. simulated the secondary E-field distribution of a linear implant while varying the conductivity of the material [10]. The scattered secondary field was found to create hotspots at the implant tips as the conductivity of the material increased. As such, WE43 is reported to have a higher conductivity than titanium [50], which may justify the marginally elevated heating measured. However, Capek et al. have investigated the assumption that current distribution on perfect electric conductors and good conductors (such as copper, aluminum, and silver) are equal [51]. Therefore, similar heating profiles between WE43 materials and titanium are not expected to be significantly different as noted in Fig. 7.

As degradation occurs, not only does the physical geometry of the WE43-based screws change, but the material composition of the implant surface alters as well. As a result, the heating profile of the implant changes as the material corrodes. Our results in Fig. 7 demonstrate that the maximum heating exists at the earliest stage prior to corrosion, more specifically, highest heating at original and largest metallic volume prior to degradation, which is supported by previous work [31]. Although there are no significant differences highlighted, the maximum temperature change found for the degraded implants decreases with degradation time. As corrosion persists two complimentary processes occur, (1) the degradation layer continues to develop as (2) the base metallic material reduces.

The base metallic WE43 material degrades over time transforming the compression screw geometry into a potential one-dimensional or wire-like structure. There is minimal reduction in screw length as the implant degrades. The overall diameter of the base material of WE43 decreases during corrosion. Previous investigations demonstrated that maximum temperature rises caused by RF-heating of thin wires during MRI studies increase as diameter decreases [52]. Armenean et al. describe that the increase in temperature due to the wire diameter reduction is caused by an increased secondary E-field. Subsequently, an increased secondary E-field is developed onto the neighbouring tissue or material. Nonetheless, this finding is not in accordance with the temperature changes observed by our study. This indicates that the developing degradation layer may play a greater influence in the heating profile of Mg-based materials.

As verified by the XRD and EDX results, the $Mg(OH)_2$ layer along with other non-crystalline products continue to develop during degradation and coats the surface of the implant. The physical nature of the degradation layer and its electromagnetic properties influence the heating profile of the corroded screws twofold. First, the induced secondary E-field sensed by the conductive tissue may be dampened by the poorly conductive nature inherent to $Mg(OH)_2$ surrounding the base metallic material. Second, the physical corrosion resulting in a non-smooth surface of the material may disrupt the development of the secondary E-field. Our results demonstrate various sizes of pitting formation and developed surface roughness within the cannulation and on the surface of the screw. The overall surface smoothness is decreased as corrosion persists, which has shown to decrease the “skin effect” of EM fields and therefore reduce current density at the surface of the material [53–55]. Additionally, the secondary E-field may further be hindered by the anisotropic nature of the amorphous degradation material found in the cannulation and the non-uniform sticking of heavier rare-earth metallic elements on the surface of the material. However, the influence of the amorphous material and rare-earth elements on the secondary E-field requires further investigation. As a result, the development of the degradation layer over time may reduce the maximum heating detected by surrounding environment.

The intrinsic degradation capability of Mg-based implants introduces limitations into this investigation. The reactive characteristic of Mg-based alloys prohibits samples from being tested more than once due to the interaction with the water-based phantom medium. As a result, multiple samples must be prepared for each time-point which ultimately differ based on the non-uniform corrosion, which may be the main contributor to the variations in recorded measurements. Additionally, WE43 samples could not be placed in the phantom for extended periods of time, as bubble formation (hydrogen gas) would occur. Although the surrounding area of the temperature probes were verified to be bubble-free prior to measurements, few millimetre-sized bubble formation was seen sparsely formed on the implant due to the corrosion process. This concern justifies an amendment to the ASTM F2182 procedures to include verified and standardised protocols to map RF-induced heating caused by biodegradable materials using MR thermometry [56]. Our investigation focuses on utilising industry *in vitro* standards and testing methodologies as a mandatory precursor to *in vivo* or clinical studies, which would provide further specific information on the impact of the degradation layer on RF induced heating of biodegradable orthopaedic screw implants during MRI. Animal studies would provide further insight on heat dissipation in live tissue and therefor should be investigated in the future. As such, it is important to note that the phantom measurements described by the ASTM standard generally provide an overestimation of the temperature increase due to the lack of blood perfusion, wet tissue convection, and blood vessel conduction effects, all of which would be found *in vivo* and in clinical situations. However, previous studies [57] have shown that although the standard implicitly assumes conservative measurements, the heating responses measured in the ASTM phantom can be greatly underestimated for certain situations which should further caution users of the standardised protocol.

Although RF-induced heating has been investigated for multiple permanent implants, future studies should include heating caused by multiple implants made of biodegradable materials. Additionally, heating profiles of broken Mg-based implants resulting in gaps between the original geometry should be investigated as this may occur *in vivo* [58] which presents further safety risks [10]. Moreover, the effects of degradation products in terms of layer depth and other degradation resultants (hydrogen evolution and pH) should similarly be assessed for influence on implant heating.

5. Conclusion

This is the first study that evaluated RF-induced heating of Mg-based orthopaedic implants during MRI. WE43 screws degraded *in vitro* for various time periods causing decreased RF-induced heating during MRI sessions as corrosion time and the formation of the degradation layer progressed. This reduction in RF-induced heating may be instigated by the decline of the “skin effect” caused by a decrease in surface smoothness during degradation layer formation. To conclude, the non-degraded WE43 sample poses the “worst-case” scenario, suggesting highest heating risk occurs directly after material implantation into the body. RF-induced heating was similar for native WE43 screws and for the titanium equivalent. Though the current ASTM standard was successfully utilised in this investigation, our findings support a revision to industry safety standards to encompass testing of conductive implanted medical devices with verified methodologies which may allow for more optimal evaluations of biodegradable materials.

Conflict of interest

Authors Kuehne and Berangi are employees of MRI.TOOLS GmbH. Author Niendorf is CEO and founder of MRI.TOOLS GmbH. Syntellix AG is a medical technology manufacturer of metallic and bio-absorbable clinical implants. Authors Espiritu and Seitz are employed as Research Associate and Director of Research and Development, respectively.

CRediT authorship contribution statement

Jonathan Espiritu: Conceptualization, Data curation, Formal analysis, Investigation, Methodology, Validation, Visualization, Writing – original draft, Writing – review & editing. **Mostafa Berangi:** Data curation, Formal analysis, Investigation, Methodology. **Hanna Cwieka:** Data curation, Formal analysis, Investigation, Visualization, Writing – original draft. **Kamila Iskhakova:** Data curation, Formal analysis, Investigation, Visualization, Writing – original draft. **Andre Kuehne:** Conceptualization, Methodology, Supervision, Writing – review & editing. **D.C. Florian Wieland:** Data curation, Methodology, Resources, Supervision. **Berit Zeller-Plumhoff:** Data curation, Methodology, Resources, Supervision. **Thoralf Niendorf:** Resources, Supervision, Writing – review & editing. **Regine Willumeit-Römer:** Funding acquisition, Project administration, Resources, Supervision, Writing – review & editing. **Jan-Marten Seitz:** Conceptualization, Funding acquisition, Project administration, Resources, Supervision, Writing – review & editing.

Declaration of Competing interest

Authors Kuehne and Berangi are employees of MRI.TOOLS GmbH. Author Niendorf is CEO and founder of MRI.TOOLS GmbH. Syntellix AG is a medical technology manufacturer of metallic and bio-absorbable clinical implants. Authors Espiritu and Seitz are employed as Research Associate and Director of Research and Development, respectively.

Acknowledgements

We would like to thank Eileen Höltje from Syntellix AG (Hannover, Germany) and Roman Leicht from MRI.TOOLS GmbH (Berlin, Germany) for their assistance with the experiments and preparation of materials. This project has received funding from the European Union's Horizon 2020 Research and Innovation Programme under the Marie Skłodowska-Curie Grant Agreement No 811226.

References

[1] A. Hall, E. Dunstan, Day case total hip arthroplasty: a safe and sustainable approach to improve satisfaction and productivity, and meet the needs of the orthopaedic population, Orthop. Traumatol. 36 (1) (2022) 14–21.

[2] N. Singh, U. Batra, K. Kumar, N. Ahuja, A. Mahapatro, Progress in bioactive surface coatings on biodegradable Mg alloys: a critical review towards clinical translation, Bioact. Mater. 19 (2023) 717–757.

[3] R.P.S. Krishnan, S. Muthusamy, H. Panchal, M. Alsoufi, A. Ibrahim, A. Elsheikh, Biodegradable magnesium metal matrix composites for biomedical implants: synthesis, mechanical performance, and corrosion behavior -A review, J. Mater. Res. Technol. 20 (2022) 650–670.

[4] Z. Ran, W. Dai, K. Xie, Y. Hao, Advances of Biodegradable Magnesium-Based Implants for," Life Research, vol. 5, 2022, p. 7, 1.

[5] J. Espiritu, M. Meier, J. Seitz, The current performance of biodegradable magnesium-based implants in magnetic resonance imaging: a review, Bioact. Mater. 6 (12) (2021) 4360–4367.

[6] J. Seitz, R. Eifler, F. Bach, H. Maier, Magnesium degradation products: effects on tissue and human metabolism, Jounral of Biomedical Materials Research 102 (10) (2013) 3744–3753.

[7] Z. Mosher, J. Sawyer, D. Kelly, MRI safety with orthopedic implants, Orthopedic Clinics 49 (4) (2018) 455–463.

[8] J. Nzenhuis, S. Park, R. Kamondetdacha, A. Amjad, F. Shellock, A. Rezai, MRI and implanted medical devices: basic interactions with an emphasis on heating, IEEE Trans. Device Mater. Reliab. 5 (3) (2005) 467–480.

[9] J. Espiritu, M. Berangi, C. Yiannakou, E. Silva, R. Francischello, A. Kuehne, T. Niendorf, S. Könneker, R. Willumeit-Romer, J. Seitz, Evaluating metallic artefact of biodegradable magnesium-based implants in magnetic resonance imaging, Bioact. Mater. 15 (2022) 382–391.

[10] L. Winter, F. Seifert, L. Zilberti, M. Murbach, B. Ittermann, MRI-Related heating of implants and devices: a review, J. Magn. Reson. Imag. 53 (6) (2020) 1646–1665.

[11] A. Arduino, U. Zanovello, J. Hand, L. Zilberti, B.R.M. Chiampi, O. Bottauscio, Heating of hip joint implants in MRI: the combined effect of RF and switched-gradient fields, Magn. Reson. Med. 85 (6) (2021) 3447–3462.

[12] R. Brühl, A. Ihlenfeld, B. Ittermann, Gradient heating of bulk metallic implants can be a safety concern in MRI, Magn. Reson. Med. 77 (5) (2017) 1739–1740.

[13] L. Winter, E. Oberacker, C. özerdem, Y. Ji, F. Knobelsdorff-Brenkenhoff, G. Weidemann, B. Ittermann, F. Seifert, T. Niendorf, On the RF heating of coronary stents at 7.0 Tesla MRI, Magn. Reson. Med. 74 (4) (2015) 999–1010.

[14] E. Oberacker, K. Paul, T. Huelnhagen, C. Oezerdem, L. Winter, A. Pohlmann, L. Boehmert, O. Stachs, J. Heufelder, A. Weber, M. Rehak, I. Seibel, T. Niendorf, Magnetic resonance safety and compatibility of tantalum markers used in proton beam therapy for intraocular tumors: a 7.0 Tesla study, Magn. Reson. Med. 78 (4) (2017) 1533–1546.

[15] K. Baker, J. Tkach, J. Nyenhuis, M. Phillips, F. Shellock, J. Gonzalez-Martinez, A. Rezai, Evaluation of specific absorption rate as a dosimeter of MRI-related implant heating, J. Magn. Reson. Imag. 20 (2) (2004) 315–320.

[16] L. Winter, B. Silemek, J. Petzold, H. Pfeiffer, W. Hoffmann, F. Seifert, B. Ittermann, Parallel transmission medical implant safety testbed: real-time mitigation of RF induced tip heating using time-domain E-field sensors, Magn. Reson. Med. 84 (6) (2020) 3468–3484.

[17] Y. Eryaman, E. Turk, C. Oto, O. Algin, E. Atalar, Reduction of the radiofrequency heating of metallic devices using a dual-drive birdcage coil, Magn. Reson. Med. 69 (3) (2012) 845–852.

[18] Y. Eryaman, B. Akin, E. Atalar, Reduction of implant RF heating through modification of transmit coil electric field, Magn. Reson. Med. 65 (5) (2011) 1305–1313.

[19] T. Bachschmidt, M. Köhler, J. Nitsler, C. Geppert, P. Jakob, M. Nittka, Polarized multichannel transmit MRI to reduce shading near metal implants, Magn. Reson. Med. 75 (1) (2016) 217–226.

[20] M. Dempsey, B. Condon, D. Handley, Investigation of the factors responsible for burns during MRI, J. Magn. Reson. Imag. 13 (4) (2001) 627–631.

[21] ASTM International, *ASTM F2182-09 Standard Test Method for Measurement of Radio* Frequency Induced Heating Near Passive Implants during Magnetic Resonance Imaging, 2010. West Conshohocken, PA.

[22] I. E. C. (IEC), EC 60601–2-33:2010+AMD1:2013+AMD2:2015, CSV: Medical Electrical Equipment — Particular Requirements for the Basic Safety and Essential Performance of Magnetic Resonance Equipment for Medical Diagnosis, 2015.

[23] I. O. f. S. (ISO), Assessment of the safety of magnetic resonance imaging for patients with an active implantable medical device, Tech Specif ISOTS (2018), 10974.

[24] R. Buchli, P. Boesiger, D. Meier, Heating effects of metallic implants by MRI examinations, Magn. Reson. Med. 7 (3) (1988) 255–261.

[25] H. Bassen, W. Kainz, G. Mendoza, T. Kellom, MRI-induced heating of selected thin wire metallic implants – laboratory and computational studies – findings and new questions raised, Minim Invasive Ther. Allied Technol. 15 (2) (2006).

[26] S. Tsutsui, T. Matsuda, K. Takeda, M. Sasaki, Y. Kubo, K. Setta, S. Fujiwara, K. Chida, K. Ogasawara, Assessment of heating on titanium alloy cerebral aneurysm clips during 7T MRI, Am. J. Neuroradiol. 43 (7) (2022) 972–977.

[27] Y.C.J. Liu, F. Shellock, W. Kainz, Computational and experimental studies of an orthopedic implant: MRI-related heating at 1.5-T/64-MHz and 3-T/128-MHz, J. Magn. Reson. Imag. 37 (2) (2012) 491–497.

[28] P. Serano, L. Angelone, H. Katnani, E. Eskandar, G. Bonmassar, A novel brain stimulation technology provides compatibility with MRI, Sci. Rep. 5 (9805) (2015).

[29] E. Mattei, M. Triventi, G. Calcagnini, F. Censi, W. Kainz, G. Mendoza, H. Bassen, P. Bartolini, Complexity of MRI induced heating on metallic leads: experimental measurements of 374 configurations, Biomed. Eng. Online 7 (11) (2008).

[30] S. Feng, R. Qiang, W. Kainz, J. Chen, A technique to evaluate MRI-induced electric fields at the ends of practical implanted lead, IEEE Trans. Microw. Theor. Tech. 63 (1) (2014) 305–313.

[31] N. Yang, F. Gong, L. Cheng, H. Lei, W. Li, Z. Sun, C. Ni, Z. Wang, Z. Liu, Biodegradable magnesium alloy with eddy thermal effect for effective and accurate magnetic hyperthermia ablation of tumors, Natl. Sci. Rev. 8 (1) (2021).

[32] AZO Materials, Magnesium elektron WE43 alloy (UNS M18430) [Online]. Available: https://www.azom.com/article.aspx?ArticleID=9279, 2013. (Accessed 7 October 2021).

[33] ASTM International, ASTM standard F3268-18a, in: Standard Guide for in Vitro Degradation Testing of Absorbable Metals, 2018. West Conshohocken, PA.

[34] J. Schindelin, I. Arganda-Carreras, E. Frise, V. Kaynig, M. Longair, T. Pietzsch, S. Preibisch, C. Rueden, S. Saalfeld, B. Schmid, J. Tinevez, D. White, V. Hartenstein, K. Eliceiri, P. Tomancak, A. Cardona, Fiji: an open-source platform for biological-image analysis, Nat. Methods 9 (2012) 676–682.

[35] I. Arganda-Carreras, V. Kaynig, C. Rueden, K. Eliceiri, J. Schindelin, A. Cardona, H. Seung, Trainable Weka Segmentation: a machine learning tool for microscopy pixel classification, Bioinformatics 33 (15) (2017) 2424–2426.

[36] N. Schell, A. King, F. Beckmann, T. Fischer, M. Müller, A. Schreyer, The high energy materials science beamline (HEMS) at PETRA III, Mater. Sci. Forum 772 (2013) 57–61.

[37] M. Basham, J. Filik, M. Wharmby, P. Chang, B. El Kassaby, M. Gerring, J. Aishima, K. Levik, B. Pulford, I. Sikharulidze, D. Sneddon, M. Webber, S. Dhesi, F. Maccherozzi, O. Svensson, S. Brockhauser, G. Naray, A. Ashton, Data analysis WorkbeNch (DAWN), J. Synchrotron Radiat. 22 (2015) 853–858.

[38] W. Nitz, A. Oppelt, W. Renz, C. Manke, M. Lenhart, J. Link, On the heating of linear conductive structures as guide wires and catheters in interventional MRI, J. Magn. Reson. Imag. 13 (1) (2001) 105–114.

[39] P. Nordbeck, F. Fidler, I. Weiss, M. Warmuth, M. Friedrich, P. Ehses, W. Geistert, O. Ritter, P. Jakob, M. Ladd, H. Quick, W. Bauer, Spatial distribution of RF-induced E-fields and implant heating in MRI, Magn. Reson. Med. 60 (2) (2008) 312–319.

[40] R. Willumeit-Römer, The interface between degradable Mg and tissue, Characterization of Biodegradable Medical Materials 71 (4) (2019) 1447–1455.

[41] M. Ascencio, M. Pekguleryuz, S. Omanovic, An investigation of the corrosion mechanisms of WE43 Mg alloy in a modified simulated body fluid solution: the influence of immersion time, Corrosion Sci. 87 (2014) 489–503.

[42] G. Galicia, N. Pebere, B. Tribollet, V. Vivier, Local and global electrochemical impedances applied to the corrosion behaviour of an AZ91 magnesium alloy, Corrosion Sci. 51 (8) (2009) 1789–1794.

[43] N. Mcintyre, C. Chen, Role of impurities on Mg surfaces under ambient exposure conditions, Corrosion Sci. 40 (10) (1998) 1697–1709.

[44] I. Marco, F. Feyerabend, R. Willumeit-Römer, O. Van der Biest, Degradation testing of Mg alloys in Dulbecco's modified eagle medium: influence of medium sterilization, Mater. Sci. Eng. C 62 (2016) 68–78.

[45] B. Zeller-Plumhoff, D. Laipple, H. Slominksa, K. Iskhakova, E. Longo, A. Hermann, S. Flenner, I. Greving, M. Storm, R. Willumeit-Römer, Evaluating the morphology of the degradation layer of pure magnesium via 3D imaging at resolutions below 40 nm, Bioact. Mater. 6 (12) (2021) 4368–4376.

[46] A. Hänzi, P. Gunde, M. Schinhammer, P. Uggowitzer, On the biodegradation performance of an Mg–Y–RE alloy with various surface conditions in simulated body fluid, Acta Biomater. 5 (1) (2009) 162–171.

[47] E. Öcal, Z. Esen, K. Aydinol, A. Dericioglu, Comparison of the short and long-term degradation behaviors of as-cast pure Mg, AZ91 and WE43 alloys, Mater. Chem. Phys. 241 (2020).

[48] D. Liu, Y. Ding, T. Guo, X. Qin, C. Guo, S. Yu, S. Lin, Influence of fine-grain and solid-solution strengthening on mechanical properties and in vitro degradation of WE43 alloy, Biomed. Mater. 9 (2014).

[49] A. Anesi, M. Di Bartolomeo, A. Pellacani, M. Feretti, F. Cavani, R. Salvatori, R. Nocini, C. Palumbo, L. Chiarini, Bone healing evaluation following different osteotomic techniques in animal models: a suitable method for clinical insights, Appl. Sci. 10 (20) (2020) 7165.

[50] MatWeb, LLC, MatWeb: Material Property Data, 1996. -2022. [Online]. Available: https://www.matweb.com/index.aspx. (Accessed 14 July 2022).

[51] M. Capek, J. Eichler, P. Hazdra, Evaluating radiation efficiency from characteristic currents, IET Microw., Antennas Propag. 9 (1) (2015) 10–15.

[52] C. Armenean, E. Perrin, M. Armenean, O. Beuf, F. Pilleul, H. Saint-Jalmes, RF-induced temperature elevation along metallic wires in clinical magnetic resonance imaging: influence of diameter and length, Magn. Reson. Med. 52 (5) (2004) 1200–1206.

[53] S. Seshadri, J. Scott, Enhancing skin-effect using surface roughening and its potential to reduce RF heating from implant leads, in: Electronics New Zealand Conference, 2017.

[54] G. Gold, K. Helmreich, A physical model for skin effect in rough surfaces, in: 7th European Microwave Integrated Circuit Conference, 2012.

[55] A. Horn, J. Reynolds, J. Rautio, Conductor profile effects on the propagation constant of microstrip transmission lines, in: IEEE MTT-S International Microwave Symposium, 2010.

[56] D. Gensler, F. Fidler, P. Ehses, M. Warmuth, R. Reiter, M. Düring, O. Ritter, M. Ladd, H. Quick, P. Jakob, W. Bauer, P. Nordbeck, MR safety: fast T 1 thermometry of the RF-induced heating of medical devices, Magn. Reson. Med. 68 (5) (2012) 1593–1599.

[57] A. Yao, M. Murbach, T. Goren, E. Zastrow, W. Kainz, N. Kuster, Induced radiofrequency fields in patients undergoing MR examinations: insights for risk assessment, Phys. Med. Biol. 66 (2021).

[58] P. Sekar, N. S, V. Desai, Recent progress in in vivo studies and clinical applications of magnesium based biodegradable implants – a review, Journal of Magnesium and Alloys 9 (4) (2021) 1147–1163.

Publication 3

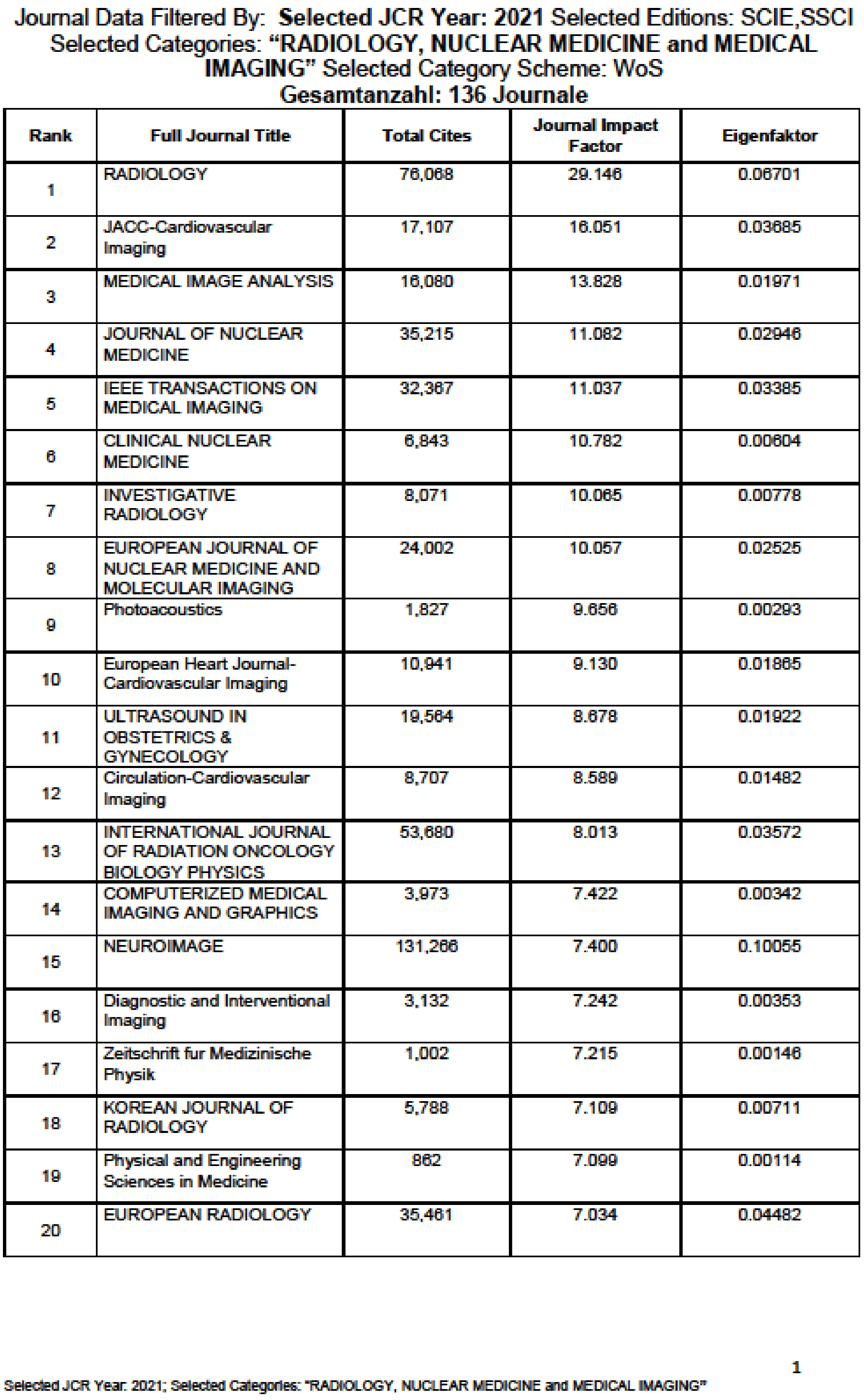

Journal Data Filtered By: **Selected JCR Year: 2021** Selected Editions: SCIE,SSCI Selected Categories: **"RADIOLOGY, NUCLEAR MEDICINE and MEDICAL IMAGING"** Selected Category Scheme: WoS
Gesamtanzahl: 136 Journale

Rank	Full Journal Title	Total Cites	Journal Impact Factor	Eigenfaktor
1	RADIOLOGY	76,068	29.146	0.06701
2	JACC-Cardiovascular Imaging	17,107	16.051	0.03685
3	MEDICAL IMAGE ANALYSIS	16,080	13.828	0.01971
4	JOURNAL OF NUCLEAR MEDICINE	35,215	11.082	0.02946
5	IEEE TRANSACTIONS ON MEDICAL IMAGING	32,367	11.037	0.03385
6	CLINICAL NUCLEAR MEDICINE	6,843	10.782	0.00604
7	INVESTIGATIVE RADIOLOGY	8,071	10.065	0.00778
8	EUROPEAN JOURNAL OF NUCLEAR MEDICINE AND MOLECULAR IMAGING	24,002	10.057	0.02525
9	Photoacoustics	1,827	9.656	0.00293
10	European Heart Journal-Cardiovascular Imaging	10,941	9.130	0.01865
11	ULTRASOUND IN OBSTETRICS & GYNECOLOGY	19,564	8.678	0.01922
12	Circulation-Cardiovascular Imaging	8,707	8.589	0.01482
13	INTERNATIONAL JOURNAL OF RADIATION ONCOLOGY BIOLOGY PHYSICS	53,680	8.013	0.03572
14	COMPUTERIZED MEDICAL IMAGING AND GRAPHICS	3,973	7.422	0.00342
15	NEUROIMAGE	131,266	7.400	0.10055
16	Diagnostic and Interventional Imaging	3,132	7.242	0.00353
17	Zeitschrift fur Medizinische Physik	1,002	7.215	0.00146
18	KOREAN JOURNAL OF RADIOLOGY	5,788	7.109	0.00711
19	Physical and Engineering Sciences in Medicine	862	7.099	0.00114
20	EUROPEAN RADIOLOGY	35,461	7.034	0.04482

1

Selected JCR Year: 2021; Selected Categories: "RADIOLOGY, NUCLEAR MEDICINE and MEDICAL IMAGING"

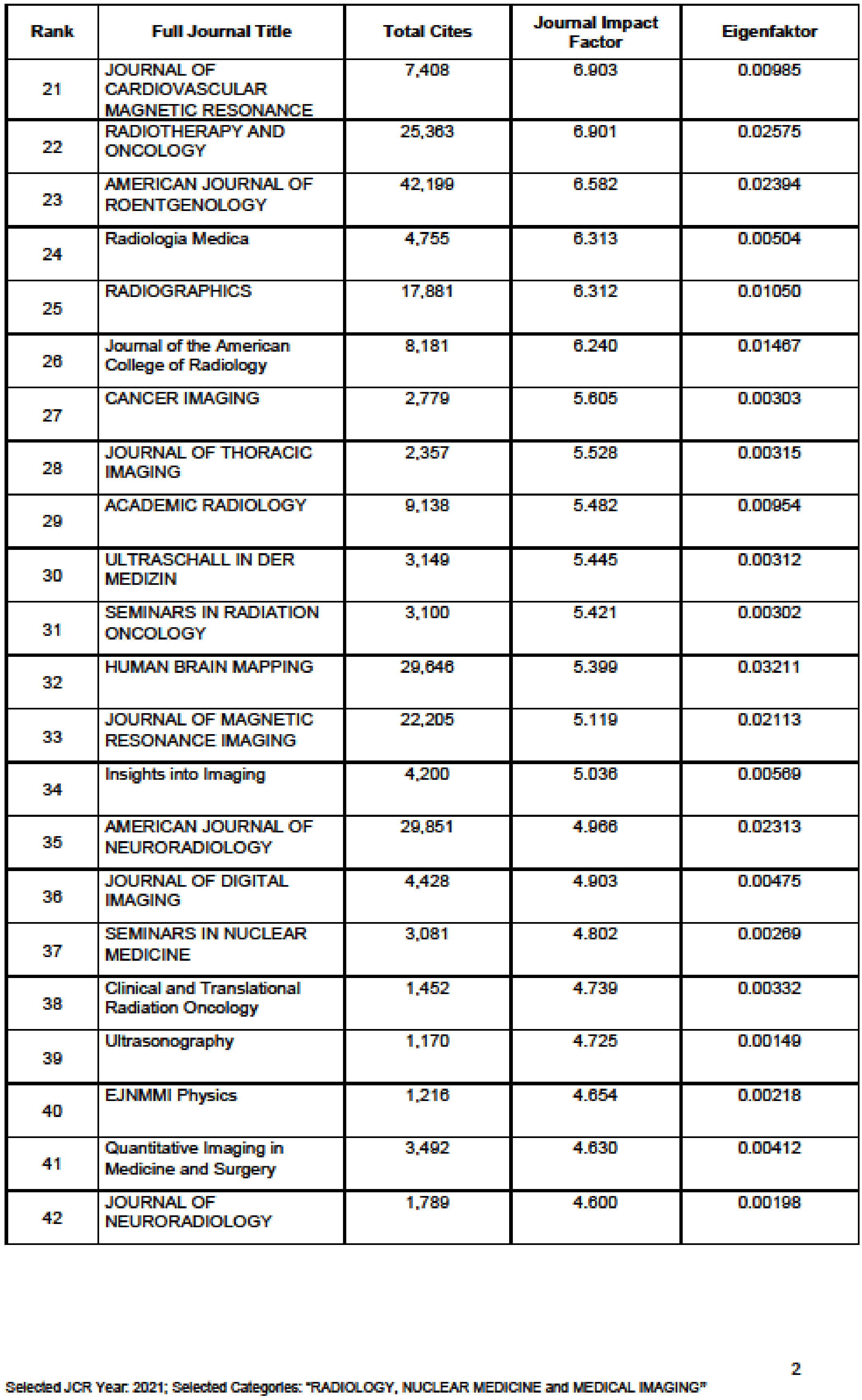

Rank	Full Journal Title	Total Cites	Journal Impact Factor	Eigenfaktor
21	JOURNAL OF CARDIOVASCULAR MAGNETIC RESONANCE	7,408	6.903	0.00985
22	RADIOTHERAPY AND ONCOLOGY	25,363	6.901	0.02575
23	AMERICAN JOURNAL OF ROENTGENOLOGY	42,199	6.582	0.02394
24	Radiologia Medica	4,755	6.313	0.00504
25	RADIOGRAPHICS	17,881	6.312	0.01050
26	Journal of the American College of Radiology	8,181	6.240	0.01467
27	CANCER IMAGING	2,779	5.605	0.00303
28	JOURNAL OF THORACIC IMAGING	2,357	5.528	0.00315
29	ACADEMIC RADIOLOGY	9,138	5.482	0.00954
30	ULTRASCHALL IN DER MEDIZIN	3,149	5.445	0.00312
31	SEMINARS IN RADIATION ONCOLOGY	3,100	5.421	0.00302
32	HUMAN BRAIN MAPPING	29,646	5.399	0.03211
33	JOURNAL OF MAGNETIC RESONANCE IMAGING	22,205	5.119	0.02113
34	Insights into Imaging	4,200	5.036	0.00569
35	AMERICAN JOURNAL OF NEURORADIOLOGY	29,851	4.966	0.02313
36	JOURNAL OF DIGITAL IMAGING	4,428	4.903	0.00475
37	SEMINARS IN NUCLEAR MEDICINE	3,081	4.802	0.00269
38	Clinical and Translational Radiation Oncology	1,452	4.739	0.00332
39	Ultrasonography	1,170	4.725	0.00149
40	EJNMMI Physics	1,216	4.654	0.00218
41	Quantitative Imaging in Medicine and Surgery	3,492	4.630	0.00412
42	JOURNAL OF NEURORADIOLOGY	1,789	4.600	0.00198

2

Selected JCR Year: 2021; Selected Categories: "RADIOLOGY, NUCLEAR MEDICINE and MEDICAL IMAGING"

Rank	Full Journal Title	Total Cites	Journal Impact Factor	Eigenfaktor
43	EUROPEAN JOURNAL OF RADIOLOGY	18,452	4.531	0.01698
44	MEDICAL PHYSICS	34,047	4.506	0.02361
45	NMR IN BIOMEDICINE	9,333	4.478	0.00940
46	Radiation Oncology	9,044	4.309	0.00986
47	Radiology and Oncology	1,530	4.214	0.00188
48	CANADIAN ASSOCIATION OF RADIOLOGISTS JOURNAL-JOURNAL DE L ASSOCIATION CANADIENNE DES RADIOLOGISTES	1,545	4.186	0.00204
49	PHYSICS IN MEDICINE AND BIOLOGY	32,475	4.174	0.02143
50	ULTRASONICS	10,209	4.062	0.00611
51	STRAHLENTHERAPIE UND ONKOLOGIE	4,084	4.033	0.00369
52	JOURNAL OF NUCLEAR CARDIOLOGY	5,958	3.872	0.00641
53	Journal of Cardiovascular Computed Tomography	2,923	3.814	0.00522
54	JOURNAL OF BIOMEDICAL OPTICS	16,255	3.758	0.01062
55	INTERNATIONAL JOURNAL OF HYPERTHERMIA	6,888	3.753	0.00511
56	MAGNETIC RESONANCE IN MEDICINE	37,122	3.737	0.02446
57	ULTRASOUND IN MEDICINE AND BIOLOGY	14,270	3.694	0.00989
58	JOURNAL OF VASCULAR AND INTERVENTIONAL RADIOLOGY	12,142	3.682	0.01042
59	CANCER BIOTHERAPY AND RADIOPHARMACEUTICALS	3,008	3.632	0.00217
60	BRITISH JOURNAL OF RADIOLOGY	14,769	3.629	0.01332
61	Biomedical Optics Express	14,709	3.562	0.02009
61	DENTOMAXILLOFACIAL RADIOLOGY	4,141	3.525	0.00254
63	MOLECULAR IMAGING AND BIOLOGY	3,794	3.484	0.00465

Selected JCR Year: 2021; Selected Categories: "RADIOLOGY, NUCLEAR MEDICINE and MEDICAL IMAGING"

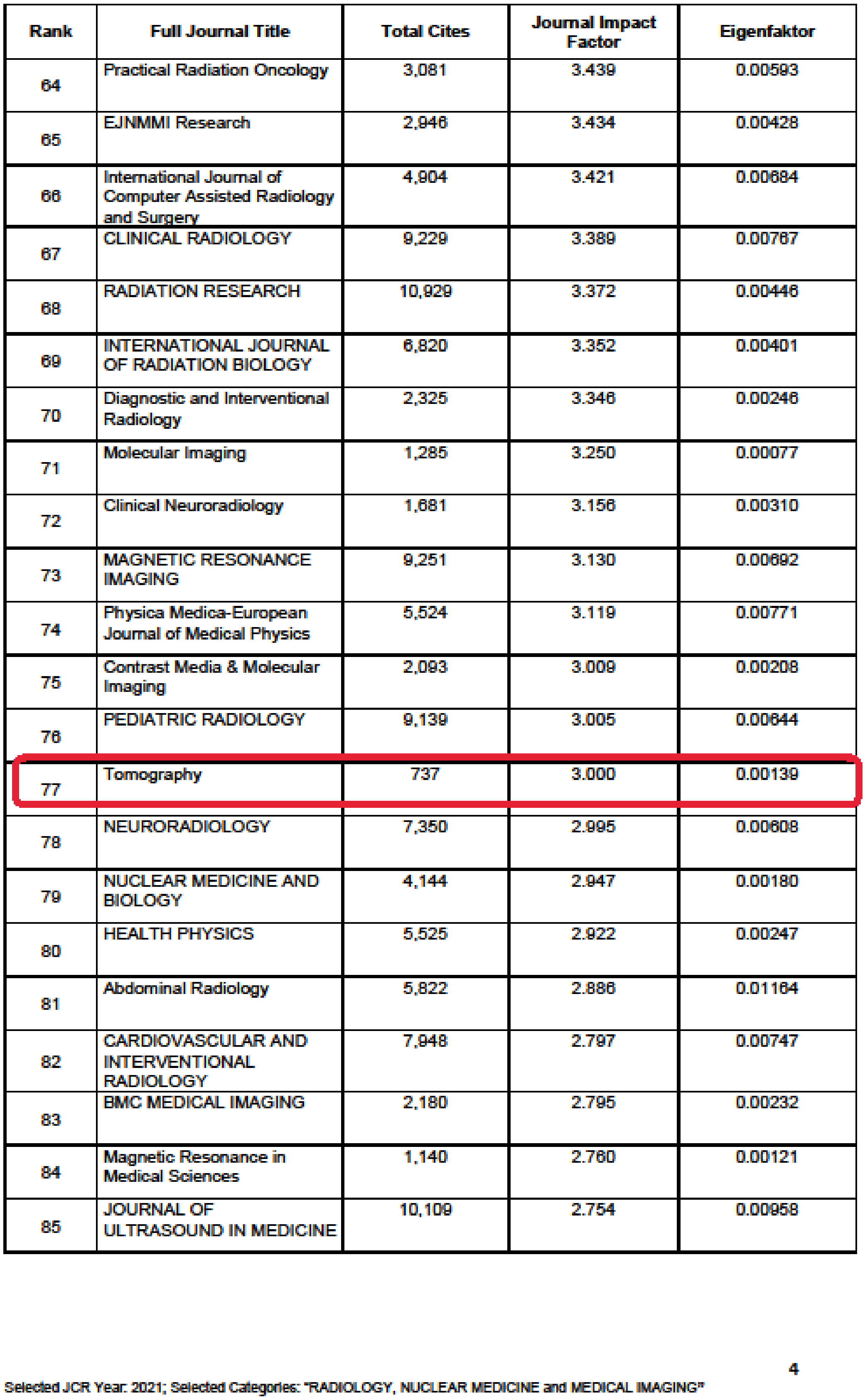

Rank	Full Journal Title	Total Cites	Journal Impact Factor	Eigenfaktor
64	Practical Radiation Oncology	3,081	3.439	0.00593
65	EJNMMI Research	2,946	3.434	0.00428
66	International Journal of Computer Assisted Radiology and Surgery	4,904	3.421	0.00684
67	CLINICAL RADIOLOGY	9,229	3.389	0.00767
68	RADIATION RESEARCH	10,929	3.372	0.00446
69	INTERNATIONAL JOURNAL OF RADIATION BIOLOGY	6,820	3.352	0.00401
70	Diagnostic and Interventional Radiology	2,325	3.346	0.00246
71	Molecular Imaging	1,285	3.250	0.00077
72	Clinical Neuroradiology	1,681	3.156	0.00310
73	MAGNETIC RESONANCE IMAGING	9,251	3.130	0.00692
74	Physica Medica-European Journal of Medical Physics	5,524	3.119	0.00771
75	Contrast Media & Molecular Imaging	2,093	3.009	0.00208
76	PEDIATRIC RADIOLOGY	9,139	3.005	0.00644
77	Tomography	737	3.000	0.00139
78	NEURORADIOLOGY	7,350	2.995	0.00608
79	NUCLEAR MEDICINE AND BIOLOGY	4,144	2.947	0.00180
80	HEALTH PHYSICS	5,525	2.922	0.00247
81	Abdominal Radiology	5,822	2.886	0.01164
82	CARDIOVASCULAR AND INTERVENTIONAL RADIOLOGY	7,948	2.797	0.00747
83	BMC MEDICAL IMAGING	2,180	2.795	0.00232
84	Magnetic Resonance in Medical Sciences	1,140	2.760	0.00121
85	JOURNAL OF ULTRASOUND IN MEDICINE	10,109	2.754	0.00958

4

Selected JCR Year: 2021; Selected Categories: "RADIOLOGY, NUCLEAR MEDICINE and MEDICAL IMAGING"

tomography

MDPI

Article

MRI of Implantation Sites Using Parallel Transmission of an Optimized Radiofrequency Excitation Vector

Mostafa Berangi [1,2,3], Andre Kuehne [3], Helmar Waiczies [3] and Thoralf Niendorf [1,2,3,*]

[1] Berlin Ultrahigh Field Facility, Max-Delbrück-Center for Molecular Medicine in the Helmholtz Association, 13125 Berlin, Germany
[2] Charité—Universitätsmedizin Berlin, 10117 Berlin, Germany
[3] MRI.TOOLS GmbH, 13125 Berlin, Germany
* Correspondence: thoralf.niendorf@mdc-berlin.de; Tel.: +49-30-9406-4505

Abstract: Postoperative care of orthopedic implants is aided by imaging to assess the healing process and the implant status. MRI of implantation sites might be compromised by radiofrequency (RF) heating and RF transmission field (B_1^+) inhomogeneities induced by electrically conducting implants. This study examines the applicability of safe and B_1^+-distortion-free MRI of implantation sites using optimized parallel RF field transmission (pTx) based on a multi-objective genetic algorithm (GA). Electromagnetic field simulations were performed for eight eight-channel RF array configurations (f = 297.2 MHz), and the most efficient array was manufactured for phantom experiments at 7.0 T. Circular polarization (CP) and orthogonal projection (OP) algorithms were applied for benchmarking the GA-based shimming. B_1^+ mapping and MR thermometry and imaging were performed using phantoms mimicking muscle containing conductive implants. The local SAR10g of the entire phantom in GA was 12% and 43.8% less than the CP and OP, respectively. Experimental temperature mapping using the CP yielded ΔT = 2.5–3.0 K, whereas the GA induced no extra heating. GA-based shimming eliminated B_1^+ artefacts at implantation sites and enabled uniform gradient-echo MRI. To conclude, parallel RF transmission with GA-based excitation vectors provides a technical foundation en route to safe and B_1^+-distortion-free MRI of implantation sites.

Keywords: MRI; implant; parallel transmission; transmission field shimming; safety; radiofrequency; RF array

check for updates

Citation: Berangi, M.; Kuehne, A.; Waiczies, H.; Niendorf, T. MRI of Implantation Sites Using Parallel Transmission of an Optimized Radiofrequency Excitation Vector. *Tomography* **2023**, *9*, 603–620. https://doi.org/10.3390/tomography9020049

Academic Editor: Emilio Quaia

Received: 26 January 2023
Revised: 3 March 2023
Accepted: 5 March 2023
Published: 8 March 2023

1. Introduction

Postoperative care of orthopedic implants is aided by the imaging of the implantation sites to monitor the healing process of surrounding bone and tissues and to assess the implant status [1,2]. For this purpose, X-ray-based imaging modalities (e.g., CT, and radiography) are commonly applied in clinical practice [3]. The use of ionizing radiation in the longitudinal examination of implantation sites adds to the cumulative radiation dose of patients, which may be associated with an increased risk of malignancy [4].

MRI presents a viable alternative for the examination of implantation sites [5–8]. The metallic and electrically conductive nature of implants constitutes a challenge for MRI [9,10]. Metallic implants may induce magnetic susceptibility dispersions at implant–tissue interfaces [11,12]. The resulting magnetic field perturbations may compromise the anatomic integrity of MRI due to distortions, may induce signal loss due to shortening of the effective transversal relaxation time T_2* or even signal voids in areas with very high B_0 gradients, or may cause off-resonance effects caused by ΔB_0-induced frequency dispersions [11]. These constraints can be addressed using on- and off-resonance approaches that permit MRI of implants free of B_0 distortions and signal voids [13–17].

Another constraint of MRI monitoring of implantation sites is related to the interactions between conductive implants and radio frequency (RF) electromagnetic fields

(EMF). These interactions lead to scattered EMFs originating from the implant [9]. The superposition of incident E-fields ($\overrightarrow{E}_{inc}$) and scattered E-fields ($\overrightarrow{E}_{sca}$) may lead to locally elevated total E-fields: $|\overrightarrow{E}_{total}| = |\overrightarrow{E}_{inc} + \overrightarrow{E}_{sca}|$. This increases the specific absorption rate (SAR) by SAR $\propto$ $|\overrightarrow{E}_{total}|^2$ and may cause RF-induced heating [18]. For example, at 7.0 T MRI the RF wavelength (λ) in brain tissue is sufficiently short (λ~12 cm) to allow for resonance and heating effects at λ/4–λ/2, which is in the size range of clinically available orthopedic implants.

The magnetic component of scattered and incident superposition fields may induce RF transmission field $\left(B_1^+\right)$ inhomogeneities. These interferences may manifest as non-uniform image intensities, signal shading, signal voids, or signal intensity elevation in the vicinity of the implant, all of which bear the potential to spoil the benefits of MRI due to non-diagnostic image quality. Owing to the shape, location, and orientation of a conductive implant, also depending on the RF excitation vector in parallel RF transmission (pTx), the level of RF-induced heating and RF transmission field distortions may vary [18,19].

A plethora of reports present MRI hardware and methodology tailored for the examination and mitigation of RF-induced implant heating and/or of RF shading near conductive implants [20–22]. A reduction in RF heating at the tip of metallic implant leads and the improvement of B_1^+ homogeneity have been demonstrated by changing the magnitude of the excitation currents on two separate channels of a dual-drive birdcage RF coil [23]. Utilizing pTx pulse design at 3.0 T to reduce SAR near a deep brain stimulation device (DBS) in a uniform flip-angle excitation scheme has been implemented and verified in simulations [24]. The impact of RF coil configurations using pTx at 3.0 T has been investigated in numerical simulations, in phantom studies, and in cadaver studies with the goal of reducing the absorbed power or of improving transmission field uniformity around DBS implants [25,26]. An optimization procedure based on a subject-dependent optimization factor has been proposed to limit SAR while providing uniform B_1^+ [27]. A more general mathematical approach has been proposed for implant-friendly MRI and was previously demonstrated in a theoretical cylindrical model [28]. However, directly translating this approach to an actual coil array is not feasible. Firstly, the desired B_1 profile and zero E-field in the implant were implemented as strict constraints in the optimization formulation. Secondly, the degrees of freedom afforded by a realistic pTx coil array are limited by the number of transmit channels. These two restrictions taken together result in a potentially unsolvable optimization problem because the constraints cannot be all simultaneously satisfied by the limited number of transmit channels. Other pioneering approaches include modification of RF transmission fields using RF arrays and parallel transmission with maximum- and null-current modes [29]. Machine-learning-based prediction of RF power absorption or ultrafast calculation of RF field enhancements near medical implants provide computational solutions for implant-specific RF heating assessment and management [30,31].

Considering the increasing population of patients with orthopedics implants [32], understanding and managing the interactions of conductive implants with RF fields is of profound importance for advancing safe and B_1^+-distortion-free MRI of implantation sites. This need concerns conventional titanium or stainless-steel-based implants and clinically available Mg-based biodegradable implants [33,34] which promote patient comfort and reduce healthcare costs by making implant removal surgery obsolete. This involves particularly small biodegradable screw or fixation implants (short implant), which are used as a real-clinical-world example in our study.

Recognizing the need for safeguarding MR monitoring of implants, this study examines the feasibility of moving towards safe and B_1^+-distortion-free MRI of implantation sites using parallel RF transmission. The main goal of our strategy is to exploit the degrees of freedom of multi-channel RF transmission using an optimized excitation vector that offsets the interactions between RF fields and a metallic implant. Our study adds to the literature because the objective of our approach of tailoring the total superposition of the RF fields is twofold: (1) to mitigate implant tip heating while keeping (local) SAR everywhere within the safety limits [35] and (2) to ensure B_1^+ homogeneity and uniform image quality in close vicinity of an implant. For this purpose, multi-channel RF array configurations comprising loop and dipole RF elements were designed and customized for 7.0 T MRI (f = 297.2 MHz) and examined in numerical EMF simulations to detail the B_1^+ E-fields and local specific absorption rates. The excitation vectors used for multi-channel transmission were derived from a multi-objective, genetic-algorithm-based optimization which demonstrates the novelty of our work. To advance from EMF simulations to a realistic clinical setup, the most efficient RF array configuration was manufactured, and its performance was assessed in phantom studies. To achieve this goal, RF transmission field mapping, MRI thermometry, and conventional MRI were performed using tissue-mimicking phantoms containing conductive implants.

2. Materials and Methods

The methods and materials used in this study are outlined in four sections:

1. The RF transceiver array configurations section introduces the design aspects and EMF simulations conducted to identify an optimum RF array configuration based on commonly used RF transceiver elements.
2. The transmission field shaping (B_1^+ shimming) section outlines the excitation vector optimization to minimize scattered fields.
3. The phantom experiments section details the setup used for validation of the EMF simulations in phantom studies conducted at 7.0 T.
4. The sections on MR thermometry and transmission field mapping describe the metrics used for validation.

2.1. RF Transceiver Array Configurations

To investigate the interference between electrically conductive implants, E-fields, and B-fields, numerical EMF simulations were performed at 297.2 MHz (operating frequency at 7.0 T MRI). A set of eight RF array configurations (Figure 1) tailored for MRI of body extremities comprising loops and/or fractionated dipoles [36] were evaluated aiming to identify the configuration with the best B_1^+ and SAR performance:

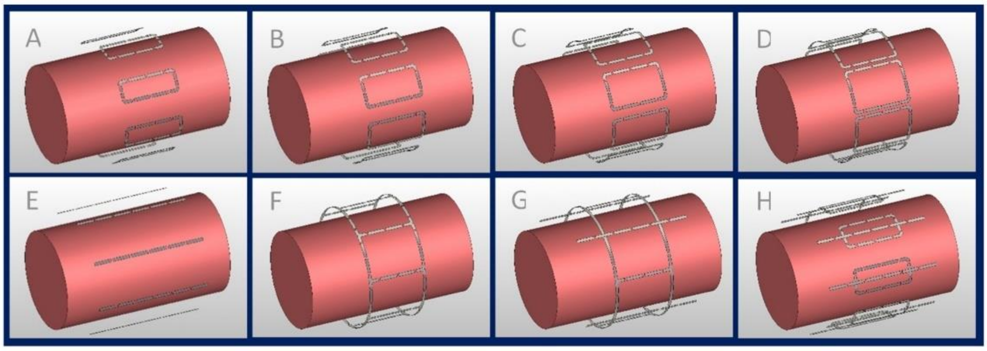

Figure 1. Eight-channel RF transceiver array configurations examined in the EMF simulations; (**A**–**D**) eight loop elements with L = 100 mm and W ≈ 41 mm, 52 mm, 62 mm, and 72 mm, (**E**) eight fractionated dipoles (L = 200 mm), (**F**) degenerate birdcage with eight rungs (L = 100 mm, D = 210 mm), (**G**) hybrid birdcage with four rungs (L = 100 mm, D = 210 mm) and four dipoles (L = 200 mm), and (**H**) loop–dipole array (L_loop = 100 mm, W_loop ≈ 41 mm, L_dipole = 200 mm).

(A–D) Eight identical loop elements (L = 100 mm) with different widths (W), defined by $W_n = ((210\text{ mm})\pi/16) \times \alpha_n$, where $n = 1$–4 and $\alpha_n = 1$, 1.25, 1.5 and 1.75.

(E) Eight fractionated dipoles (L = 200 mm, W = 5 mm).

(F) Degenerate birdcage RF resonator (L = 100 mm, D = 210 mm) using eight rungs.

(G) Combination of a degenerate birdcage RF resonator (L = 100 mm, D = 210 mm, four rungs) and four fractionated dipoles (L = 200 mm, W = 5 mm), with a fractioned dipole being placed between each birdcage rung.

(H) Eight modules consisting of a loop (L = 100 mm, $W = (210\ \text{mm})\pi/16)$ and a fractionated dipole [37,38] (L = 200 mm, W = 5 mm) placed in the center of the loop.

All RF transceivers were placed equidistantly around a cylindrical phantom (L = 300 mm, D = 170 mm) mimicking the electrical properties of muscle tissue $\varepsilon_r = 58.24$, $\sigma = 0.769$ (S/m) at 297.2 MHz. The RF transceiver arrays were placed 20 mm away from the phantom and shielded at 30 mm.

The RF array configurations were implemented in CST Studio Suite 2020 (CST MWS, Darmstadt, Germany) using the Finite Integration Technique (FIT) [39]. EMF simulations were performed with smaller than 1.5 mm^3 mesh resolution. Matching and tuning capacitors were set to force the magnitude of scattering parameters (both reflections and transmissions) of the system to less than -15 dB. Neighboring loop elements were decoupled with transformers [40]. Due to the geometric distance, no decoupling was required for the dipole elements. A cylindrical element (L = 70 mm, R = 1 mm, $\sigma = 5.8 \times 10^8$ S/m) mimicking a conducting implant was placed inside the phantom at a depth of 30 mm from the surface parallel to the phantom axis. This simulation setup was used to assess the performance of the RF arrays in terms of strength and uniformity of B_1^+ in a cylindrical ROI (L = 110 mm, R = 20 mm) covering the implant, as well as the maximum induced SAR (averaged over 10 g tissue, $\text{SAR}_{10\text{g,max}}$) in the entire phantom.

2.2. Transmission field Shaping (B_1^+ Shimming)

Transmission field shaping was performed to obtain a set of excitation vectors that met the requirements of (i) achieving a strong and uniform B_1^+ in the target ROI containing the implant and (ii) reducing the maximum local SAR below the limits imposed by the IEC guidelines [35]. This was achieved using the MATLAB (The Mathworks, Natick, MA, USA) toolbox [41] for multi-objective genetic algorithm (GA). The GA-based approach provides solutions for optimization problems with several conflicting objectives. For the field shaping problem, the output of the optimization is a set of excitation vectors that best satisfies the conflicting objectives. This set of solutions lies on a trade-off curve (pareto front) which illustrates the conflict between objectives, i.e., improving one objective results in the worsening of one or more other objectives. The following parameters were used for the definition of the objectives:

- local $\text{SAR}_{10\text{g,max}}$: the maximum 10 g SAR value in the entire phantom, not just the implantation site.
- $\text{B}_1\text{\_SAR}_{\text{max}} = \text{B}_1^+ / \sqrt{\text{local SAR}_{10\text{g,max}}}$
- $\text{COV}(\text{B}_1\text{\_SAR}_{\text{max}}) = \text{std}(\text{B}_1\text{\_SAR}_{\text{max}})/\text{mean}(\text{B}_1\text{\_SAR}_{\text{max}})$

where B_1^+ values are calculated for the target ROI containing the implant. Mean($\text{B}_1\text{\_SAR}_{\text{max}}$) is responsible for regulation of the B_1^+ strength as well as reduction in local SAR through the entire phantom. The uniformity of B_1^+ is controlled by the coefficient of variation ($\text{COV}(\text{B}_1\text{\_SAR}_{\text{max}})$). The output of this optimization is a complex excitation vector, the GA excitation vector (U_{GA}):

$$\vec{U}_{GA} = K_{GA} \times (u_1,\ u_2,\ \ldots,\ u_8) \text{ and } |u_n| = 1; 1 \leq n \leq 8,\ n \in \mathbb{N}$$

where K_{GA} is a real value constant that controls the overall excitation vector power, and u_n are complex excitation values corresponding to each RF channel.

The optimization tolerance function was set to 10^{-6} so that the algorithm remained sensitive to small $\text{SAR}_{10\text{g,max}}$ variations. Also for the optimization step, the SAR matrices were compressed using the virtual observation point [42] (VOP) approach.

The performance of the GA excitation vector to provide a strong and uniform B_1^+ pattern was benchmarked against the circular polarization (CP) mode [43]. The CP mode is a commonly used excitation vector which corresponds to a simple "Birdcage"-mode excitation used as a reference. The CP-mode vector (U_{CP}) is defined as:

$$\vec{U}_{CP} = K_{CP} \times (u_1,\ u_2,\ \ldots,\ u_8),\ u_n = \exp(-2\pi i \cdot n/8);\ 1 \le n \le 8,\ n \in \mathbb{N}.$$

where K_{CP} is a real value constant to control the overall excitation vector power, i is the imaginary unit, and u_n are complex excitation values corresponding to each RF channel.

The performance of the GA to reduce SAR_{10g} induced by the implant was benchmarked against the orthogonal projection (OP) method [22]. In the OP method, the implant-induced SAR is eliminated by projecting U_{CP} (or any other excitation vector) onto a vector perpendicular to the vector creating the worst-case implant SAR (U_{wc}). With this approach, the OP method supports elimination of the implant-induced SAR while the overall transmission field uniformity benefits from the advantages of the U_{CP} excitation.

$$\vec{U}_{OP} = \hat{U}_{CP} - \hat{U}_{wc}\ (\hat{U}_{CP}\ .\ \hat{U}_{wc}),$$

$$\hat{U}_{CP} = \frac{\vec{U}_{CP}}{\|\vec{U}_{CP}\|},\ \hat{U}_{wc} = \frac{\vec{U}_{wc}}{\|\vec{U}_{wc}\|}.$$

The U_{wc} is calculated as the eigenvector corresponding to the maximum eigenvalue of the local RF power correlation matrix in the target ROI [44].

2.3. Phantom Experiments

For validation of the EMF simulations, phantom experiments were performed at 7.0 T. Cylindrical phantoms (L = 300 mm and D = 170 mm) identical to those used in the EMF simulations were employed. A liquid-sucrose-based phantom [45] plus a solid polyvinylpyrrolidone (PVP)-based [46] phantom were used to emulate the electrical properties of muscle tissue at 297.2 MHz. The liquid-sucrose-based phantom was used for conventional MRI and B_1^+ mapping as it allows implant reorientation. Thermal experiments were conducted on the PVP phantom because there are no interfering ^{1}H resonance peaks available in the NMR spectra of PVP which elevates the accuracy of MR thermal measurements [46].

To mimic the thermal behavior of biological tissue without additional fluid dynamics caused by thermal convection, a mixture of PVP (33.9% w/w), agarose (0.4% w/w), and NaCl (1.1% w/w) was dissolved in deionized water. For the sucrose-based phantom, no gel agent was used (sucrose 48.9%w/w, NaCl 1.9% w/w). A conductivity of σ = 0.77 S/m was used to match the conductivity of muscle tissue based on the electrical properties of various body tissues for a broad frequency range [47]. The permittivity was set to ε_r = 58.

A copper wire (L = 70 mm, outer diameter D_{out} = 1 mm) mimicking an implant was placed inside the phantoms to emulate a conducting implant. The maximum implant length was chosen based on the maximum screw length of biodegradable implants commercially and clinically available today (www.syntellix.de, accessed on 1 March 2022). This approach provides a reasonable approximation of an implant because the induced current distribution on a metallic implant is the source of scattered fields which is less sensitive to the shape details [48] and metal characteristics [49]. Acrylic glass (PMMA) material was used as a phantom container. The implant was suspended in the phantom using cotton strings to minimize unwanted interference with EMFs. The strings were fixated with a 3D-printed setup made of Acrylonitrile Butadiene Styrene material to facilitate rapid and accurate positioning of the implant (Figure 2).

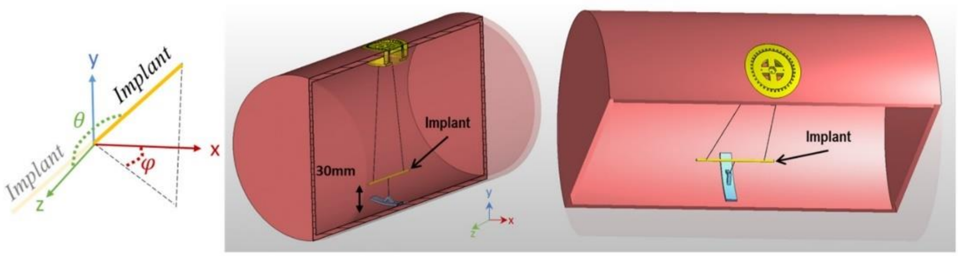

Figure 2. Cross section of the phantom and implant positioning system. The implant is suspended using cotton strings at a 30 mm distance from the phantom surface. The orientation of the implant can be controlled by adjusting the length of the strings and the rotation of the yellow implant adjuster positioned at the surface of the phantom. The orientations are defined based on a spherical coordinate system using polar (θ) and azimuthal (ϕ) angles when the origin is aligned with the center of the implant.

2.4. MR Thermometry

Implant-induced heating of GA- and CP-based excitation vectors was assessed by MR thermometry on the PVP phantom. MR thermometry was performed at the iso-center of the MRI scanner at room temperature (T = 297 K). Temperature difference maps were obtained using gradient-echo imaging (spatial resolution = 1.3 × 1.3 × 5.0 mm^3, TE_1 = 2.26 ms, TE_2 = 6.34 ms, TR = 246 ms) in conjunction with the proton resonance frequency shift approach [50] before and after RF-induced heating. An additional oil sample was used within the field of view to compensate for the magnetic field drift [51]. For the RF heating paradigm (P_{in} = 175 W, duration = 5 min), a turbo-spin-echo technique was applied.

2.5. Transmission Field Mapping

The transmission field shimming methods were evaluated using low flip angle gradient echo imaging-based [52,53] B_1^+ mapping (TR = 10 s, TE = 2.31 ms, number of averages = 4, matrix size = 256 × 256, slice thickness = 5 mm) of transversal ($\text{FOV}_{\text{transversal}}$ = 200 mm × 200 mm) and sagittal ($\text{FOV}_{\text{sagittal}}$ = 250 mm × 250 mm) slices through the center of the implant which was aligned with the center of the phantom. This procedure was used for the worst-case scenario orientation, where the implant is aligned parallel to the main magnetic field B_0 and parallel to the E-field lines of the RF arrays, thus ensuring maximum RF coupling between the E-field and the implant. The non-gel sucrose-based phantom, which enables convenient rotation of the implant, was used for B_1^+ mapping of a broad range of implant orientations.

Discrepancies in EMF patterns between the simulations and the experimental measurements may be due to losses or phase shifts which are introduced because of non-ideal real-world lumped elements, coupling of RF channels to the surroundings, and other factors. Small variations may accumulate and lead to a detectable effect on the RF field pattern. This is especially important in the close vicinity of the implant where the EMFs undergo significant alterations. Having exact information on the behavior of the EMFs in this region is important to suppress the implant-induced effects. These discrepancies were minimized in a calibration step including a simulated B_1^+ map ($\text{B}_{1,s}^+$) and its corresponding experimental map ($\text{B}_{1,e}^+$) for a slice close to the tip of the implant. This target slice can be selected in such a way that no interference from the implant is observed, or alternatively a slice-including implant can be selected if any invalid data in the implantation regions are masked. Then, complex calibrating coefficients were calculated to minimize the differences between measured and simulated B_1^+ maps in an optimization algorithm with the following error function:

$$\min_X \left\| \left(X * X_e * \text{B}_{1,s}^+ \right) - \left(X_e * \text{B}_{1,e}^+ \right) \right\|$$

where $B^{+}_{1,s}$ and $B^{+}_{1,\,e}$ are $n \times m$ complex matrixes. X is the optimization variable (calibration coefficients), and X_e is the excitation vector used to acquire $B^{+}_{1,\,e}$. X and X_e are $1 \times n$ complex vectors, n is the number of channels in the array, and m is the total number of pixels in $B^{+}_{1,\,e}$. These calibration coefficients are then multiplied by the excitation vectors obtained from the simulations to calculate the excitation vector used for the MRI experiments.

The efficacy of the GA shimming approach was investigated for several scenarios by changing the orientation of the implant. Different orientations were defined using a spherical coordinate system where the origin of the coordinate system is aligned with the center of the implant, and θ and φ are azimuthal and polar angles, respectively. The results obtained for the GA approach were benchmarked against the CP and the OP reference methods.

2.6. MR Hardware

The simulated values of the tuning and matching network were used as an initial starting point and adjusted to reach −15 dB for all scattering parameters (both reflections and transmissions) in the manufactured RF transceiver array. For phantom experiments, the RF transceiver was connected to a 7.0 T MRI scanner (Magnetom, Siemens, Erlangen, Germany) using a multi-channel interface (MRI.TOOLS GmbH, Berlin, Germany) containing transmit–receive switches and RF power dividers. The scanner was driven in pTx mode with precise control of the phase and amplitude for each of the eight RF channels.

3. Results

3.1. EMF Simulations of Eight-Channel RF Transceiver Configurations

The performance of the eight RF transceiver array configurations was assessed using the CP-mode, OP, and GA-derived transmission field shimming. The safety of each excitation is limited by the local SAR_{max}. The strength and uniformity of each excitation vector in the target ROI was assessed by the mean($B_1\_SAR_{max}$) and coefficient of variation (COV($B_1\_SAR_{max}$)). The results obtained from the EMF simulations demonstrate that with GA-based shimming, the mean($B_1\_SAR_{max}$) is increased from configuration A to E and from F to H (Figure 3A). The mean($B_1\_SAR_{max}$) across all configurations for GA, CP, and OP is $0.42 \pm 43\% \left(\mu T/\sqrt{w/kg}\right)$, $0.44 \pm 9.4\% \left(\mu T/\sqrt{w/kg}\right)$, and $0.22 \pm 21\% \left(\mu T/\sqrt{w/kg}\right)$, respectively.

Increasing the width of the loop elements used in configurations A-D increases mean($B_1\_SAR_{max}$) for each transmission field shimming algorithm (except for the CP mode in D) (Figure 3A). The mean($B_1\_SAR_{max}$) obtained for GA versus CP transmission field shimming (%($Mean_{GA}/Mean_{CP} - 1$) = −3.6% (A), −9.9% (B), −10.9% (C), and 16.8% (D)) and OP versus CP transmission field shimming (%($Mean_{OP}/Mean_{CP} - 1$) = −54.6% (A), −54.1% (B), −49.8% (C), and −33.2% (D)) reveals that the OP approach is inferior to the CP and GA approaches.

For the dipole-only configuration (E) and for the eight-loop–dipole (H) configuration, the mean ($B_1\_SAR_{max}$) obtained from the GA outperforms the CP approach (%($Mean_{GA}/Mean_{CP} - 1$) = 25.3% and 37.3%) and is superior to the OP algorithm (%($Mean_{OP}/Mean_{GA} - 1$) = −74.5% and −67.8%).

For the degenerate birdcage array (F), the CP approach provided the largest mean ($B_1\_SAR_{max}$) where (%($Mean_{GA}/Mean_{CP} - 1$) = −15.6%). In configuration (G), the mean ($B_1\_SAR_{max}$) strength derived from GA yielded a small difference (%($Mean_{GA}/Mean_{CP} - 1$) = 1.6%) versus the CP algorithm, while the mean($B_1\_SAR_{max}$) obtained from the OP algorithm is much lower (%($Mean_{OP}/Mean_{CP} - 1$) = −38.7%).

Assessment of the $B_1\_SAR_{max}$ homogeneity revealed that the OP algorithm provided a transmission field uniformity similar to that obtained for the CP algorithm for all eight RF array configurations with the exception of configuration E (%($1 - COV_{OP}/COV_{CP}$) = 1.6%, 3.9%, 4.6%, −1.4%, 32.8%, 2.8%, 6.6%, 7.5%) (Figure 3B). The GA provided a substantially more uniform transmission field pattern versus the OP or the CP approach (%($1 - COV_{GA}/COV_{CP}$) = 49.7%, 51.3%, 50.1%, 37.2, 66.6%, 64.1%, 60.8%, 75.9%) (Figure 3B).

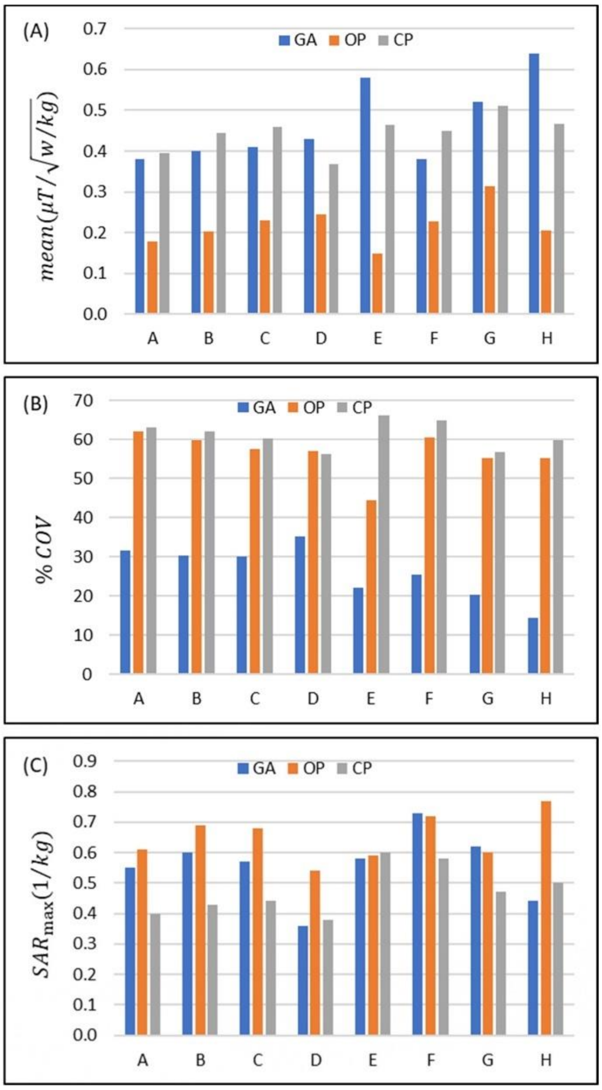

Figure 3. Comparison of the performance of the eight eight-channel RF transceiver configurations (design A to H) using a circular polarization (CP)-, an orthogonal projection (OP)-, and a multi-objective genetic algorithm (GA)-based approach for transmission field shimming. (**A**) Mean(B_1_SAR_{max}) and (**B**) %COV(B_1_SAR_{max}) in the ROI. (**C**) $SAR_{10g,max}$ in the whole phantom.

Assessment of the RF power deposition showed that average $SAR_{10g,max}$ (1 W input power) was below 0.8 (W/kg) for all RF transceiver array configurations and RF transmission field shaping approaches (Figure 3C). For most of the eight RF transceiver configurations, CP provided a lower SAR than GA or OP. The SAR obtained for the GA approach was similar to that of the OP algorithm or less. The maximum $SAR_{10g,max}$ derived from the GA approach for the loop–dipole (H) configuration was 12% and 43.8% less than the CP and OP counterparts.

The implant-induced hot SAR spots resulting from the CP mode were eliminated with the OP algorithm. Yet, our simulations showed that in some scenarios OP excitation vectors produced a superficial $\mathrm{SAR}_{10g,max}$ value that is outside of the implantation site, and thus its maximum $\mathrm{SAR}_{10g,max}$ is still in the range of the results derived from the CP mode.

Using the GA for transmission field shimming, the eight-loop–dipole configuration (H) yielded a 15.8% increase in $\mathrm{SAR}_{10g,max}$ versus the lowest SAR value among all configurations/shimming (available in configuration D with CP shimming). On the other hand, this increased $\mathrm{SAR}_{10g,max}$ is compensated for by providing the strongest mean($\mathrm{B_1\_SAR_{max}}$) among all configurations/shimming (25% more than the second strongest mean($\mathrm{B_1\_SAR_{max}}$); in configuration F with CP) and the most uniform $\mathrm{B_1\_SAR_{max}}$ excitation pattern (COV% is 67.6% lower than the lowest COV% found for the OP algorithm in design G) in the target ROI containing the implant.

3.2. Phantom MR Experiments

Based on the EMF simulations, the eight-loop–dipole configuration (H) was selected for manufacturing an RF transceiver array for use in phantom experiments. The computer-aided design and a photo of the manufactured prototype of configuration H, along with the phantom container and power splitters used for feeding the RF array, are shown in Figure 4.

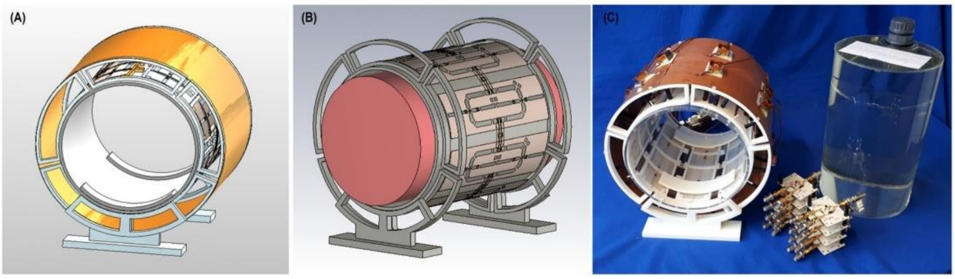

Figure 4. Experimental setup of the 8-channel loop–dipole RF transceiver array. (**A**,**B**) Computer-aided design of the RF transceiver array and the loop–dipole configuration decoupled with transformers. (**C**) Manufactured 8-channel loop–dipole RF transceiver array together with the phantom, the implant, the phantom container, and the power splitters used for RF feeding of the array.

For this configuration, the efficiency of the GA-based shimming method versus the CP and OP approaches was examined using the PVP-based gel phantom. The implant was aligned with the long axis of the phantom as the E-field lines of the RF array are along this orientation, hence inducing the most implant SAR. The metrics investigated were B_1^+ $\left(\mu\mathrm{T}/\sqrt{\mathrm{kW}}\right)$ strength and uniformity (mean and COV% of $B_1^+/\sqrt{P_{fwd.}}$, respectively, where $P_{fwd.}$ is the sum of the input power to all RF channels).

The experimental B_1^+ mapping results along with the corresponding B_1^+ maps obtained from the EMF simulations are shown in Figure 5 with the ROI containing the implant highlighted in red. The B_1^+ maps derived from the EMF simulations and the phantom experiments show good agreement. The simulated B_1^+ maps highlight that the CP approach suffers from a B_1^+ asymmetry around the implant, which manifests as a strong B_1^+ void on one side of the implant and a B_1^+ elevation on the opposite side. This asymmetry is reduced when using the OP algorithm. This improvement comes at the cost of B_1^+ destruction close to the implant. Unlike the CP and OP approaches, the transmission field vector obtained from the GA provides a uniform and increased B_1^+ field in the target ROI containing the implant.

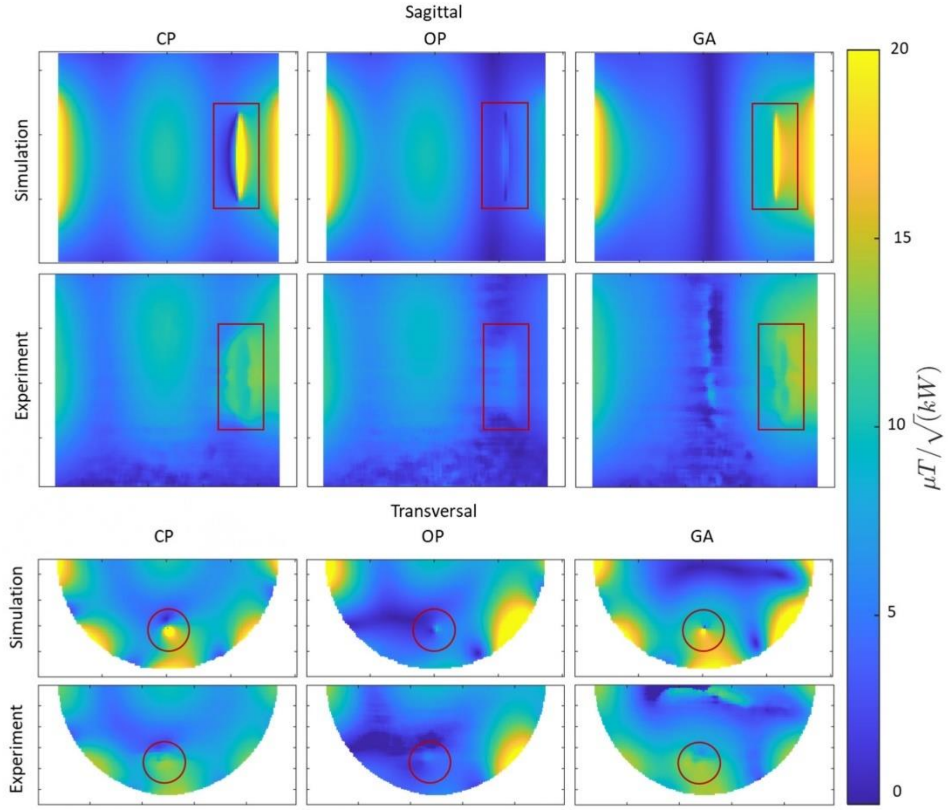

Figure 5. Simulated and experimental results obtained for B_1^+ mapping using CP-, OP-, and GA-based transmission field shimming algorithms. The top two rows show sagittal B_1^+ maps (covering the entire implant including tips). The bottom two rows show transversal B_1^+ maps (covering the regions with most pronounced RF distortion) derived from simulations and phantom experiments. The ROI containing the implant is indicated in red.

Next, the SAR reduction of the GA approach was investigated and benchmarked against the CP approach. Point SAR and temperature difference maps were derived from EMF simulations and from phantom experiments. The OP mode was not considered for heating evaluations due to its weak and non-uniform B_1^+ in the close vicinity of the implant. The point SAR distribution obtained from the EMF simulations shows a pattern similar to the E-field distribution, given that SAR is proportional to E^2. When the implant was positioned parallel to B_0, a dipole antenna effect was observed for SAR near the tips of the copper wire. This is due the accumulation of charges at the tips of the implant causing elevated SAR in the close vicinity of the implant. The movement of these charges on the surface of the implant (i.e., induced currents) is responsible for B_1^+ inhomogeneities. The SAR obtained for the GA-based transmission field shimming is substantially reduced compared to that of the CP mode, meaning that less current is induced on the implant with the GA approach (Figure 6). This SAR reduction is achieved by creating a reduced E-field in the vicinity of the implant.

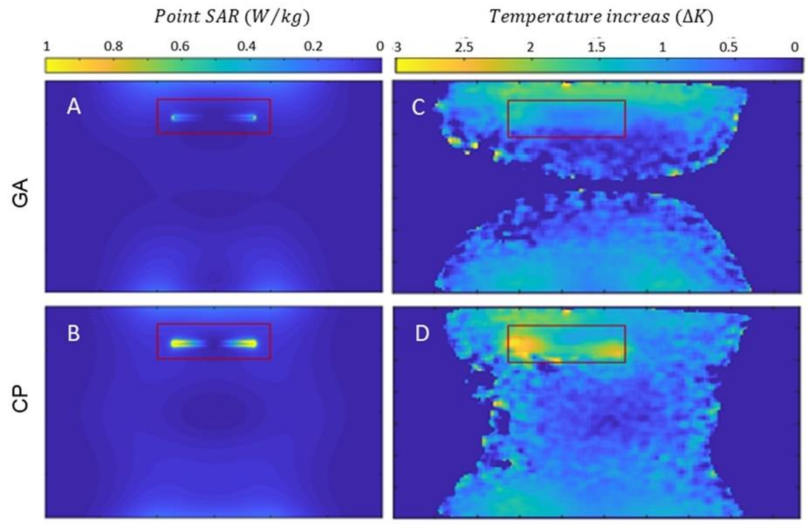

Figure 6. Simulation of point SAR maps (projection of maximum value) for a sagittal view of the phantom using GA- (**A**) and CP-based (**B**) transmission field shimming for 1 W input power along with temperature increase maps obtained for a sagittal view using GA- (**C**) and CP-based (**D**) shimming. The ROI containing the implant is indicated in red.

Temperature difference maps (Figure 6) derived from MR thermometry confirmed the results obtained from the SAR assessment. The transmission field vectors obtained for the CP approach induced a temperature increase of ΔT = 2.5–3.0 K at the tips of the implant. The GA approach resulted in transmission fields which induced no extra temperature increase around the implant (Figure 6). With the GA approach, the area around the implant showed a temperature which did not differ from the background temperature distribution. A summary of the metrics obtained from the EMF simulations and the phantom experiments is shown in Table 1.

Table 1. Summary of statistical B_1^+ parameters and maximum temperature increase derived from numerical EMF simulations and phantom experiments using the CP, OP, and GA approaches for transmission field shaping.

Transmission Field Shaping Algorithm	**EMF Simulation**			**Experiment**		
	$mean\ (B_1^+)$ $(\mu T/\sqrt{kW})$	$\%\ \frac{std.(B_1^+)}{mean(B_1^+)}$	$max.\ \Delta K$	$mean\ (B_1^+)$ $(\mu T/\sqrt{kW})$	$\%\ \frac{std.(B_1^+)}{mean(B_1^+)}$	$max.\ \Delta K$
CP	7.6	51.4%	3.27 K	7.3	53%	3.15 K
OP	3.2	53.2%	–	2.3	69%	-
GA	10.3	23.2%	1.31 K	9.6	23%	1.23 K

The simulated and measured B_1^+ maps and their corresponding point SAR and temperature difference maps obtained with the GA excitation vector demonstrated that a reduction in SAR is related to the homogenization of the B_1^+ field in the vicinity of the implant. This can be explained by the fact that both unwanted effects originate from the same source, namely induced currents on the conductive implant. Thus, the reduction in SAR is related to the homogenization of the B_1^+ field and vice versa.

Next, the orientation of the implant was varied, and the B_1^+ maps measured, relative to the reference position (the implant was aligned with the long axis of the phantom). For convenient repositioning of the implant, the liquid-sucrose-based phantom was used.

The implant orientations were defined using spherical coordinates where the origin was placed at the center of the implant, and polar (θ) and azimuthal (φ) angles defined the orientation. The transversal maps were acquired for slices through the center of the implant, where the implant-induced inhomogeneity of B_1^+ reaches a maximum. A summary of the B_1^+ maps obtained for the CP-, OP-, and GA-based shimming algorithms is shown in Figure 7A(A–R). For an orientation of $\theta = 90°$ and $\varphi = 0°$, the implant-induced B_1^+ artefact reached a minimum (Figure 7A(J–L)). For this orientation, a minimal current is induced on the implant because the E-Fields of the RF transceiver array are almost parallel to the long axis of the RF transceiver. Other implant orientations revealed strong B_1^+ inhomogeneities in the vicinity of the implant for transmission field shimming using the CP or OP algorithm. The GA supported substantial improvements in the B_1^+ uniformity. For every implant orientation, GA transmission field shimming provided a combined mean B_1^+ and B_1^+ uniformity which was superior to the counterparts derived from CP and OP transmission field shimming.

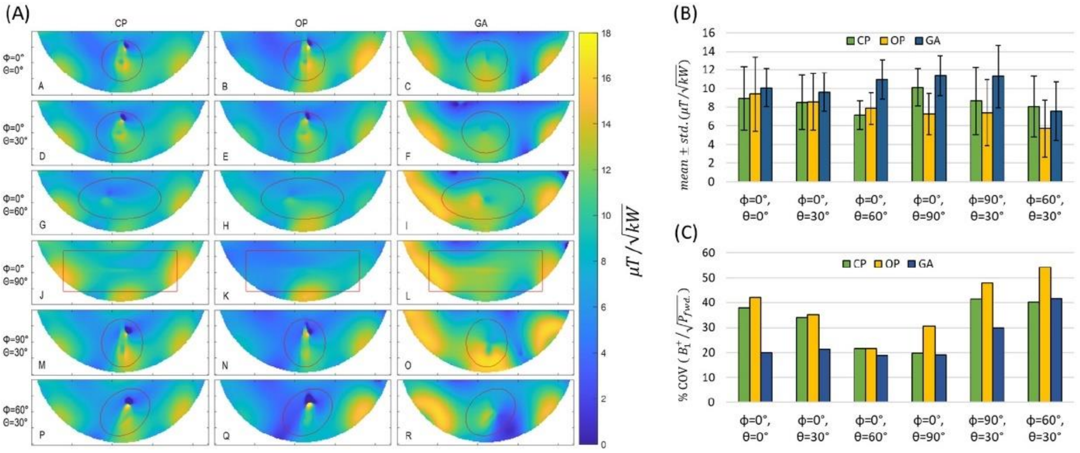

Figure 7. (**A**) Transversal experimental B_1^+ maps obtained for the tissue-mimicking phantom using CP-, OP-, and GA-based transmission field shimming for several implant orientations (Labelled from A to R). The implant orientation is defined using polar (θ) and azimuthal (φ) angles in spherical coordinates by considering the origin of the coordinate system on the center of the implant. The ROI covering the phantom is indicated in red. (**B**) Mean ± std. and (**C**) % coefficient of variation in $\left(B_1^+\right)/\sqrt{power_{Fwd.}}$ inside the ROI for different implant orientations (defined with polar (θ) and azimuthal (φ) angles with the origin of the coordinate system being placed on the center of the implant) using CP, OP, and GA transmission field shimming.

3.3. MRI of Implants Using a High Spatial Resolution

To examine the clinical applicability of transmission field shimming, a 3D gradient-echo MRI was performed (TR = 20 ms, TE = 2.7 ms, FA = 20°, isotropic spatial resolution = 0.5 mm^3, matrix size = 512 × 512 × 104, TA ≈ 17 min, receiver bandwidth = 501 Hz/Px) using the eight-loop–dipole configuration (H) in conjunction with the excitation vectors derived from the CP, OP, and GA approaches. From the 3D data sets, imaging planes including the implant and B_1^+ artifacts were manually selected using a custom-built MATLAB script. Minimum-intensity projection (MinIP) was used to project the 3D data in the vicinity of the implant onto 2D MinIP images (Figure 8) which help elucidate any destructive interference. For transmission field shimming using the CP and OP algorithms, a bow-shaped B_1^+ artefact is formed close to the implant. GA transmission field shimming eliminated B_1^+ artefacts and facilitated the acquisition of uniform images in the vicinity of the implant (Figure 8).

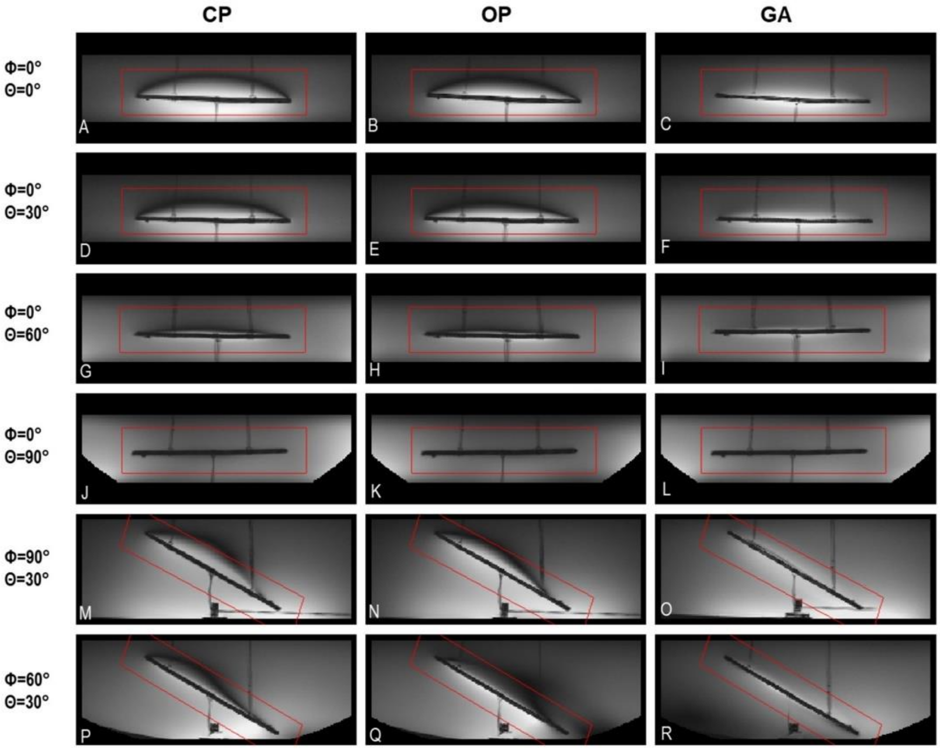

Figure 8. Minimum-intensity projections of worst-case B_1^+ artifacts obtained from 3D gradient-echo MRI in the vicinity of the implant using CP-, OP-, and GA-based transmission field shimming; (**A**–**R**) correspond to the excitation vector shown in Figure 7 for several implant orientations. The implant orientation is defined by using polar and azimuthal angles in spherical coordinates by considering the origin of the coordinate system on the center of the implant. The ROI under investigation is indicated in red.

3.4. Simulations in the Realistic Human Voxel Model

The eight-loop–dipole configuration (H) was selected for the simulation of a realistic human model (Duke [54]) with a sample screw (L = 70 mm, outer diameter D_{out} = 1 mm) implanted in the right tibia. The GA with the properties described in the section on transmission field shaping (B_1^+ shimming) was implemented for a cylindrical ROI (L = 110 mm, D = 40 mm). The CP was used for benchmarking in terms of B_1^+ strength and uniformity in the ROI and SAR reduction, and the results are presented in Figure 9.

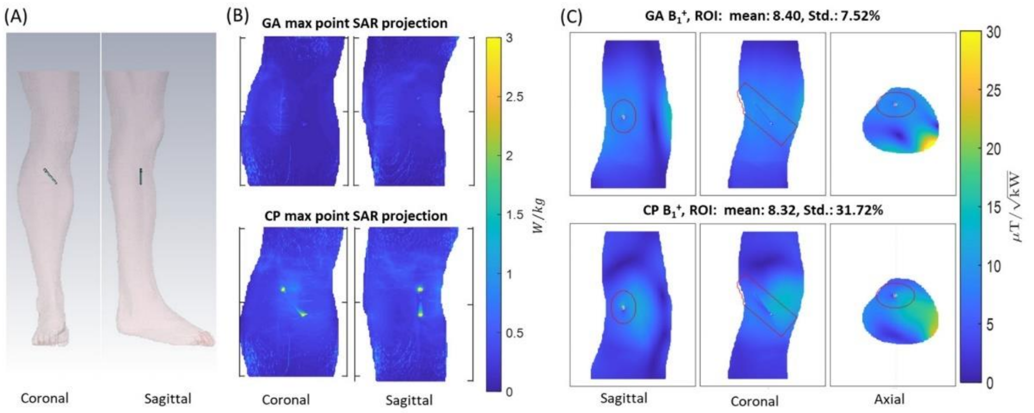

Figure 9. (**A**) Overview of the setup used for EMF simulations showing the positioning of the sample screw implant in the tibia of the human voxel model Duke. (**B**) Maximum point SAR projections obtained for the GA (**top**) and CP (**bottom**) approach for 1 W input power. (**C**) B_1^+ maps derived for slices through the center of the implant using the GA (**top**) and CP (**bottom**) approach. The ROI is highlighted in red.

4. Discussion

MRI monitoring of tissue healing and implant status may be compromised by RF-induced tissue heating and transmission field inhomogeneities. Here, we demonstrate the feasibility of moving towards safe and B_1^+-distortion-free MRI at 7.0 T in the presence of implants, using parallel radiofrequency transmission in conjunction with excitation vector optimization. Eight RF array configurations comprising loop elements and/or fractionated dipoles were characterized in EMF simulations using the metrics $\mathrm{SAR}_{10g,max}$ and transmission field strength and uniformity. The EMF simulations demonstrated that the eight-channel loop–dipole RF array configuration driven with optimum transmission field patterns obtained from a multi-objective GA provided the strongest transmission field B_1^+ and the most uniform B_1^+ distribution for a target ROI containing the implant. B_1^+ mapping, MR thermometry, and 3D gradient-echo imaging of a phantom mimicking muscle tissue showed that parallel transmission using the eight-channel loop–dipole RF array in conjunction with the multi-objective GA successfully reduces implant-induced SAR and provides transmission field uniformity required for MRI-based monitoring of tissue healing and for monitoring the degradation state of metallic implants. While our feasibility study was performed at 7.0 T, this approach can be readily applied to any available pTx system at various magnetic field strengths of 3.0 T and 1.5 T. It is also suitable for higher magnetic field strengths such as 10.5 T or 14.0 T. Using dynamic pTx versus static pTx would permit further transmission field enhancement in the presence of implants. While our clinical example used for demonstration of proof of principle focuses on screw implants used for fixation of bone fractures in body extremities, our approach can be conveniently applied to other body regions including the use of RF arrays customized for these body regions.

The CP excitation approach results in B_1^+ artifacts and excessive implant-induced SAR close to the implant. The OP method can reduce implant-induced SAR, but only at the cost of B_1^+ degradation at the implant site, resulting in non-uniform image intensity. Our results demonstrate that the GA-based approach addresses both these challenges, and thus represents a promising option en route to safe clinical MRI of orthopedic implants, free of B_1^+ artifacts. It is a recognized limitation of our study that MRI was limited to high-spatial-resolution gradient-echo imaging. Further research into other MRI techniques such as echo-planar imaging or fast-spin-echo imaging is warranted.

GA-based transmission field shimming eliminates conducting implant effects on EMFs by the suppression of RF-induced current on the implant surface. This is achieved by creating a reduced E-field region in the implantation location. Hence, it is plausible that the GA method can be adapted for shaping the transmission field around other passively conducting (interventional) devices. These include, for example, standard titanium implants, catheters, intracoronary stents, guide wires, or metallic needles. This approach is compatible with the rapid detection and mitigation of RF-induced implant heating during MRI using small (<1.5 mm^3) and low-cost (EUR < 1) root-mean-square (RMS) sensors, such as diodes and thermistors integrated within an implant [55]. Although current commercially available diodes and thermistor configurations are not yet biodegradable, continuing advances in bioderived materials, green processing, and additive manufacturing for green electronics offer a conceptually appealing strategy to pursue the development of biocompatible and biodegradable electronic devices, which can complement biodegradable orthopedic implants, allowing even more effective non-invasive monitoring [56,57].

A caveat of this feasibility study is that the number of RF transmission channels is limited to eight independent radiofrequency power amplifiers (RFPA, each 1 kW peak output power) due to the MR scanner system design used. However, recent commercially available implementations that support up to sixteen RFPAs, each providing up to 2 kW adjustable RF output power, can circumvent this limitation. Pioneering scalable prototypes supporting up to thirty-two independent signal generators, RFPAs, and RF chains suitable for parallel transmission MRI of the body at 7.0 T offer even more potential [58,59]. Parallel transmission with RF transceiver array configurations of up to 48 channels have also been evaluated in EMF simulations [60]. Thus, increasing the number of RF transmission channels will improve the degrees of freedom and will provide more flexibility for transmission field shaping. This advancement will be greatly beneficial for the suppression of induced currents on implants of arbitrary geometry or size and can potentially improve the overall performance of the approach proposed herein. Increasing the number of RF channels to cover the same region of interest requires smaller transceiver elements (due to limited space) which reduces load noise seen from each element but also introduces extra coil resistance (i.e., through more copper, lumped elements, etc.) to the total resistance seen from the RF transceiver ports [61] which constrains the signal-to-noise ratio of MRI. On the other hand, increasing the number of channels elevates the total losses in the transmission path as more cabling and circuit elements are required. Therefore, the ideal number of independent RF transmission channels used for MRI of implants will depend on the specific application, implant configuration, and target anatomy.

5. Conclusions

This study demonstrates that parallel transmission using an eight-channel loop–dipole RF array in conjunction with a multi-objective genetic algorithm for transmission field shaping ensures MR safety and transmission field uniformity suitable for MRI-aided monitoring of tissue healing of implantation sites including MRI characterization of the degradation state of biodegradable orthopedic implants. The proposed approach provides important guidance for RF coil design and provides a technological basis for MRI of orthopedic and other conducting implants at clinical magnetic field strengths. While the impact of the RF transmit array on the efficiency of GA-based excitation vector optimization is acknowledged, it stands to reason that the approach evaluated and validated in this study is compatible with any RF array with an arbitrary number of transmit channels to facilitate safe and B_1^+-distortion-free MRI of implants.

Author Contributions: Conceptualization, M.B., A.K., H.W. and T.N.; Methodology, M.B. and A.K.; Software, M.B.; Validation, M.B. and H.W.; Formal analysis, M.B.; Investigation, M.B. and H.W.; Data curation, M.B.; Writing—original draft, M.B.; Writing—review & editing, M.B., A.K., H.W. and T.N.; Visualization, M.B.; Supervision, T.N.; Project administration, A.K. and T.N. All authors have read and agreed to the published version of the manuscript.

Funding: This work received funding (M.B., A.K., T.N.) from the European Union's Horizon 2020 research and innovation program under the Marie Skłodowska-Curie grant agreement No. 811226. This project received funding (T.N.) from the European Research Council (ERC) under the European Union Horizon 2020 research and innovation program under grant agreement No. 743077 (ThermalMR).

Institutional Review Board Statement: Not applicable.

Informed Consent Statement: Not applicable.

Data Availability Statement: The code and data that support the findings of this study will be openly available in GitHub (https://github.com/BerangiMostafa/safe_MRI_of_implants, accessed on 1 April 2023) upon publication of the manuscript.

Acknowledgments: The authors wish to thank Roman Leicht, Darius Lysiak, and Alonso Vazques (MRI.TOOLS GmbH, Berlin, Germany) for assistance with the preparation and manufacturing of the experimental RF transceiver array and phantom, and Jason M. Millward (Berlin Ultrahigh Field Facility, Max-Delbrueck Center for Molecular Medicine in the Helmholtz Association, Berlin, Germany) for revision of the manuscript.

Conflicts of Interest: Mostafa Berangi and Helmar Waiczies are employees of MRI.TOOLS GmbH, Berlin, Germany. Thoralf Niendorf is founder and CEO of MRI.TOOLS GmbH, Berlin, Germany.

References

1. Espiritu, J.; Meier, M.; Seitz, J.-M. The current performance of biodegradable magnesium-based implants in magnetic resonance imaging: A review. *Bioact. Mater.* **2021**, *6*, 4360–4367. [CrossRef] [PubMed]
2. White, L.M.; Buckwalter, K.A. Technical considerations: CT and MR imaging in the postoperative orthopedic patient. *Semin. Musculoskelet. Radiol.* **2002**, *6*, 5–17. [CrossRef] [PubMed]
3. Paramitha, D.; Ulum, M.F.; Purnama, A.; Wicaksono, D.H.B.; Noviana, D.; Hermawan, H. Monitoring degradation products and metal ions in vivo. *Monit. Eval. Biomater. Perform. Vivo* **2017**, *1*, 19–44. [CrossRef]
4. Linet, M.S.; Slovis, T.L.; Miller, D.L.; Kleinerman, R.; Lee, C.; Rajaraman, P.; Berrington de Gonzalez, A. Cancer risks associated with external radiation from diagnostic imaging procedures. *CA A Cancer J. Clin.* **2012**, *62*, 75–100. [CrossRef]
5. Koch, K.M.; Brau, A.C.; Chen, W.; Gold, G.E.; Hargreaves, B.A.; Koff, M.; McKinnon, G.C.; Potter, H.G.; King, K.F. Imaging near metal with a MAVRIC-SEMAC hybrid. *Magn. Reson. Med.* **2011**, *65*, 71–82. [CrossRef]
6. Koch, K.M.; Hargreaves, B.A.; Pauly, K.B.; Chen, W.; Gold, G.E.; King, K.F. Magnetic resonance imaging near metal implants. *J. Magn. Reson. Imaging* **2010**, *32*, 773–787. [CrossRef]
7. Hayter, C.L.; Koff, M.F.; Potter, H.G. Magnetic resonance imaging of the postoperative hip. *J. Magn. Reson. Imaging* **2012**, *35*, 1013–1025. [CrossRef]
8. Jungmann, P.M.; Agten, C.A.; Pfirrmann, C.W.; Sutter, R. Advances in MRI around metal. *J. Magn. Reson. Imaging* **2017**, *46*, 972–991. [CrossRef]
9. Winter, L.; Seifert, F.; Zilberti, L.; Murbach, M.; Ittermann, B. MRI-Related Heating of Implants and Devices: A Review. *J. Magn. Reson. Imaging* **2021**, *53*, 1646–1665. [CrossRef]
10. Kuroda, K.; Yatsushiro, S. New Insights into MR Safety for Implantable Medical Devices. *Magn. Reson. Med. Sci.* **2022**, *21*, 110–131. [CrossRef]
11. Hargreaves, B.A.; Worters, P.W.; Pauly, K.B.; Pauly, J.M.; Koch, K.M.; Gold, G.E. Metal-induced artifacts in MRI. *AJR Am J Roentgenol* **2011**, *197*, 547–555. [CrossRef]
12. Spronk, T.; Kraff, O.; Kreutner, J.; Schaefers, G.; Quick, H.H. Development and evaluation of a numerical simulation approach to predict metal artifacts from passive implants in MRI. *Magn. Reson. Mater. Phys. Biol. Med.* **2022**, *35*, 485–497. [CrossRef]
13. Koch, K.M.; Lorbiecki, J.E.; Hinks, R.S.; King, K.F. A multispectral three-dimensional acquisition technique for imaging near metal implants. *Magn. Reson. Med.* **2009**, *61*, 381–390. [CrossRef] [PubMed]
14. Lu, W.; Pauly, K.B.; Gold, G.E.; Pauly, J.M.; Hargreaves, B.A. SEMAC: Slice Encoding for Metal Artifact Correction in MRI. *Magn. Reson. Med.* **2009**, *62*, 66–76. [CrossRef]
15. Cho, Z.H.; Kim, D.J.; Kim, Y.K. Total inhomogeneity correction including chemical shifts and susceptibility by view angle tilting. *Med. Phys.* **1988**, *15*, 7–11. [CrossRef]
16. Hargreaves, B.A.; Chen, W.; Lu, W.; Alley, M.T.; Gold, G.E.; Brau, A.C.S.; Pauly, J.M.; Pauly, K.B. Accelerated slice encoding for metal artifact correction. *J. Magn. Reson. Imaging JMRI* **2010**, *31*, 987–996. [CrossRef] [PubMed]
17. Chen, C.A.; Chen, W.; Goodman, S.B.; Hargreaves, B.A.; Koch, K.M.; Lu, W.; Brau, A.C.; Draper, C.E.; Delp, S.L.; Gold, G.E. New MR imaging methods for metallic implants in the knee: Artifact correction and clinical impact. *J. Magn. Reson. Imaging* **2011**, *33*, 1121–1127. [CrossRef]
18. Winter, L.; Oberacker, E.; Özerdem, C.; Ji, Y.; von Knobelsdorff-Brenkenhoff, F.; Weidemann, G.; Ittermann, B.; Seifert, F.; Niendorf, T. On the RF heating of coronary stents at 7.0 Tesla MRI. *Magn. Reson. Med.* **2015**, *74*, 999–1010. [CrossRef] [PubMed]

19. Espiritu, J.; Berangi, M.; Yiannakou, C.; Silva, E.; Francischello, R.; Kuehne, A.; Niendorf, T.; Könneker, S.; Willumeit-Römer, R.; Seitz, J.M. Evaluating metallic artefact of biodegradable magnesium-based implants in magnetic resonance imaging. *Bioact. Mater.* **2022**, *15*, 382–391. [CrossRef] [PubMed]
20. Li, D.; Zheng, J.; Liu, Y.; Pan, C.; Kainz, W.; Yang, F.; Wu, W.; Chen, J. An efficient approach to estimate MRI RF field induced in vivo heating for small medical implants. *IEEE Trans. Electromagn. Compat.* **2015**, *57*, 643–650. [CrossRef]
21. Baker, K.B.; Tkach, J.A.; Nyenhuis, J.A.; Phillips, M.; Shellock, F.G.; Gonzalez-Martinez, J.; Rezai, A.R. Evaluation of specific absorption rate as a dosimeter of MRI-related implant heating. *J. Magn. Reson. Imaging* **2004**, *20*, 315–320. [CrossRef]
22. Winter, L.; Silemek, B.; Petzold, J.; Pfeiffer, H.; Hoffmann, W.; Seifert, F.; Ittermann, B. Parallel transmission medical implant safety testbed: Real-time mitigation of RF induced tip heating using time-domain E-field sensors. *Magn. Reson. Med.* **2020**, *84*, 3468–3484. [CrossRef] [PubMed]
23. Eryaman, Y.; Turk, E.A.; Oto, C.; Algin, O.; Atalar, E. Reduction of the radiofrequency heating of metallic devices using a dual-drive birdcage coil. *Magn. Reson. Med.* **2013**, *69*, 845–852. [CrossRef] [PubMed]
24. Eryaman, Y.; Guerin, B.; Akgun, C.; Herraiz, J.L.; Martin, A.; Torrado-Carvajal, A.; Malpica, N.; Hernandez-Tamames, J.A.; Schiavi, E.; Adalsteinsson, E.; et al. Parallel transmit pulse design for patients with deep brain stimulation implants. *Magn. Reson. Med.* **2015**, *73*, 1896–1903. [CrossRef]
25. Guerin, B.; Angelone, L.M.; Dougherty, D.; Wald, L.L. Parallel transmission to reduce absorbed power around deep brain stimulation devices in MRI: Impact of number and arrangement of transmit channels. *Magn. Reson. Med.* **2020**, *83*, 299–311. [CrossRef] [PubMed]
26. Eryaman, Y.; Kobayashi, N.; Moen, S.; Aman, J.; Grant, A.; Vaughan, J.T.; Molnar, G.; Park, M.C.; Vitek, J.; Adriany, G.; et al. A simple geometric analysis method for measuring and mitigating RF induced currents on Deep Brain Stimulation leads by multichannel transmission/reception. *NeuroImage* **2019**, *184*, 658–668. [CrossRef] [PubMed]
27. McElcheran, C.E.; Golestanirad, L.; Iacono, M.I.; Wei, P.S.; Yang, B.; Anderson, K.J.T.; Bonmassar, G.; Graham, S.J. Numerical Simulations of Realistic Lead Trajectories and an Experimental Verification Support the Efficacy of Parallel Radiofrequency Transmission to Reduce Heating of Deep Brain Stimulation Implants during MRI. *Sci. Rep.* **2019**, *9*. [CrossRef]
28. Eryaman, Y.; Akin, B.; Atalar, E. Reduction of implant RF heating through modification of transmit coil electric field. *Magn. Reson. Med.* **2011**, *65*, 1305–1313. [CrossRef] [PubMed]
29. Bachschmidt, T.J.; Köhler, M.; Nistler, J.; Geppert, C.; Jakob, P.M.; Nittka, M. Polarized multichannel transmit MRI to reduce shading near metal implants. *Magn. Reson. Med.* **2016**, *75*, 217–226. [CrossRef]
30. Vu, J.; Nguyen, B.T.; Bhusal, B.; Baraboo, J.; Rosenow, J.; Bagci, U.; Bright, M.G.; Golestanirad, L. Machine learning-based prediction of MRI-induced power absorption in the tissue in patients with simplified deep brain stimulation lead models. *IEEE Trans. Electromagn. Compat.* **2021**, *63*, 1757–1766. [CrossRef]
31. Stijnman, P.R.S.; Steensma, B.R.; van den Berg, C.A.T.; Raaijmakers, A.J.E. A perturbation approach for ultrafast calculation of RF field enhancements near medical implants in MRI. *Sci. Rep.* **2022**, *12*, 4224. [CrossRef]
32. Yun, Y.; Dong, Z.; Lee, N.; Liu, Y.; Xue, D.; Guo, X.; Kuhlmann, J.; Doepke, A.; Halsall, H.B.; Heineman, W. Revolutionizing biodegradable metals. *Mater. Today* **2009**, *12*, 22–32. [CrossRef]
33. Seitz, J.-M.; Lucas, A.; Kirschner, M. Magnesium-Based Compression Screws: A Novelty in the Clinical Use of Implants. *JOM* **2016**, *68*, 1177–1182. [CrossRef]
34. Espiritu, J.; Berangi, M.; Cwieka, H.; Iskhakova, K.; Kuehne, A.; Florian Wieland, D.C.; Zeller-Plumhoff, B.; Niendorf, T.; Willumeit-Römer, R.; Seitz, J.-M. Radiofrequency induced heating of biodegradable orthopaedic screw implants during magnetic resonance imaging. *Bioact. Mater.* **2023**, *25*, 86–94. [CrossRef]
35. IEC 60601-2-33 Medical Electrical Equipment-Part 2-33. In *Particular Requirements for the Basic Safety and Essential Performance of Magnetic Resonance Equipment for Medical Diagnosis Edition 3.2*; International Electrotechnical Commission (IEC): Geneva, Switzerland, 2015.
36. Raaijmakers, A.J.E.; Italiaander, M.; Voogt, I.J.; Luijten, P.R.; Hoogduin, J.M.; Klomp, D.W.J.; van den Berg, C.A.T. The fractionated dipole antenna: A new antenna for body imaging at 7 Tesla. *Magn. Reson. Med.* **2016**, *75*, 1366–1374. [CrossRef]
37. Ertürk, M.A.; Raaijmakers, A.J.E.; Adriany, G.; Uğurbil, K.; Metzger, G.J. A 16-channel combined loop-dipole transceiver array for 7 Tesla body MRI. *Magn. Reson. Med.* **2017**, *77*, 884–894. [CrossRef] [PubMed]
38. Lattanzi, R.; Wiggins, G.C.; Zhang, B.; Duan, Q.; Brown, R.; Sodickson, D.K. Approaching ultimate intrinsic signal-to-noise ratio with loop and dipole antennas. *Magn. Reson. Med.* **2018**, *79*, 1789–1803. [CrossRef] [PubMed]
39. Clemens, M.; Weiland, T. Discrete electromagnetism with the finite integration technique. *Prog. Electromagn. Res.* **2001**, *32*, 65–87. [CrossRef]
40. Kriegl, R.; Ginefri, J.C.; Poirier-Quinot, M.; Darrasse, L.; Goluch, S.; Kuehne, A.; Moser, E.; Laistler, E. Novel inductive decoupling technique for flexible transceiver arrays of monolithic transmission line resonators. *Magn. Reson. Med.* **2015**, *73*, 1669–1681. [CrossRef]
41. Deb, K. Multi-objective Optimisation Using Evolutionary Algorithms: An Introduction. In *Multi-OBJECTIVE Evolutionary Optimisation for Product Design and Manufacturing*; Wang, L., Ng, A.H.C., Deb, K., Eds.; Springer: London, UK, 2011; pp. 3–34.
42. Eichfelder, G.; Gebhardt, M. Local specific absorption rate control for parallel transmission by virtual observation points. *Magn. Reson. Med.* **2011**, *66*, 1468–1476. [CrossRef]

43. Alagappan, V.; Nistler, J.; Adalsteinsson, E.; Setsompop, K.; Fontius, U.; Zelinski, A.; Vester, M.; Wiggins, G.C.; Hebrank, F.; Renz, W.; et al. Degenerate mode band-pass birdcage coil for accelerated parallel excitation. *Magn. Reson. Med.* **2007**, *57*, 1148–1158. [CrossRef] [PubMed]
44. Zhu, Y.; Alon, L.; Deniz, C.M.; Brown, R.; Sodickson, D.K. System and SAR characterization in parallel RF transmission. *Magn. Reson. Med.* **2012**, *67*, 1367–1378. [CrossRef] [PubMed]
45. Duan, Q.; Duyn, J.H.; Gudino, N.; de Zwart, J.A.; van Gelderen, P.; Sodickson, D.K.; Brown, R. Characterization of a dielectric phantom for high-field magnetic resonance imaging applications. *Med. Phys.* **2014**, *41*, 102303. [CrossRef] [PubMed]
46. Ianniello, C.; de Zwart, J.A.; Duan, Q.; Deniz, C.M.; Alon, L.; Lee, J.S.; Lattanzi, R.; Brown, R. Synthesized tissue-equivalent dielectric phantoms using salt and polyvinylpyrrolidone solutions. *Magn. Reson. Med.* **2018**, *80*, 413–419. [CrossRef]
47. Gabriel, C. *Compilation of the Dielectric Properties of Body Tissues at RF and Microwave Frequencies*; King's College London: London, UK, 1996.
48. Santoro, D.; Winter, L.; Müller, A.; Vogt, J.; Renz, W.; Özerdem, C.; Grässl, A.; Tkachenko, V.; Schulz-Menger, J.; Niendorf, T. Detailing radio frequency heating induced by coronary stents: A 7.0 Tesla magnetic resonance study. *PLoS ONE* **2012**, *7*, e49963. [CrossRef]
49. Capek, M.; Eichler, J.; Hazdra, P. Evaluating radiation efficiency from characteristic currents. *IET Microw. Antennas Propag.* **2015**, *9*, 10–15. [CrossRef]
50. Kuroda, K.; Suzuki, Y.; Ishihara, Y.; Okamoto, K.; Suzuki, Y. Temperature mapping using water proton chemical shift obtained with 3D-MRSI: Feasibility in vivo. *Magn. Reson. Med.* **1996**, *35*, 20–29. [CrossRef]
51. Winter, L.; Oberacker, E.; Paul, K.; Ji, Y.; Oezerdem, C.; Ghadjar, P.; Thieme, A.; Budach, V.; Wust, P.; Niendorf, T. Magnetic resonance thermometry: Methodology, pitfalls and practical solutions. *Int. J. Hyperth.* **2016**, *32*, 63–75. [CrossRef]
52. Chung, S.; Kim, D.; Breton, E.; Axel, L. Rapid B1+ mapping using a preconditioning RF pulse with TurboFLASH readout. *Magn. Reson. Med.* **2010**, *64*, 439–446. [CrossRef]
53. Insko, E.K.; Bolinger, L. Mapping of the Radiofrequency Field. *J. Magn. Reson. Ser. A* **1993**, *103*, 82–85. [CrossRef]
54. Gosselin, M.-C.; Neufeld, E.; Moser, H.; Huber, E.; Farcito, S.; Gerber, L.; Jedensjö, M.; Hilber, I.; Gennaro, F.D.; Lloyd, B.; et al. Development of a new generation of high-resolution anatomical models for medical device evaluation: The Virtual Population 3.0. *Phys. Med. Biol.* **2014**, *59*, 5287. [CrossRef] [PubMed]
55. Silemek, B.; Seifert, F.; Petzold, J.; Hoffmann, W.; Pfeiffer, H.; Speck, O.; Rose, G.; Ittermann, B.; Winter, L. Rapid safety assessment and mitigation of radiofrequency induced implant heating using small root mean square sensors and the sensor matrix Qs. *Magn. Reson. Med.* **2021**, *87*, 509–527. [CrossRef]
56. Nyamayaro, K.; Keyvani, P.; D'Acierno, F.; Poisson, J.; Hudson, Z.M.; Michal, C.A.; Madden, J.D.W.; Hatzikiriakos, S.G.; Mehrkhodavandi, P. Toward Biodegradable Electronics: Ionic Diodes Based on a Cellulose Nanocrystal–Agarose Hydrogel. *ACS Appl. Mater. Interfaces* **2020**, *12*, 52182–52191. [CrossRef] [PubMed]
57. Sui, Y.; Kreider, L.P.; Bogie, K.M.; Zorman, C.A. Fabrication of a silver-based thermistor on flexible, temperature-sensitive substrates using a low-temperature inkjet printing technique. *IEEE Sens. Lett.* **2019**, *3*, 1–4. [CrossRef] [PubMed]
58. Poulo, L.; Alon, L.; Deniz, C.; Haefner, R.; Sodickson, D.; Stoeckel, B.; Zhu, Y.A. 32-channel parallel exciter/amplifier transmit system for 7T imaging. *Proc. Int. Soc. Magn. Reson. Med.* **2011**, *19*, 1867.
59. Han, H.; Oberacker, E.; Kuehne, A.; Wang, S.; Eigentler, T.W.; Grass, E.; Niendorf, T. Multi-Channel RF Supervision Module for Thermal Magnetic Resonance Based Cancer Therapy. *Cancers* **2021**, *13*, 1001. [CrossRef] [PubMed]
60. Fiedler, T.M.; Orzada, S.; Flöser, M.; Rietsch, S.H.G.; Quick, H.H.; Ladd, M.E.; Bitz, A.K. Performance analysis of integrated RF microstrip transmit antenna arrays with high channel count for body imaging at 7 T. *NMR Biomed.* **2021**, *34*, e4515. [CrossRef]
61. Vaidya, M.V.; Sodickson, D.K.; Lattanzi, R. Approaching ultimate intrinsic SNR in a uniform spherical sample with finite arrays of loop coils. *Concepts Magn. Reson. Part B Magn. Reson. Eng.* **2014**, *44*, 53–65. [CrossRef]

Curriculum Vitae

My curriculum vitae does not appear in the electronic version of my paper for reasons of data protection.

Publication list

---

1. (Accepted) **Mostafa Berangi**, Helmar Waiczies and Thoralf Niendorf, “RF power deposition magnification in MRI of fractured passive metallic implants”, ISMRM, 2024.
2. **Mostafa Berangi**, Andre Kuehne, Helmar Waiczies, Thoralf Niendorf MRI of Implantation Sites Using Parallel Transmission of an Optimized Radiofrequency Excitation Vector. Tomography. 2023; 9(2):603-620.
3. Jonathan Espiritu, **Mostafa Berangi**., Hanna Cwieka, Kamila Iskhakova, Andre Kuehne, D.C. Florian Wieland, Berit Zeller-Plumhoff, Thoralf Niendorf, Regine Willumeit-Römer, Jan-Marten Seitz, ‘’Radiofrequency induced heating of biodegradable orthopaedic screw implants during magnetic resonance imaging’’, Bioactive Materials, 2023. 25(NA): p. 86-94.
4. **Mostafa Berangi**, Helmar Waiczies and Thoralf Niendorf, ‘’Rapid transfer function-based transmission field shimming for safe and B_1^+ artefact free MRI of implantation sites’’, ISMRM, 2023, Abstract #2687.
5. Jonathan Espiritu, **Mostafa Berangi**, Christina Yiannakou, Eduarda Silva, Roberto Francischello, Andre Kuehne, Thoralf Niendorf, Sören Könneker, Regine Willumeit-Römer, Jan-Marten Seitz. “Evaluating metallic artefact of biodegradable magnesium-based implants in magnetic resonance imaging”. Bioactive Materials, 2022. 15: p. 382-391.
6. **Mostafa Berangi**, Andre Kuehne and Thoralf Niendorf “Excitation vector optimization for safe parallel transmission MRI of passively conducting implants in the presence of motion”, ISMRM, 2022, Abstract #2628.
7. **Mostafa Berangi**, Andre Kuehne and Thoralf Niendorf “Safe 7T MRI of tissues neighboring Mg-based biodegradable implants using parallel transmission”, ISMRM, 2021, Abstract #0360.
8. Andre Kuehne, …, **Mostafa Berangi**, … and Thoralf Niendorf” Parallel transmit local SAR vs. mesh resolution in EMF simulations of highly detailed anatomical models – a rigorous analysis”, ISMRM, 2020, Abstract #1121.
9. **Mostafa Berangi**, Vahid Ghodrati, Fereshteh Hasanzadeh, Puria Rafsanjani, Zahra Alizadeh Sani and Abbas Nasiraei Moghaddam, “Off-resonance error suppression in MOLLI T1 mapping using a specific CE-FAST”, ISMRM, 2019, Abstract #2215
10. **Mostafa Berangi**, Abbas Nasiraei Moghaddam, “Fast T2 estimation of heart using MOLLI dataset and a balanced-SSFP image”, SCMR, 2019
11. **Mostafa Berangi**, & Abbas Nasiraei Moghaddam "Analyzing the Influence of Imaging Parameters on Cardiac T1 Estimation Accuracy Using MOLLI," Electrical Engineering (ICEE), Iranian Conference on, Mashhad, Iran, 2018, pp. 1467-1470, doi: 10.1109/ICEE.2018.8472498.

Acknowledgments

I would like to express my sincere gratitude to my supervisor, Prof. Dr. Thoralf Niendorf, for his invaluable guidance, support, and encouragement throughout my journey. His deep knowledge, expertise, and commitment to my development as a scientist have been instrumental in shaping this thesis.

I am deeply thankful to Dr. Andre Kühne for his insightful discussions, constructive feedback, and collaborative spirit. His mentoring and guidance have played a crucial role in shaping my research and strengthening my analytical skills. I am grateful for his willingness to invest time and effort in mentoring me, and for the valuable lessons I have learned under his tutelage.

I would also like to extend my appreciation to Dr. Helmar Waiczies for his valuable inputs, guidance, and mentorship. His expertise in MRI physics, coil design and hardware has been invaluable in shaping the direction of my research. I am grateful for his willingness to share his knowledge and for his constant support and encouragement.

I would like to acknowledge the financial and educational support provided by the MgSafe Training Network (ITN). Their funding and support have been instrumental in enabling me to carry out this research and pursue my passion for advancing knowledge in this field. I am grateful for the opportunities, resources, and networking opportunities provided by MgSafe, which has significantly contributed to the success of this thesis project.

Moreover, I would like to express my gratitude to my wife, Mahsa Salimi Majd (Ph.D. candidate), my parents and brothers for their support, patience, and understanding. Their love, encouragement, and faith in me have been a constant source of motivation and strength throughout this journey. I am truly fortunate to have their support, which has played a vital role in my achievements.

Lastly, I would like to express my gratitude to all my colleagues, friends, and mentors who have supported me in various ways, whether through their insightful discussions, valuable suggestions, or simply their friendship. Your presence and encouragement have been invaluable, and I am grateful for the collaborative and inspiring environment in which we worked together.